OPTICAL STUDIES OF ION-BOMBARDED GALLIUM ARSENIDE

by

Guofu (Jeff) Feng

Dissertation submitted to the faculty of
the Virginia Polytechnic Institute and State University
in partial fulfillment of the requirements for the degree
of

DOCTOR OF PHILOSOPHY

in

Physics

APPROVED:

Richard Zallen, Chairman

A. L. Ritter

L. C. Burton

G. J. M. Indebetouw

C. D. Williams

May, 1989

Blacksburg, Virginia

OPTICAL STUDIES OF ION-BOMBARDED GALLIUM ARSENIDE

by

Guofu (Jeff) Feng

Committee Chairman: Richard Zallen
Department of Physics

(ABSTRACT)

The present work studies the disorder in ion-implanted and ion-etched GaAs semiconductors. The primary targets in this study consist of two types of systems: 45-keV Be^+-implanted GaAs and low-energy Ar^+-etched GaAs. Electronic and lattice structural disorder in these systems are investigated by means of optical reflectivity measurements and Raman-scattering techniques.

Visible-ultraviolet reflectivity measurements have identified finite-size effects on the interband electronic excitations in microcrystalline GaAs (μ-GaAs), which is known from previous work to exist in Be^+-implanted disordered GaAs. The optical properties of μ-GaAs differ appreciably from those of the bulk crystal, the difference increasing with L^{-1}, the inverse of the characteristic size of the microcrystals. The linewidths of the prominent interband features E_1, $E_1+\Delta_1$, and E_2 increase linearly and rapidly with inverse microcrystal size: $\Gamma_\mu = \Gamma_0 + AL^{-1}$, where Γ_0 (Γ_μ) is the linewidth in the bulk crystal (μ-GaAs), and A is a constant. A simple theory is proposed

which semi-quantitatively accounts for the observed size effects. Small microcrystal size implies a short time for an excited carrier to reach, and to be scattered by, the microcrystal boundary, thus limiting the excited-state lifetime and broadening the excited-state energy. An alternative uncertainty-principle argument is also given in terms of the confinement-induced *k*-space broadening of electron states.

The near-surface structural disorder in Ar^+-etched GaAs has been investigated using a combination of Raman scattering and optical reflectivity measurements. The longitudinal optical (LO) Raman mode in the ion-damaged medium preserves its crystalline lineshape, indicating that the crystalline long-range order is retained in the disordered structure. The structural damage is depth-profiled with LO Raman intensity measurements together with wet chemical etching. A graded damage model proposed in the work well explains the observed LO intensity in the ion-damaged, chemical-etched GaAs. The reflectivity measurements qualitatively support the Raman scattering findings. In addition, the reflectivity spectrum exhibits a red-shift of the peaks associated with the interband electronic transitions. Such a peak shift is likely to arise from the electron-defect interaction in the disordered surface medium.

ACKNOWLEDGMENTS

I am especially grateful to my advisor, Prof. Richard Zallen, for his guidance and support throughout the course of this work. His inspiration will continue serving well in my future professional career. I would also like to thank Prof. Sam Bowen, Prof. Larry Burton, and Prof. John Dillard for their valuable conversations.

I would like to thank Prof. Diane Hoffman for her invaluable advice on spectroscopic instrumentation and for sharing her expertise on optical experimentation.

I am indebted to Dr. Mark Holtz for his work on which part of this work is built. I also enjoyed the fun and fruitful period of time that I shared the office and the laboratory with him. Special thanks go to Dr. June Epp, who spent much time preparing some essential samples used in this work. I wish to thank Texas Instruments, ITT Corperation, and the Virginia Center for Innovative Technology for supporting this work. I would also like to thank Dr. David Aspnes of Bellcpre for providing optical data on amorphous GaAs.

I am grateful to many staff menbers in the Physics Department, especially to and for their personal and professional support.

I have enjoyed and benefited from many interesting

and suggestive conversations with my fellow graduate students and colleagues , , ,
, , ,
, , and many others.

Finally, I wish to express special appreciations to my wife, , whose encouragement, support, and love made this work possible.

This work is dedicated to my parents.

Attention Patron:

Page v repeated in numbering

TABLE OF CONTENTS

Attention Patron:

Page vii omitted from numbering

CHAPTER 1

INTRODUCTION

1.1 Overview

1.1.1 Semiconductor GaAs

Gallium Arsenide (GaAs) is a III-V compound semiconductor with the cubic zincblende crystal structure. Its primitive cell consists of two atoms, one Ga atom and one As atom. The structure has face-center cubic (fcc) translational symmetry. The bond length between the Ga site and the As site is 2.45 Å, while the length of the side of the unit cube is 5.65 Å.[Blakemore 1982] Its first Brillouin zone has the same shape as for the fcc lattice, a truncated octahedron. Figure 1.1 shows both the unit cube and the first Brillouin zone of the GaAs crystal.

Figure 1.2 shows the theoretical band structure for GaAs crystal calculated by Chelikowsky and Cohen [1976] using the nonlocal pseudopotential approach. The highest valence band in the figure is the curve with the label $L_{4,5}$ near -1 eV, and the lowest conduction band is the one with the label L_6 near 2 eV. The spin-orbit splitting of the highest valence band is relatively large in the L-Γ-X

regions, and is about 0.2 eV along the Λ directions near the L points. As can be seen in the band structure, GaAs is a direct-gap semiconductor. The direct valence-to-conduction transitions occur near the zone center, $\Gamma_8^v \rightarrow \Gamma_6^c$, with the bandgap being 1.424 eV at room temperature.[Sell et al. 1974]

The direct-bandgap characteristic of GaAs has two essential consequences in its application potential relative to indirect-gap semiconductors such as silicon. The first consequence is that it can be used as an efficient light-emitting material. Direct bandgap semiconductors are ideal candidates for electroluminescent devices (such as diode lasers) because the radiative recombination is a first order transition process and the quantum efficiency is much higher than that for an indirect-gap semiconductor, where a phonon has to be involved.[Sze 1981] The second consequence lies in the fact that the curvature of the conduction band near the zone center Γ_6^c is very large compared with those near the zone edge points. The corresponding effective mass m^*, which is proportional to $|\nabla^2 E(k)|^{-1}$, is hence very small. Consequently, the electron mobility in GaAs is high. As a matter of fact, the electron mobility in GaAs is a factor of 6 greater than that in silicon, which is an indirect-gap semiconductor.[Shur 1988] In Si the conduction

electrons are largely located in the flat valleys near the X_6^c symmetry points, the conduction band minima of its band structure. High mobility is an advantage in many semiconductor devices such as field effect transistors (FETs).

1.1.2 Ion Implantation and Ion Etching

Ion implantation and ion etching techniques have been extensively used in semiconductor device fabrication. The disorder introduced by ion bombardment during ion processing is of great technical importance in device manufacturing. It also provides a special means to study disordered solids and the process of amorphization.

Ion implantation is the introduction of energetic charged particles into a solid substrate. Ion implantation as a technique for controllably and reproducibly introducing shallow conductive layers into bulk grown semi-insulating substrates is now a standard procedure in doping semiconductors. In addition, ion implantation can be used for selectively isolating active regions during integrated circuits processing.[Duncan and Westphal 1985] The typical ion energies used in implantation range from 10 to 400 keV, while the ion dose (fluence) is usually kept below 10^{16} ion/cm^2.

Ion etching, on the other hand, is a low-energy ion

bombardment process in which directional or patterned substrate etching occurs. Controllable etch profiles give ion etching an advantage over wet chemical etching in many device fabrication processes. Reactive ion etching, ion beam bombardment in a plasma environment, is an essential procedure in the fabrication of GaAs Schottky-barrier metal-semiconductor field-effect transistors (MESFETs). [see for example, Shur 1988] The ion energies used in ion etching are typically of the order of 1 keV, and the ion fluence is often over 10^{16} cm^{-2}. Lower-energy inert gas ions are also used in semiconductor surface cleaning processes.[Epp and Dillard 1989]

In both ion implantation and ion etching, substrate structural damage introduced by the interaction of the energetic impinging particles and the substrate is inevitable. A damage layer extending from the substrate surface to a depth of a few thousand angstroms is often created during ion implantation. A follow-up annealing step is needed to structurally heal and electrically activate the implantation layer.[Duncan and Westphal 1985] In the case of ion etching, physical sputtering creates a shallow near-surface damage layer of a few hundred angstroms in depth. Possible processes such as displacement of lattice atoms by the energetic incident particles, etching induced surface contamination,

depletion layer due to preferential etching, etc., may severely degrade the quality of the device. Better understanding of damage mechanisms is essential in order to better control the device fabrication procedures and to improve the device quality.

On the other hand, radiation damage during ion bombardment allows one to create controllable disorder in crystalline solids, and thus offers a new mechanism of investigating the disorder in the crystal. By gradually tuning the bombardment parameters, it is possible to study the amorphization process in a particular way [Sadana 1985] and compare it to "conventional" amorphization processes.[Zallen 1983]

1.1.3 Optical Probes of Semiconductors

The optical response of a semiconductor to probing light at room temperature can be classified into two catagories: the lattice vibrational response and the electronic response.

The lattice vibrational excitations, or phonons, have characteristic excitation energies of the order of 10 meV or 10^2 cm^{-1}. The corresponding spectral features thus appear in the far-infrared regime. Phonons are directly related to the lattice structure, and therefore provide rich information about the crystal structure. The phonon

dispersion for GaAs crystal is shown in Fig. 1.3.[Dorner and Strauch 1987] The three optical modes of the lattice vibration belong to two optic branches at the Brillouin zone center Γ, $\Gamma = (0,0,0)$. At the Γ point the longitudinal optic (LO) branch is non-degenerate, while the transverse optic (TO) branch is doubly degenerate. As will be discussed in Sec. 1.3, the zone-center phonons are of particular importance in Raman scattering processes.

Two optical techniques are frequently employed in the study of lattice vibrations, namely infrared (IR) absorption and Raman scattering. Raman scattering is particularly useful in the study of ion processed semiconductors, because the disordered damage layer in the medium is shallow compared with the total substrate thickness. A typical ratio of the disorder layer depth to the substrate thickness is about 5000 Å to 500 μm, or 1/1000. This makes it very difficult to extract information about the disordered layer from measurements of the IR transmittance. Raman scattering, in contrast, uses visible or near-visible light as probing excitation, which has an optical penetration depth of the order of 500 Å in gallium arsenide [see for example, Aspnes and Studna 1983]. This is an ideal penetration depth for probing the damage layer in ion-processed GaAs.

In the visible and ultraviolet regime, the optical

response of a semiconductor originates mainly from the interaction of the electrons in the medium with the probing light. Such interactions can be described by the dielectric properties of the semiconductor. The dielectric response function reflects the direct interband electronic transitions induced by the incident light. It is a collective effect of many-body interactions. The dielectric properties not only depend on the atomic local potential, but also rely heavily on the long range order of the medium and the electronic band structure. It is therefore no surprise that the UV-visible dielectric properties are often more sensitive than the lattice vibrations to the crystalline perfection. The measurement of reflectivity in the visible and near-ultraviolet is a relatively simple experimental technique, and is well suited for the characterization of ion-processed semiconductors. The dielectric properties can be derived from the reflectivity spectrum, as will be discussed in the next section.

Raman scattering can also be used to study properties related to the electronic band structure. This is often done in the resonance Raman scattering processes in which the photon energy of the incident light or the scattered light (or both) is close to the energy of electronic transitions near critical points (see the next

section).[Cardona 1982]

The purpose of this work is to understand better the nature of the structural disorder which is introduced into semiconductors by ion implantation and ion etching. Scientific interest in such disordered structures resides in the fact that they provide various structures "intermediate" between the crystalline state and the amorphous state. These intermediate structural states have opened new channels to certain phenomena not previously accessible. The experimental means employed in this study are optical reflectivity measurements and Raman scattering measurements. Optical experiments are non-destructive and fairly easy to access. Yet they provide rich information of interest.

The fundamentals of optical properties and Raman scattering processes in solids are discussed in the next two sections of this chapter. The next chapter describes the experimental aspects of the reflectivity and Raman scattering measurements. Chapter 3 presents a reflectivity study of beryllium-implanted GaAs. The observation of size effects on optical and structural properties in the implanted medium is discussed in detail. Chapter 4 studies the nature as well as the depth distribution of the structural disorder of argon-ion etched GaAs. A brief

summary of this work is given in the last chapter of this dissertation.

1.2 Optical Properties of Semiconductors

1.2.1 Optical Functions

The response of a solid to the electromagnetic field of light can be described, to the first order, by its dielectric function which is generally complex and frequency dependent. The fact that the wavevector of vis-near-UV light is very much smaller than the Brillouin-zone size allows us to neglect the wavevector-dependence of the optical response. We hence write

$$\varepsilon(\omega) = \varepsilon_1(\omega) + i\varepsilon_2(\omega) \ , \qquad (1.1)$$

where ω is the angular frequency of the light, and ε_1 and ε_2 are the real and imaginary parts of the dielectric function ε, respectively.

The imaginary part of the dielectric function, $\varepsilon_2(\omega)$, represents the absorptive nature of the solid. It becomes appreciable in a semiconductor when the energy of the incident photon, $\hbar\omega$, exceeds the energy gap of the semiconductor. ε_2 is intimately related to the band structure of the crystal. In the one-electron approximation, it can be written as [Cohen 1958, Petroff 1980]:

$$\varepsilon_2(\omega) = \frac{2e^2\hbar^2}{3m^2}\,\frac{2}{(2\pi)^3}\sum_{n,m}\int \frac{|\langle k,n|P|k,m\rangle|^2\ dS}{\omega_{nm}^2\,|\nabla_k\,\omega_{nm}|} \qquad (1.2)$$

where $\omega_{nm} = (E_n - E_m)/\hbar$ represents the interband energy with n and m as band indices, and P is the momentum operator. The integral runs over a surface in k-space on which $\omega_{nm} = \omega$. The integrand has singularities at points in k-space where the gradient in the denominator vanishes. These points, where $\nabla_k\omega_{nm} = 0$, are called critical points, first stressed by Van Hove [1953]. It is these singularities associated with the critical points that bring about the distinctive features in the spectrum of the dielectric function and other optical spectra.

The real part of the dielectric function, $\varepsilon_1(\omega)$, is related to the imaginary part through causality relations, often known as Kramers-Krönig relations [see for example, Wooten 1972, Shiles et al. 1980]:

$$\varepsilon_1(\omega) - \varepsilon_\infty = \frac{2}{\pi}\,\mathcal{P}\int_0^\infty \frac{\omega'\varepsilon_2(\omega')}{\omega'^2 - \omega^2}\,d\omega' \ ; \qquad (1.3a)$$

$$\varepsilon_2(\omega) = \frac{2\omega}{\pi}\,\mathcal{P}\int_0^\infty \frac{\varepsilon_1(\omega')}{\omega'^2 - \omega^2}\,d\omega' \ . \qquad (1.3b)$$

Other optical quantities are often used, depending on the system or the properties being investigated. They are all related to each other, and to the dielectric function. Some of the commonly used quantities are summarized here.

The complex index of refraction, $N(\omega) = n(\omega) + ik(\omega)$ is related to ε by

$$N^2 = \varepsilon \ , \tag{1.4a}$$

or $$\varepsilon_1 = n^2 - k^2 \tag{1.4b}$$

and $$\varepsilon_2 = 2nk \ . \tag{1.4c}$$

Here n is the refractive index and k the extinction coefficient.

The reflectivity R is by far the most commonly measured optical quantity in the region above the energy bandgap of a semiconductor, where transmission measurements are difficult because the absorption is so large. In the case of normal incidence,

$$R = \left|\frac{N-1}{N+1}\right|^2 = \left|\frac{n-1-ik}{n+1-ik}\right|^2 . \tag{1.5}$$

In the regime below or near the energy gap, or for studies of core-to-conductionband transitions, transmission measurements are often used. The transmission of a plane-parallel slab-shaped sample can be written as,

$$T = \frac{I}{I_0} = \frac{(1-R)^2 \ e^{-\alpha d}}{1 - R^2 e^{-2\alpha d}} \ , \tag{1.6}$$

where R is the surface reflectivity, d is the sample thickness, and α is the absorption coefficient. α is related to other optical quantities by

$$\alpha = 4\pi k/\lambda = \varepsilon_2 \omega/nc \ . \qquad (1.7)$$

where λ is the wavelength and c the speed of light.

1.2.2 Classical Oscillator Representation

Theoretically, the dielectric function, and hence all the other optical responses, of a crystalline solid can be calculated approximately by using Eq. 1.2, once the band structure ($E_n(k)$ and $|k,n\rangle$) is known. In practice, however, even for the simplest semiconductors like Si and Ge, theoretical calculations, such as those obtained by the pseudopotential approach which is viewed as the best technique to date [Cohen and Chelikowsky 1982, 1988], yield quantitatively poor reproduction of the experimental optical spectrum.[Petroff 1980] The difficulty is essentially due to the complexity of the crystal potential in real solids, and to the large amount of computation to be handled in determining the band structure and the optical properties. Equation 1.2 has not yielded a simple analytic expression of the dielectric function with general validity to crystalline semiconductors. For disordered semiconductors, calculations are even more difficult. Phenomenological expressions thus play an important role in analytically depicting the observed optical response functions of real materials.

Classical analysis of the electrodynamic interaction

in a solid reveals that the dielectric response of a substance can be represented in terms of damped oscillators.[see for example, Burns 1985] The oscillator expression of the dielectric function can be written as [Spitzer 1960, Verleur 1968]:

$$\varepsilon(\omega) = \varepsilon_{\infty} + \sum_{i=1}^{n} \frac{F_i^2}{(\omega_i^2 - \omega^2) - i\omega\Gamma_i} . \qquad (1.8)$$

Here ε_{∞} is the high frequency asymptote of the dielectric function (representing the contributions from strongly bound high-frequency oscillators such as core levels). The parameters F_i, ω_i, and Γ_i are the strength, position, and damping parameters of the i^{th} oscillator. Shown in Fig. 1.4 are the lineshapes of the real and imaginary parts of the dielectric response represented by two classical oscillators with the following parameters: F_1 = 3 eV, ω_1 = 2 eV, Γ_1 = 0.3 eV, F_2 = 5 eV, ω_1 = 4 eV, Γ_1 = 0.5 eV. The reflectivity derived from this dielectric function is plotted in Fig. 1.5.

In the lattice-vibrational region of the dielectric response, the oscillator parameters have clear physical significance. For instance, the oscillator position ω_1 is just the transverse-optic phonon frequency of a lattice vibrational mode represented by the oscillator.[Verleur 1968] In the region of the interband electronic transitions, such correspondence is not as apparent, and

Eq. 1.8 is often viewed as a mathematical tool which analytically reproduces the dielectric response of a real soild.[Verleur 1968, Erman et al. 1984] It will be demonstrated later in Chapter 3, however, that for a carefully selected set of the classical oscillators, some of the oscillator parameters still possess well defined physical significance and may be interpreted as Van Hove singularities resulting from electronic transitions near critical points in *k*-space.

1.2.3 Effective Medium Approximation

We have so far discussed the optical properties of a homogeneous medium. In ion-processed semiconductors the structural homogeneity is degraded by the incident energetic ions, often resulting in a heterogeneous layer near the substrate surface. The dielectric response of a heterogeneous medium can be described in terms of the dielectric properties of its components and the nature of the inhomogeneity.[Aspnes 1982, 1984] The effective dielectric response of the heterogeneous medium can be described by the Bruggeman effective medium approximation (EMA), a self-consistant effective medium theory. [Bruggeman 1935, Aspnes 1982] According to the effective medium approximation, the effective dielectric function, ϵ, of a heterogeneous medium which is composed of

particles of different components, is given by:

$$\sum_{i=1}^{N} f_i \frac{\varepsilon_i - \varepsilon}{\varepsilon_i + 2\varepsilon} = 0 \ . \qquad (1.9)$$

Here N is the number of components, and ε_i and f_i are the dielectric function and volume fraction of the i^{th} component.

The dielectric functions of the components in Eq. 1.9 are often taken as their bulk counterparts. It will be shown later that care must be taken in applyiny this seemingly apparent assumption, because the dielectric response of small-size particles can be substantially different than that of the corresponding bulk material.

1.3 Raman Scattering Processes

Raman scattering is an inelastic light scattering process in which an excitation (or excitations) in the scattering medium is created or annihilated. In the case of first-order Raman scattering by a lattice vibrational excitation (phonon), the scattering process can be described by third order time-dependent perturbation theory.[Pinczuk and Burstein 1975] Two intermediate states, |a> and |b>, are involved in the process. State |a> is an electron-hole (e-h, correlated or uncorrelated) pair state in which the electron is excited from the

valence band to the conduction band via the absorption of an incident photon, leaving the hole in the valence band. State |b> is another e-h pair state resulting from the interaction of the electron or hole with the lattice vibration in which a phonon is created (Stokes process) or annihilated (anti-Stokes process). The electron-hole pair |b> then itself recombines, emitting a scattered photon.

First-order Raman scattering processes can also be represented schematically as shown in Fig. 1.6. In Fig. 1.6a a phonon is created via the interaction of an electron with the lattice vibration, while in Fig. 1.6b it is done by the interaction of a hole with the lattice vibration. Energy is conserved only in the total process, whereas wavevector is conserved at each vertex of the Feynman diagram in Fig. 1.6.[Pinczuk and Burstein 1975] This results in the basic selection rules of the Raman scattering process:

$$\omega_2 = \omega_1 \mp \omega \ , \tag{1.10}$$

$$k_2 = k_1 \mp q + K \ . \tag{1.11}$$

Here $\hbar\omega_1$ and $\hbar\omega_2$ (k_1 and k_2) are the energies (wavevectors) of the incident and scattered photons, and $\hbar\omega$ (q) is the phonon energy (wavevector). K is a reciprocal lattice vector, and is zero unless higher orders are involved. The - (+) sign denotes the Stokes

(anti-Stokes) process. In typical Raman scattering experiments in which both the incident and scattered light are in the visible or near-visible,

$$k_1 = |k_1|,\ k_2 = |k_2| \ll 2\pi/a , \tag{1.12}$$

where a is the lattice constant. This leads to a restriction on the phonon momentum,

$$q = |q| \sim 0 \tag{1.13}$$

for the first order scattering. Hence only phonons near the Brillouin zone center may be involved in first-order Raman scattering processes. This restriction, however, is somewhat relaxed in a crystal opaque to the visible light [Buchner and Burstein 1974], and is substantially affected in an imperfect crystal [see for example, Berg and Yu 1987 and references therein].

The three transitions, with creation and annihilation of the three quanta involved in the Raman process, may occur in any time order, leading to six terms in the Raman tensor.[Loudon 1964] A typical term, which has particular importance in resonance Raman scattering processes, takes the following form [Martin and Falicov 1975, Hayes and Loudon 1978]:

$$\sum_{a,b} \frac{\langle f|H_{ER}|b\rangle\langle b|H_{EL}|a\rangle\langle a|H_{ER}|i\rangle}{[(E_b+i\hbar\gamma_b)-\hbar\omega_2][(E_a+i\hbar\gamma_a)-\hbar\omega_1]} , \tag{1.14}$$

where E_a (E_b) and $1/\gamma_a$ ($1/\gamma_b$) are the electronic excitation energy and lifetime of the intermediate state $|a\rangle$ ($|b\rangle$), and H_{ER} and H_{EL} are the interaction Hamiltonians for the electron and photon and the electron and lattice vibration, respectively.

The Raman tensor $\overleftrightarrow{R}$, which is composed of terms of the type of (1.14), plays the essential role in the Raman scattering cross section, which can be written as:

$$\frac{d\sigma^2}{d\Omega d\omega_2} \sim (n(\omega_1)+1)\,|e_2 \cdot \overleftrightarrow{R} \cdot e_1|^2 \ , \qquad (1.15)$$

where $n(\omega_1)$ is the phonon occupation number (for anti-Stokes scattering the factor $n(\omega_1)+1$ should be replaced by $n(\omega_1)$), e_1 and e_2 are the unit vectors representing the polarization of the incident and the scattered light.

The selection rules given in Eqs. 1.10 and 1.11 greatly simplify the analysis of Raman scattering processes in crystalline solids. The crystal momentum conservation leads to the fact that only the zone center (Γ) phonons participate in the first-order Raman processes. For the zincblende structure of GaAs, the crystal factor group for Γ = (0,0,0) is isomorphic to the tetrahedral point group T_d, which has been extensively studied.[Birman 1974] The spatial symmetries of crystals

have two consequences for the scattering processes in addition to those derived from the momentum conservation and the energy conservation.

The first consequence is the existence of symmetry selection rules which allow only certain phonon modes to be Raman active. The first-order Raman process involving electron-phonon interaction can be depicted by the three consecutive transitions discussed above. In the electronic transition processes the vibrational states remain unchanged; state $|a\rangle$ has the same vibrational state as state $|i\rangle$, and so have states $|b\rangle$ and $|f\rangle$. The transformation properties of the matrix elements $\langle f|H_{E\,R}|b\rangle$ and $\langle a|H_{E\,R}|i\rangle$ are hence governed by the symmetry properties of the operator $H_{E\,R}$, which is equivalent to a dipole moment.[Birman 1974] The dipole moment is a polar vector that transforms as the irreducible representation $\Gamma_{1\,5}$ of the group T_d. The matrix element $\langle b|H_{E\,L}|a\rangle$ represents a vibrational excitation. The Raman tensor governed by the three consecutive interactions is invariant under the operations of the crystal symmetry. This requires that the vibrational excitation $\langle b|H_{E\,L}|a\rangle$ transforms as a representation contained in the direct product of two polar vector representations. Thus, the symmetry of the excitation, denoted as Γ_X, must follow

$$\Gamma_X \subset \Gamma_{1\,5} \times \Gamma_{1\,5} = \Gamma_1 + \Gamma_{1\,2} + \Gamma_{1\,5} + \Gamma_{2\,5} \ . \qquad (1.16)$$

The last equation can be derived by use of standard group-theory techniques.[Elliott and Dawber 1979] The possible vibrational modes in a crystal can be obtained by the analysis of the factor group of the crystal space symmetry.[Lax 1974, Birman 1974] Both the acoustic branch and the optic branch in the zincblende crystal belong to the Γ_{15} irreducible representation.[Parmenter 1955, Birman 1974]. According to Eq. 1.16 they are both Raman active. In a perfect crystal, the first-order Raman scattering process however involves only the optic phonons, because the acoustic phonon at the Γ point has zero energy (see Fig. 1.3). In an imperfect crystal [Brodsky 1975], or for higher order processes [Trommer and Cardona 1977], the acoustic phonons may be active.

The second consequence of the crystal symmetry is that for a symmetry-allowed phonon mode certain components of the second-rank Raman tensor must vanish.[Hayes and Loudon 1978] A detailed classical description of the symmetry of second-rank tensors in a crystal can be found in the work by Nye [1957, 1987]. Lax [1974] has discussed this topic in a quantum approach. The results of the Raman tensors for the 32 crystallographic point groups have been tabulated by a number of authors.[Loudon 1964, Cardona 1975, Hayes and Loudon 1978] It is the nonvanishing matrix elements of the allowed phonons, coupled with the proper

polarization of the incident (e_1) and the scattered (e_2) light (see Eq. 1.15), that contribute to the observed Raman spectrum.

The matrix representation of the Raman tensor for the Γ_{15} phonon in GaAs (zincblende structure) is given in Table 1.1a. The selection rules for backscattering from the (100) crystal surface are listed in Table 1.1b. It is clear that in this scattering geometry only the LO phonons participate in the scattering processes.

Table 1.1 Symmetry of Raman scattering in zincblende crystals

a. Raman tensor for the Γ_{15} phonons

Longitudinal phonon

$$\begin{bmatrix} & & \\ & & d \\ & d & \end{bmatrix}$$

Transverse phonons

$$\begin{bmatrix} & & d \\ & & \\ d & & \end{bmatrix} \qquad \begin{bmatrix} & & d \\ d & & \\ & & \end{bmatrix}$$

b. Deformation potential Raman selection rules for backscattering from the (100) surface

Polarization Configuration	Raman Modes		
	LO(z)	TO(x)	TO(y)
$z(x,x)\bar{z}$	0	0	0
$z(x,y)\bar{z}$	d^2	0	0
$z(y,y)\bar{z}$	0	0	0
	LO(z')	TO(x')	TO(y')
$z(x',x')\bar{z}$	d^2	0	0
$z(x',y')\bar{z}$	0	0	0
$z(y',y')\bar{z}$	d^2	0	0

Note that

$x = \langle 100 \rangle$, $y = \langle 010 \rangle$, and $z = \langle 001 \rangle$

$x' = \langle 110 \rangle/\sqrt{2}$, $y' = \langle 1\bar{1}0 \rangle/\sqrt{2}$, and $z' = \langle 001 \rangle$.

Figure Captions

Fig. 1.1 Conventional unit cube for the zincblende lattice (a), and the first Brillouin zone for GaAs and other fcc lattices (b).

Fig. 1.2 Band structure of GaAs calculated by Chelikowsky and Cohen using the non-local pseudopotential approach. (after Chelikowsky and Cohen [1976]). The three virtical lines labelled a, b,and c represent critical-point valenceband-to-conductionband direct interband transitions (denoted as E_1, $E_1+\Delta_1$, and E_2, respectively) discussed in Chapter 3 and 4.

Fig. 1.3 Phonon dispersion for GaAs crystal. (after B. Dorner and D. Strauch [1987]).

Fig. 1.4 Dielectric function described by two Lorentz harmonic oscillators of the parameters: $\varepsilon_\infty = 1$, $F_1 = 3$ eV, $\omega_1 = 2$ eV, $\Gamma_1 = 0.3$ eV; $F_2 = 5$ eV, $\omega_2 = 4$ eV, and $\Gamma_2 = 0.5$ eV.

Fig. 1.5 The reflectivity spectrum calculated from the dielectric function of Fig. 1.4.

Fig. 1.6 Illustrations of the first-order Raman scattering processes. A phonon can be created through the interaction of an excited electron and the lattice vibration (a), or through the interaction of the hole and the lattice vibration (b).

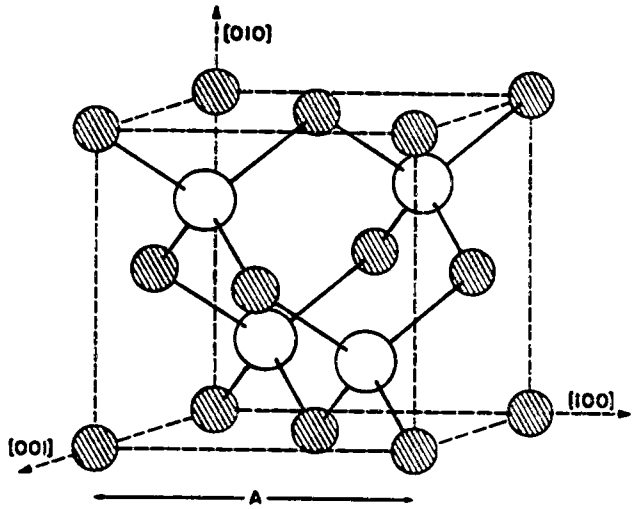

(a) Unit cube

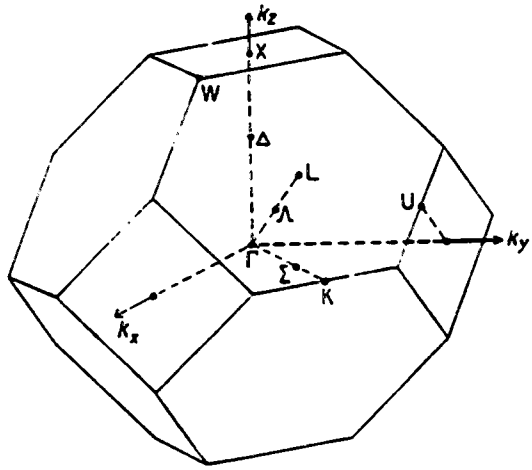

(b) First Brillouin zone

Fig. 1.1 The unit cube and first Brillouin zone of GaAs

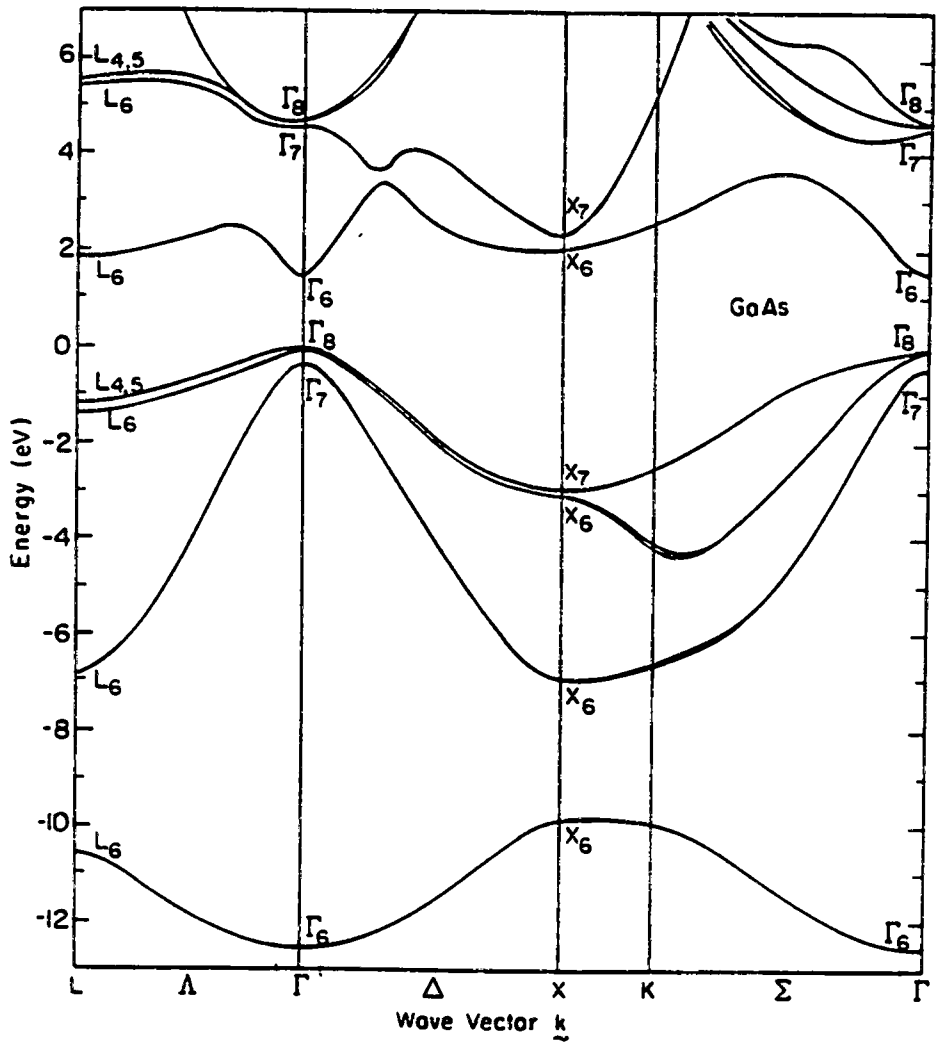

Fig. 1.2 Band structure of GaAs crystal

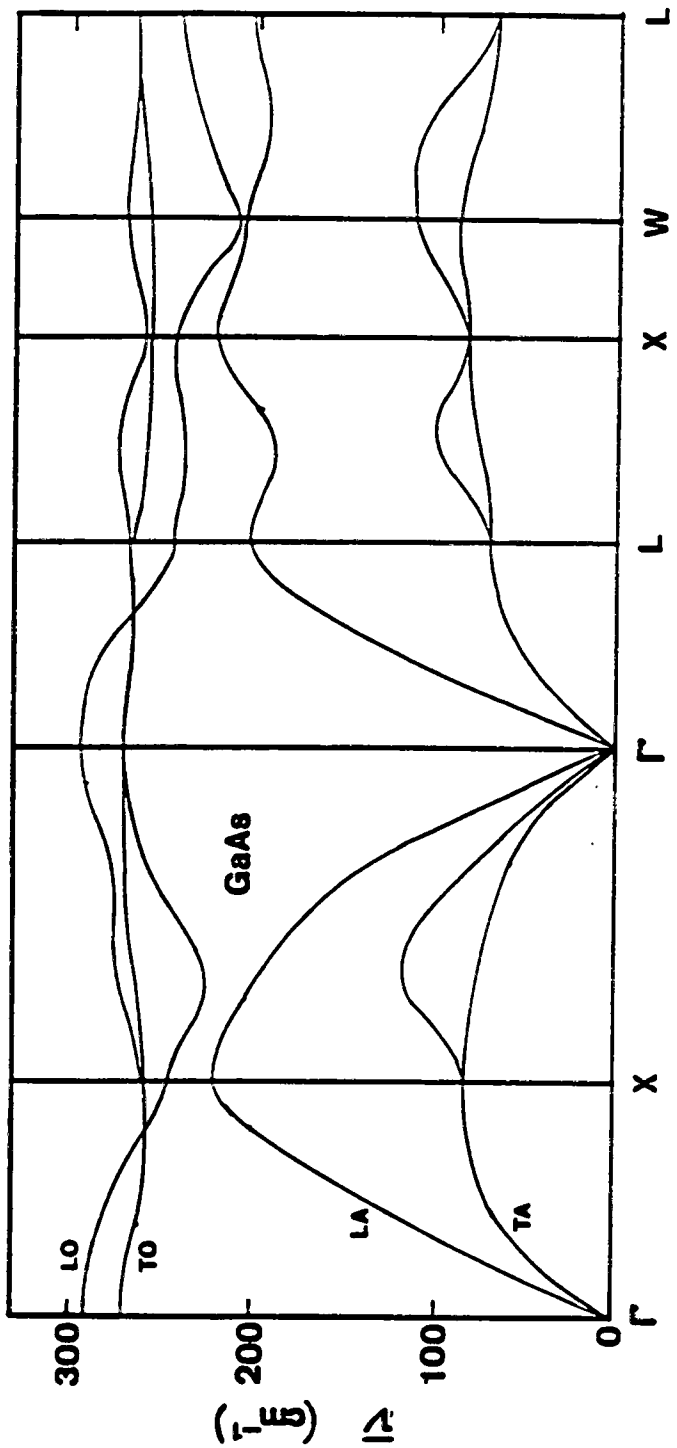

Fig. 1.3 Phonon dispersion for GaAs crystal

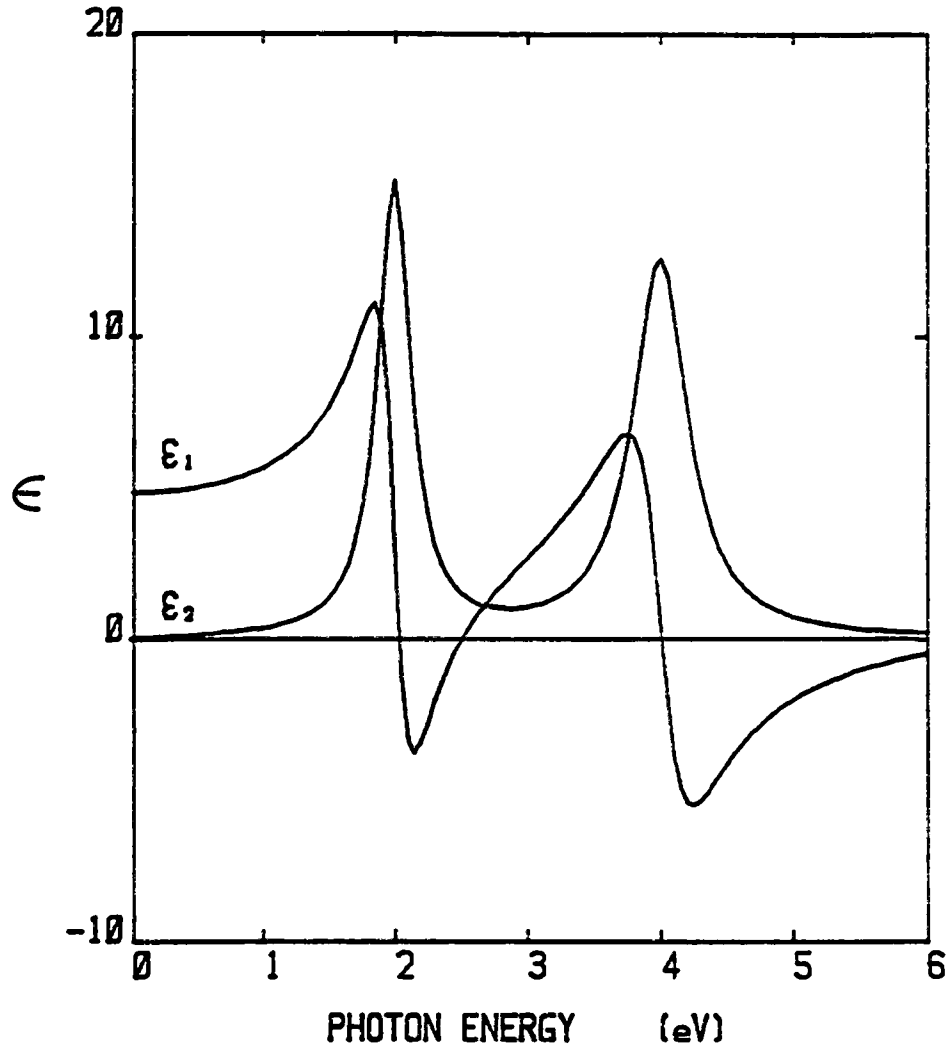

Fig. 1.4 Dielectric function described by two oscillators

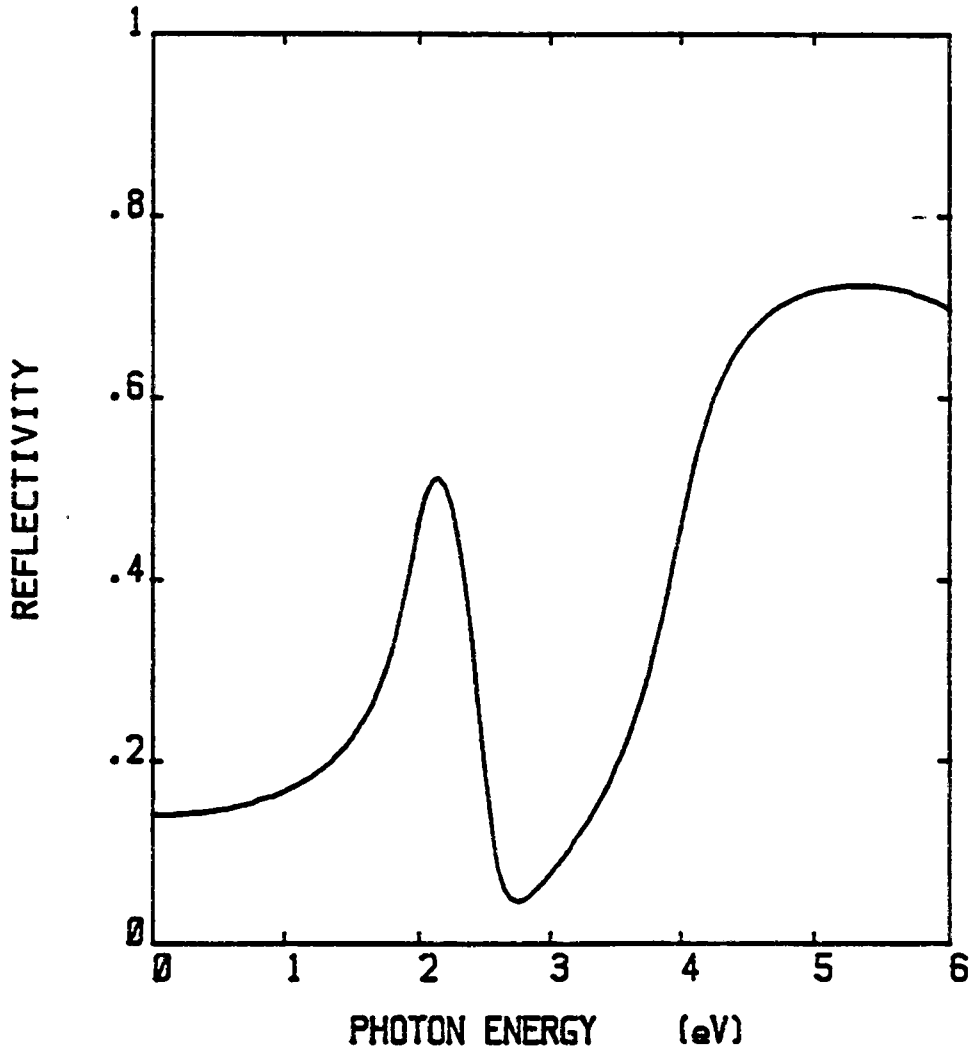

Fig. 1.5 Reflectivity from the ε of Fig. 1.4

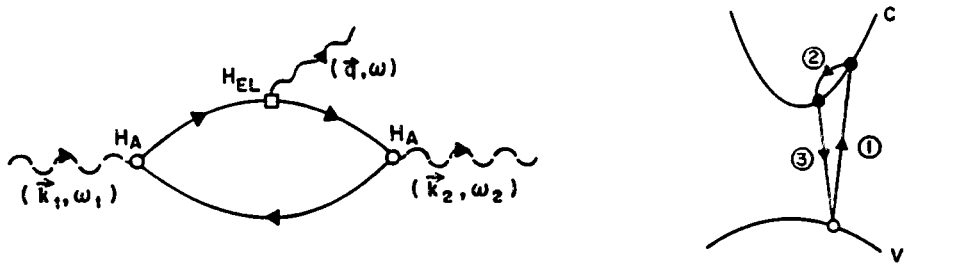

(a) electron-phonon interaction

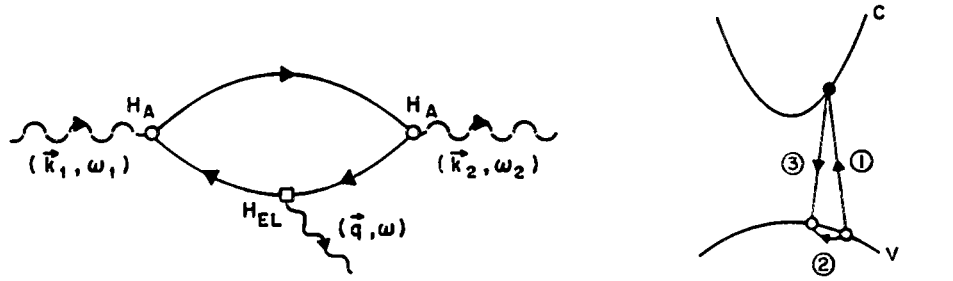

(b) hole-phonon interaction

Fig. 1.6 First-order Raman scattering processes

CHAPTER 2

INSTRUMENTATION

Most of the optical experiments performed in this study were carried out using a prism-grating spectrometer operating in the infrared through the near ultraviolet (IR-near-UV) optical region and a Raman spectrometer with an Argon-ion laser or a Krypton-ion laser. Although other instruments, such as a Fourier-transform infrared spectrometer (FTIR) and a closed-cycle compressed-helium cryostat, were used in some of the experiments, this chapter will mainly describe the two principal instruments used: the IR-near-UV spectrometer and the Raman spectrometer.

2.1 IR-near-UV Spectrometer

2.1.1 Spectrometer Optics

The IR-near-UV spectrometer is a two-stage monochromatic spectrometer. Its first stage is either a prism monochromator or an optical filter, depending on the measurement region (see Table 2.1). The purpose of the first stage is to transmit light with a narrow wavelength bandwidth so that the higher diffraction orders in the

second stage will be eliminated. The prism monochromator (model 160, Perkin-Elmer) employs a glass prism with a 15° apex angle. The prism is relatively thin (hence less absorptive), so that it can operate up to 6 eV in photon energy, or about 2000 Å in wavelength, in the near-ultraviolet region. Resolution is not a problem because its spectral bandpass is much less than that of the filters that were used in the original design, and which now are replaced with the prism. For photon energy below 1 eV (above 1.2 μm in wavelength) optical filters were used.

The spectral dispersion is mainly carried out by the second stage of the spectrometer, which is a grating monochromator (model 16U, Perkin-Elmer). With four gratings working in different spectral regimes, the grating monochromater provides a wide measurement range from 0.077 eV to 6 eV in photon energy, or from 2000 Å to 16 μm in wavelength (see Table 2.1). Table 2.1 also gives the correspondence of the light sources and the detectors to the measurement ranges.

Three different types of light sources are available: a deuterium lamp working in the near-ultraviolet region, a tungsten lamp used in the visible-near-infrared region, and a globar source for the rest of the infrared region (see Table 2.1). The three sources have considerable

overlaps in their measurement regions, and thus spectral "patching" can be done. The beam is chopped with a low frequency light chopper (model OC 4000, PTI). The measured signal is detected with either a photomultiplier tube (9558QA, EMI) in the visible-near-ultrviolet region, or a pyroelectric detector (P1-43K-CC, Molectron) in the infrared region.

The photon-energy calibration of the spectrometer was checked with an intrinsic spectral line of the deuterium lamp, namely the β line of the ^2H spectrum. The theoretical value of the photon energy of the line can be calculated from

$$E_{th} = R_D \left(\frac{1}{2^2} - \frac{1}{4^2}\right) \qquad (2.1)$$

where R_D = 13.6021 eV is the Rydberg constant for ^2H. The calculated photon energy is 2.5504 eV. Figure 2.1 shows the measured spectrum of this spectral line. The peak energy is located at 2.5505±0.0005 eV, which agrees very well with the theoretical value. Figure 2.1 also exhibits a good spectral resolution. When the slit width increases from 500 μm to 700 μm, the full width at half maximum of the peak (FWHM) increases from 6.3×10^{-3} eV to 8.7×10^{-3} eV. This is in agreement with the spectral resolution, $\Delta E/E = 1\times10^{-3}$, of the 16U spectrometer with a slit width of 180 μm at 2.5 eV, estimated by Cummings [1982] and by

Hoffman [1982]. The slit width used in our measurements was typically 700 μm, which is well suited for the measurements on GaAs. The "fine structure" of the reflectivity spectrum of crystal GaAs, namely the doublet at about 3 eV resulting from the spin-orbit splitting of the valence band, is about 0.2 eV, while the spectral resolution is about 0.01 eV at this photon energy with a slit width of 700 μm.

It should be pointed out that the original 16U spectrometer had a very high parasitic light level at photon energies above 5 eV. This parasitic light was found to be caused mainly by two factors. First, the spectrometer was supposed to operate without the first stage at photon energies above 5 eV. This allowed unwanted light (with the photon energies other than those of interest) to pass through the entrance slit of the second-stage monochromator, and to be scattered by defects on the mirrors and on the grating. The light intensity above 5 eV is orders of magnitude weaker than that with lower photon energies. This made the signal-to-noise ratio very small. The second factor was that an intense light beam with slightly lower photon energy than the "dialed" photon energy was diffracted by the grating to a slightly different angle than the desired beam, and it was then blocked by the exit slit blades. But the exit slit blades

reflected much of this light back to a mirror in front of the slit, and the mirror in turn scattered some of it to the opening of the exit slit. The first problem was solved by using the prism monochromator, which eliminated the majority of the unwanted light. The second problem was taken care of by blackening the exit slit blades.

2.1.2 Spectrometer Automation

The original spectrometer was driven by a servo motor, coupled with a strip chart recorder as the data recording device. This old electronic system was completely upgraded through computer automation using a NEC APCIII personal computer as the core device.

Figure 2.2 schematically shows the automated spectrometer. The wavelength driver consists of two stepping motors, shown as motors 1 and 2 in Fig. 2.2. Motor 1 controls the prism in the first stage monochromator, and motor 2 drives the grating in the second stage monochromator. Light with the desired photon energy is selected by coordinating the two motors through a computer program. The new data acquisition system is composed of a light detector and a lock-in amplifier which is interfaced with the computer.

The stepping motors (CX57-83, Compumotor) are directly driven by their indexer/drives (model CX,

Compumotor) which were controlled by the APCIII computer through one of its two additionally installed RS-232C serial interfaces (APC-H156 dual-port RS-232C). The two drives, identified by their own addresses, were daisy-chained on the same RS-232C port, and all the motors and the drives shared the same power supply unit. (The motors and the drives use different voltage outputs!) Like most common peripheral devices, the drive recognizes only its own commands (language). These commands can be sent to the drives, however, by using any common computer language, through an interface. The angular resolution of the stepping motor is 1.8°/full step. This corresponds to, for the 16U spectrometer, about 1×10^{-3} eV in the near-ultraviolet region (with the 2880/mm grating), 5×10^{-4} eV in the visible region (with the 1440/mm grating), and a better resolution in the infrared region. This resolution is about the same as, or better than, the optical spectral resolution estimated in the above subsection.

The interface to the lock-in amplifier (model 5207, EG&G) was done through the other port of the dual-port RS-232C board of the APCIII computer. The amplifier receives the voltage output from the detector which converts the chopped optical signal into an electrical signal. The amplifier then filters out noise and interference from frequencies other than that of the

signal, and provides a stable, low noise output. The amplifier can be controlled with its front-panel keys or via its built-in programmable interface. Among the large number of control parameters of the amplifier, the sensitivity and the time constant should be handled with special care. The time constant should be set in accord with the level of the random noise. The sensitivity should be adjusted such that a full sensitivity capacity can be realized without output overloading.

The spectrometer operation process is illustrated as a flow chart in Fig. 2.3. The experiment starts with an initial procedure which consists of a number of steps. The first step is device power on, including the light source, the beam chopper, the detector, the lock-in amplifier, the stepping motor/drives, and the APCIII computer (see Table 2.1 for source/detector selection). Second, some of the devices need a warm-up period, about 1/2 hour to 1 hour. Meanwhile, the sample should be mounted. The sample holder has been designed to provide convenient sample mounting. It has a separate piece to which the sample is attached. This piece is mounted to the holder base via three pins, and can be simply lifted up or slipped on with very precise re-positioning.

Once the initial procedure is completed, the spectrometer operation software is ready to be executed.

The program is written in the BASIC language, and is intended to be user friendly and self-explanatory. It is written in a prompt-driven format which provides an easily understandable and controllable environment to the user. It also provides convenient access to optional parameters and procedures. The complete program is given in Appendix 2.1 of the present dissertation.

The software can be used for measurements of reflectivity, transmission, and beam intensity. It performs on-time data conversion, that is, for reflectivity or transmission measurements, raw intensity data received from the amplifier is converted to the measured quantity while the spectrometer is running. Therefore, for reflectivity and transmission measurements, certain auxiliary files need to be pre-arranged. For transmission measurements, an intensity reference data file must be pre-measured and stored, and will be invoked when the transmittance is calculated, $T = I/I_{ref}$, where I is the measured intensity and I_{ref} is the source reference intensity. Similarly, two reference files are needed for reflectivity measurements, because

$$R = R_m \, I/I_m \ , \qquad (2.2)$$

where I is the measured intensity, I_m is the intensity recorded when the sample is replaced by a mirror (see

Fig. 2.2), and R_m is the reflectivity of the mirror.

An additional auxiliary file is needed when one measures the reflectivity of a small size sample. The cross section of the beam focused on the sample is about 2 mm × 10 mm. For a small zise sample, say 3×3 mm^2, the reflected/scattered light from the beam mask makes a considerable contribution to the signal received by the detector. In a region in which the sample has low reflectivity while the mask has relatively high reflectivity (though it is blackened) the mask signal can be as much as 20 percent of the the total intensity. This problem has been corrected for by subtracting from the total intensity the mask signal, which again should be pre-measured and stored in an auxiliary file to be invoked by the program. The subtraction is performed on-time using the following equation:

$$R = \frac{I - I_{mask}}{I_m - I_{mask}} R_m \quad . \tag{2.3}$$

Once the program is started, the user can simply follow the menus and the prompts on the CRT screen. In the intensity measurement mode, the user will be prompted for measurement range and the number of data points in the range. The software then commands the stepping motors to position the prism (if used, otherwise it asks for the proper filter) and the grating to the photon energy of the

first data point. (The prism and grating are abbreviated as P&G in the flowchart.) In the transmission or reflectivity measurement modes, on the other hand, the user will be prompted for the auxiliary files, and the measurement range and the number of data points are set to be the same as those in the auxiliary files. The spectrometer scans from high photon energy to low photon energy.

The graphic view port on the CRT screen should be set by invoking a plot subroutine residing in the software. Each point of the data, once it is taken and converted to the measured quantity, will be plotted on the screen. Should multiple scans be needed, data averaging will be automatically taken, and the averaged data will be plotted. A menu is provided to prompt for certain scan-control parameters such as the number of scans and the number of raw data inputs to be averaged (in addition to the time constant of the amplifier). Because of the wide measurement range, the signal intensity may vary by as much as four orders of magnitude. It is thus necessary to adjust the sensitivity of the amplifier. A section of the program is devoted to monitoring, and adjusting when necessary, the amplifier gain to ensure the best compatibility between the signal and the sensitivity. After each scan, the measured data are temporarily stored

in a file in case of any accidental program termination. The final data can be stored in a floppy disk or in the hard disk of the computer, or be plotted.

The software also contains an auto-patch routine. For measurements over a wide spectral range, it is necessary to use more than one set of spectrometer elements. For instance, both the deuterium lamp and the tungsten lamp are needed in a measurement ranging from 2 eV to 6 eV. A small mismatch, or discontinuity, in the measured spectrum is expected when one switches from one element to another. The auto-patch routine allows the spectrometer to run with an overlap of a few data points when the user changes the element. The routine then patches together the data taken with the two elements and provides a continuous spectrum.

The software was written to be as detailed as possible, and it was also intended to be as transparent as possible to the user. The software is certainly not perfect, but it is a user-friendly package that performs a number of services for the user of the spectrometer.

2.1.3 Mirror Reflectivity Calibration

It was mentioned in the above section that, for reflectivity measurements, a mirror reflectivity reference is needed (see Eqs. 2.2 and 2.3.). Therefore a calibrated mirror is required to serve as the reference standard for

reflectivity measurements. The reference mirror used in this study is an aluminum mirror which has been calibrated in two ways in the visible-near-ultraviolet (vis-near-uv) spectral region.

The first calibration method is rather straightforward. First, the mirror M2 in Fig. 2.2 is moved to the right to be aligned with the axis of the detector, and the sample is removed. Then the intensity received by the detector, I_s, is recorded, and stored. A second measurement is carried out with the original setup as shown in Fig. 2.2, except that the sample is replaced with the reference mirror M4 which is from the same batch as, and should be identical to, mirror M3. The beam is then reflected by the two identical mirrors before it reaches the detector. The beam intensity, $I = I_s R_m^2$, is thus recorded, and converted to the mirror reflectivity:

$$R_m = (I/I_s)^{1/2} . \qquad (2.4)$$

Figure 2.4a shows the reflectivity spectrum of the aluminum mirror obtained using Eq. 2.4. Measurement errors are expected because the beam has to be re-oriented for the two measurements while the I_s is assumed to be the same.

The second calibration method involves a secondary standard specimen with known reflectivity. The reflectivity spectrum of oxide-free c-GaAs reported by

Aspnes and Studna [1983] was used as our reference standard. Such a reference choice provides an additional advantage in the reflectivity measurements of our GaAs samples, which are the main targets of this study. All the GaAs samples in this study were exposed to air, and thus each such samples has a thin oxide layer present on the sample surface. The oxide layer is known to modify the observed reflectivity, especially at photon energies above 4.5 eV.[Aspnes and Studna 1983, Lautenschlager 1987] By using the oxide-free c-GaAs reflectivity spectrum, the effect of the oxide layer is absorbed into the mirror reflectivity spectrum:

$$R_m = R_c^A \frac{I_m}{I_c^o} . \qquad (2.5)$$

Here I_m is the beam intensity recorded with the sample in Fig. 2.2 replaced by the aluminum mirror, I_c^o is the beam intensity recorded with an air-exposed c-GaAs specimen as the sample, and R_c^A is the reflectivity of the oxide-free c-GaAs [Aspnes and Studna 1983]. The mirror reflectivity spectrum obtained with Eq. 2.5 is shown in Fig. 2.4b. Considerable deviation between the two spectra in Fig. 2.4 is apparent, indicating the effect of the oxide layer on the surface of c-GaAs. (It should be noted that larger measurement errors are expected for the

spectrum in Fig. 2.4a than for that in Fig. 2.4b.) The reflectivity spectrum in Fig. 2.4b was used as our reference in reflectivity measurements of our GaAs samples. The use of such a mirror reference has the effect of "optically removing" the oxide layer of our c-GaAs samples. But it is expected to be only approximate for our ion-processed GaAs samples. The error in reflectivity is estimated to be at worst 3 percent for photon energies above 5 eV, and much less below 4 eV. The measurement range was cut off at 5.6 eV in order to avoid the least reliable region. Also, no additional structure occurs for GaAs between 5.6 and 6.2 eV. All of the reflectivity results reported here were obtained with this mirror reference, unless otherwise noted.

Figure 2.5 illustrates the reflectivity spectra of crystalline GaAs taken with the IR-near-UV spectrometer. The measurements were carried out at different temperatures: 297° K (room temperature), 120° K, and 40° K, as denoted in the figure. Low temperature measurements were performed with the sample placed in the cryostat, which is equipped with fused-quartz windows. The temperature was controlled with a cryogenic thermometer/controller (model 4075, Palm Beach Cryophysics), and its variation was less than 1° K during the measurement. The spectral region of Fig. 2.4 is from

1.6 eV to 5.6 eV, corresponding to interband electronic transitions of c-GaAs (see Chapter 1).

Demonstrated in Fig. 2.6 is the transmittance spectrum of a $Bi_2Sr_2Ca_1Cu_2O_y$ thin film, a high-temperature superconductor sample prepared by Y. Y. Wang and A. L. Ritter at Virginia Tech. The spectrum, taken at room temperature, covers a wide spectral range, from 0.2 eV to 6 eV.

2.2 Raman Spectrometer

The Raman spectrometer employed in this study has been described in great detail previously [Holtz 1987]. Only a brief account of the equipment is given here.

The laser sources used in the Raman scattering measurements consist of an Argon-ion laser (Innova 90-5, Coherent) and a Krypton-ion laser (Innova 90-K, Coherent). Both lasers provide continuous wave light with discrete photon energies (discrete laser lines). The Argon-laser lines cover the wavelength region from 4579 Å to 5145 Å, or 2.71 eV to 2.41 eV, while the Krypton-laser lines expand the region to 7993 Å, or 1.55 eV with special optics. The available laser lines are listed in Table 2.2.

The laser beam emitted from the laser head is filtered by use of a grating filter to eliminate spurious plasma lines and dispersed light. The beam is then

directed toward, and focused on, the sample in a near-back-scattering geometry. [Holtz 1987] Figure 2.7 (adapted from Holtz 1987) illustrates this scattering geometry. Back-scattering geometry is commonly used for measurements of opaque materials, such as GaAs in the visible region. With this near-back-scattering setup, a sample with a mirror-like surface, like a GaAs wafer, reflects the main beam out of the spectrometer, thus greatly reducing stray light.

The scattered Raman signal is collected, analyzed, and recorded using a SPEX 1403 spectrometer. The light collecting chamber of the spectrometer contains an f/1.4 elliptical mirror which focuses the scattered signal onto the entrance slit of the monochromator of the spectrometer. The SPEX 1403 spectrometer uses a high resolution, low stray light, double monochromator with a full spectral range from 11,000 cm^{-1} to 31,000 cm^{-1}. The selected signal is focused to a photomultiplier tube detector (model C31034A-02) operating in a photon counting mode. The detector is cooled down to about -20^{0} C using a thermoelectric cooler to reduce its dark count. The spectrometer is running-time automated with its own computer controller (SPEX DATAMATE), which drives the monochromator gratings, collects the output from the detector, and records the data.

Table 2.1 IR-near-UV spectrometer components

Range λ (μ)	Range ħω (eV)	Source	1st stage	2nd stage (grating, lines/mm)	detector
0.20-0.39	6.20-3.20	D_2-lamp	Prism	2880	PMT
0.38-0.83	3.27-1.50	W-lamp	Prism	1440	PMT
0.77-1.03	1.60-1.20	W-lamp	Prism	1440	Pyro
0.88-1.24	1.40-1.00	W-lamp	Prism	640	Pyro
1.18-2.48	1.05-0.50	W-lamp	301-1308	640	Pyro
2.38-4.13	.520-.300	Globar	221-1787	240	Pyro
4.00-6.36	.310-.195	Globar	221-1788	240	Pyro
6.20-10.2	.200-.121	Globar	221-1789	101	Pyro
10.1-16.1	.122-.077	Globar	221-1790	101	Pyro

Table 2.2 Laser lines

λ (μ)	$\hbar\omega$ (eV)	$\bar{\nu}$ (cm^{-1})	Max. Power (mW)
Argon-ion laser			
4579	2.707	21835.5	400
4658	2.662	21468.0	100
4765	2.602	20985.4	600
4880	2.541	20491.0	1500
4965	2.497	20139.6	600
5017	2.471	19930.4	400
5145	2.410	19434.3	2000
Krypton-ion laser			
5682	2.183	17599.7	100
6471	1.916	15453.8	600
6764	1.833	14783.2	150
7525	1.648	13289.9	-
7993	1.551	12510.6	-

FIGURE CAPTIONS

Fig. 2.1 Photon-energy calibration check of the IR-near-UV spectrometer. Plotted are spectra exhibiting the β-line of ^2H, which is an intrinsic line structure superimposed on the continuous spectrum emitted by the deuterium lamp. The peak position at 2.5505 eV agrees very well with the calculated value. The photon-energy resolution is also reflected by the peak width obtained with two typical slit widths, 500 μm and 700 μm.

Fig. 2.2 Schematic diagram of the automated IR-near-UV spectrometer. The setup shown is for reflectivity measurements.

Fig. 2.3 The flow chart of the IR-near-UV spectrometer operation. The operation software is given in Appendix 1 of this dissertation.

Fig. 2.4 Reference spectra of the aluminum mirror reflectivity in the visible-near-UV spectral region. The spectrum in panel (a) is directly measured with the use of two identical Al

mirrors, as discussed in the text. The spectrum in panel (b) was determined using the known reflectivity of c-GaAs as a secondary standard. This reference spectrum folds in the known modification caused by the presence of the thin oxide layer on the surface of air-exposed c-GaAs, and can thus be used only in the reflectivity measurements of GaAs samples.

Fig. 2.5 Reflectivity spectra of c-GaAs measured with the IR-near-UV spectrometer. The spectra were taken at three different temperatures: 297° K (room temperature), 120° K, and 40° K.

Fig. 2.6 Room-temperature transmittance of a $Bi_2Sr_2Ca_1Cu_2O_y$ thin film, a high-temperature superconductor sample prepared by Y. Y. Wang and A. L. Ritter at Virginia Tech.

Fig. 2.7 Schematic of the near-back-scattering geometry for Raman scattering measurements on mirror-surface, opaque samples. (after M. Holtz 1987).

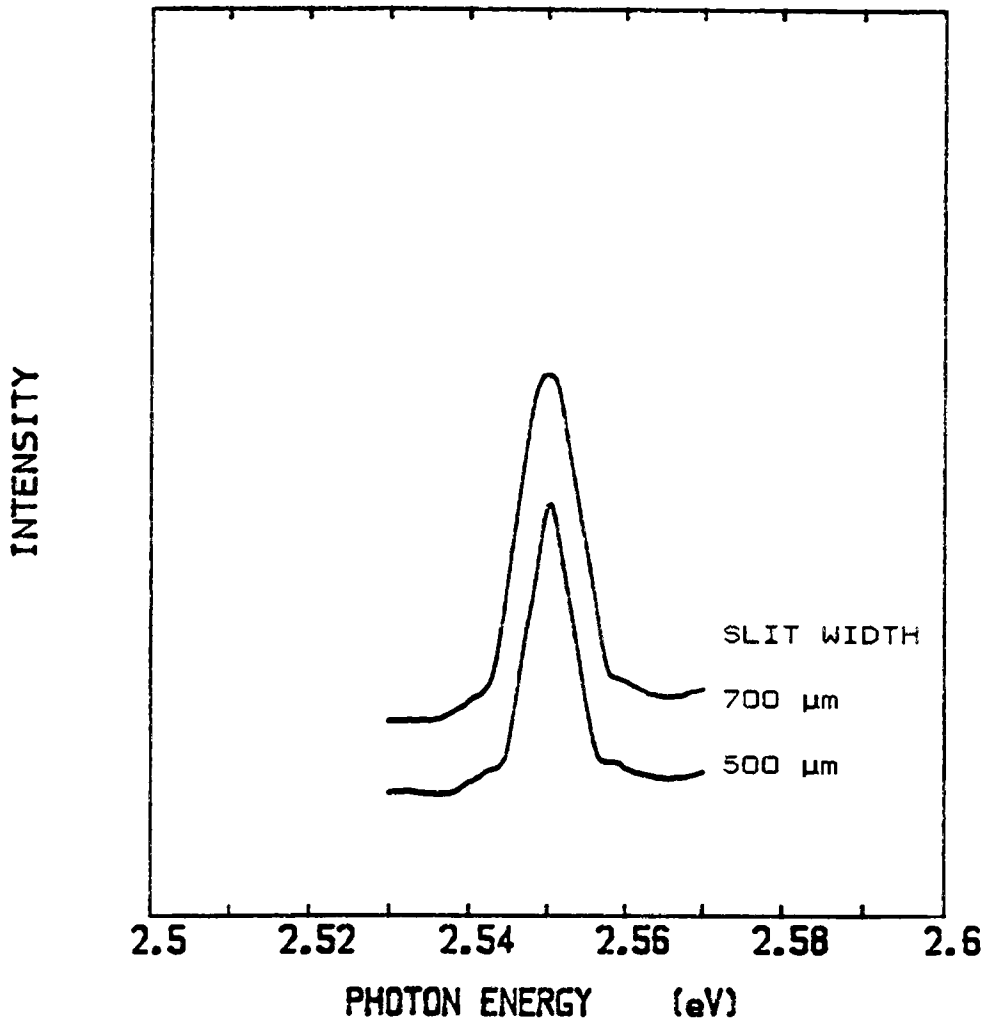

Fig. 2.1 Spectrometer photon-energy calibration check

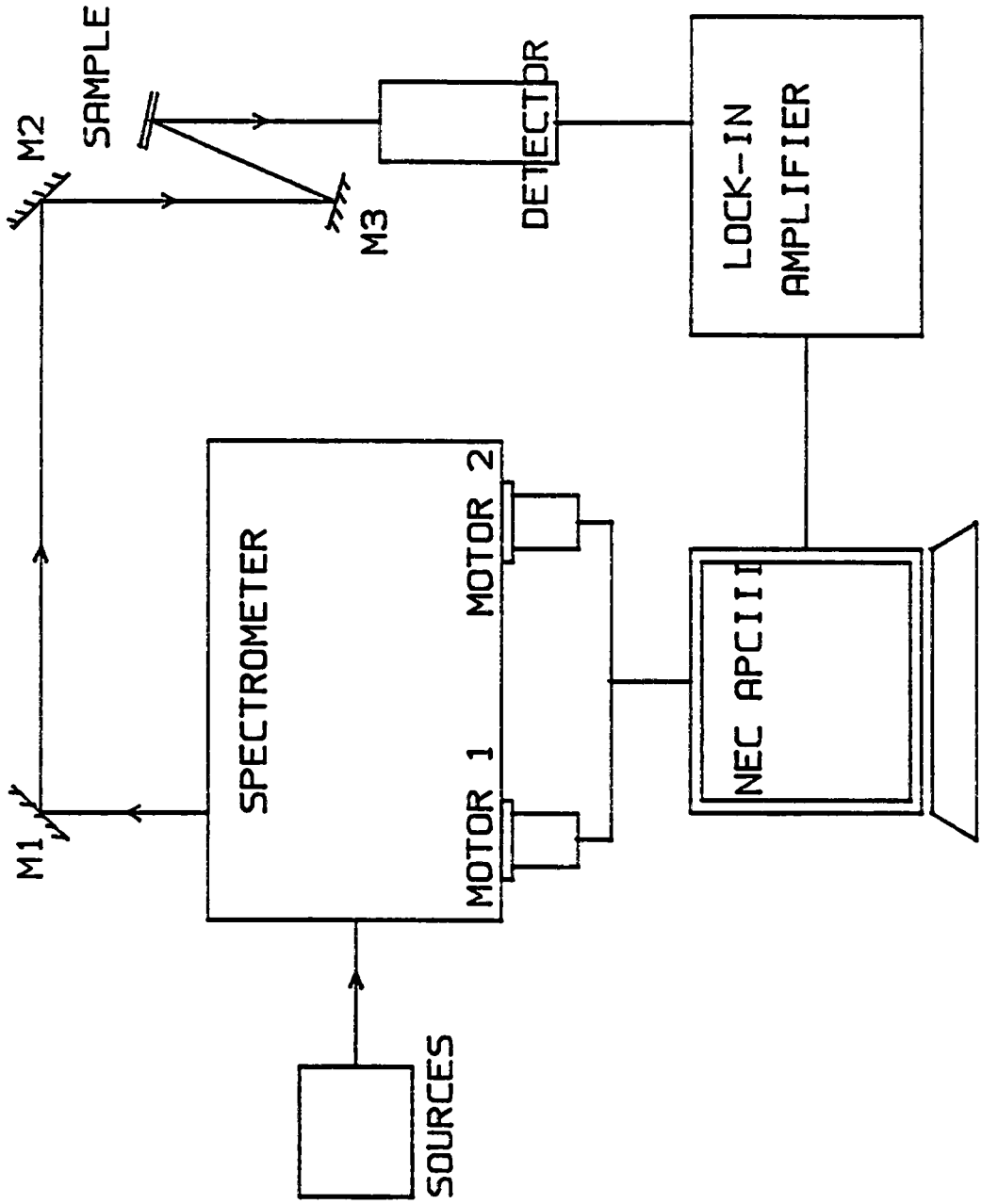

Fig. 2.2 Schematic diagram of the IR-near-UV spectrometer

IR-near-UV Spectrometer Operation Software Flowchart

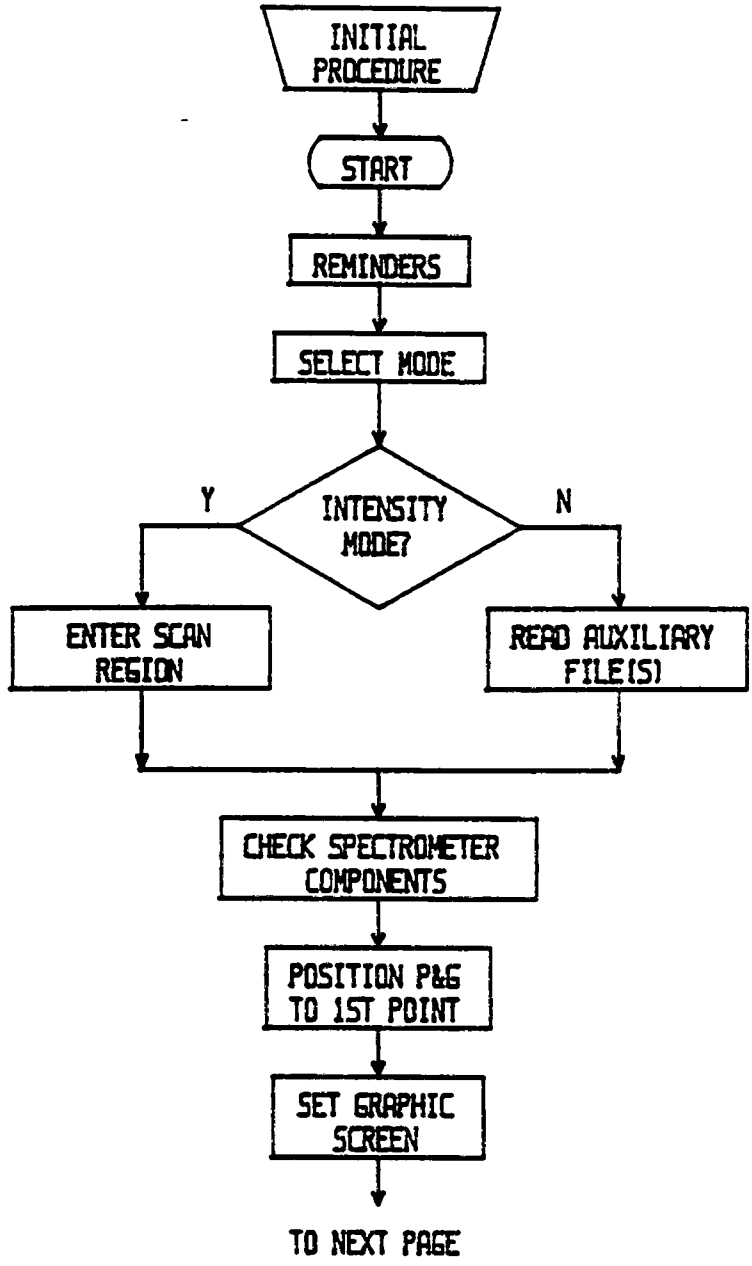

Fig. 2.3 Flow chart of the spectrometer operation

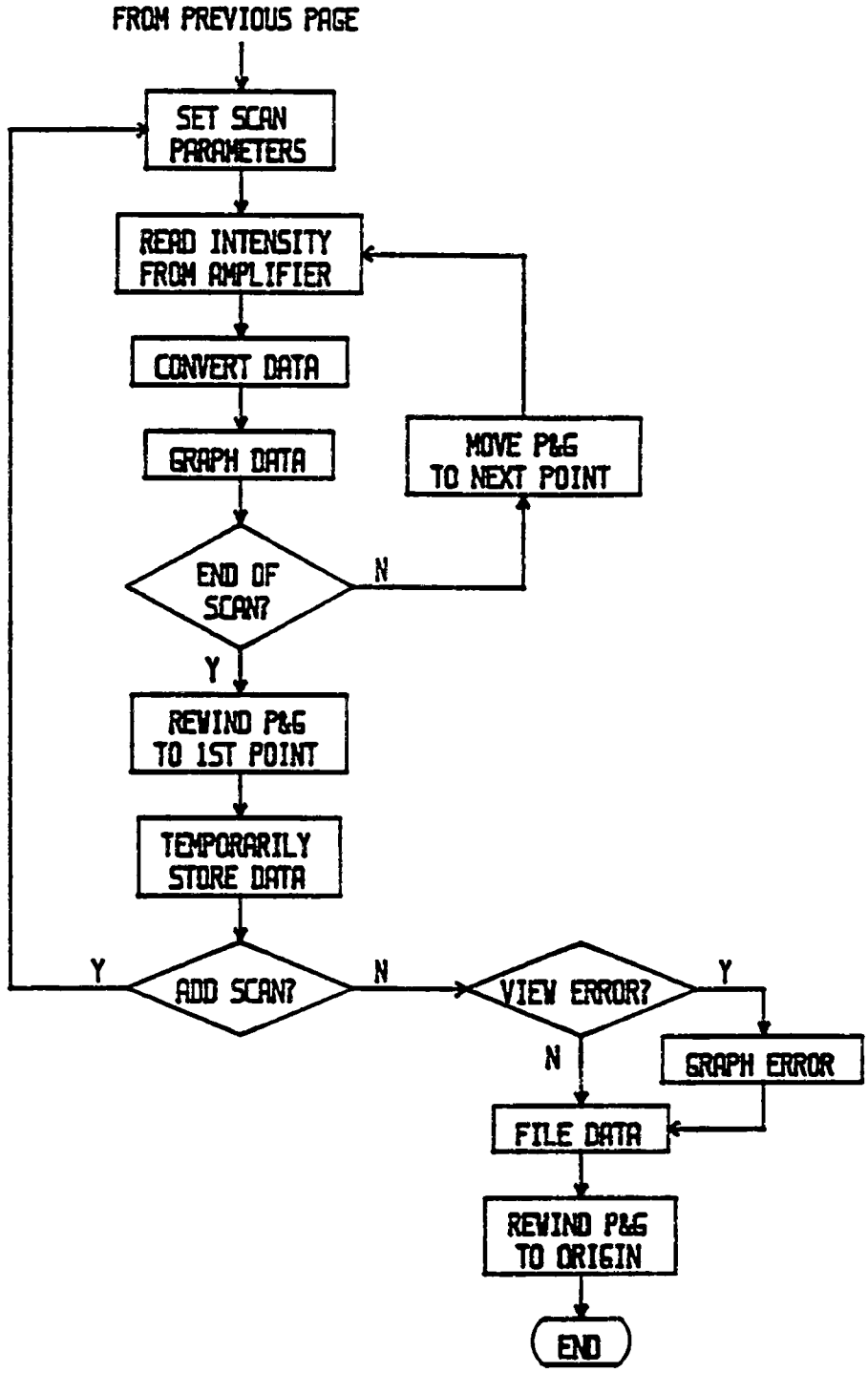

Fig. 2.3 continued

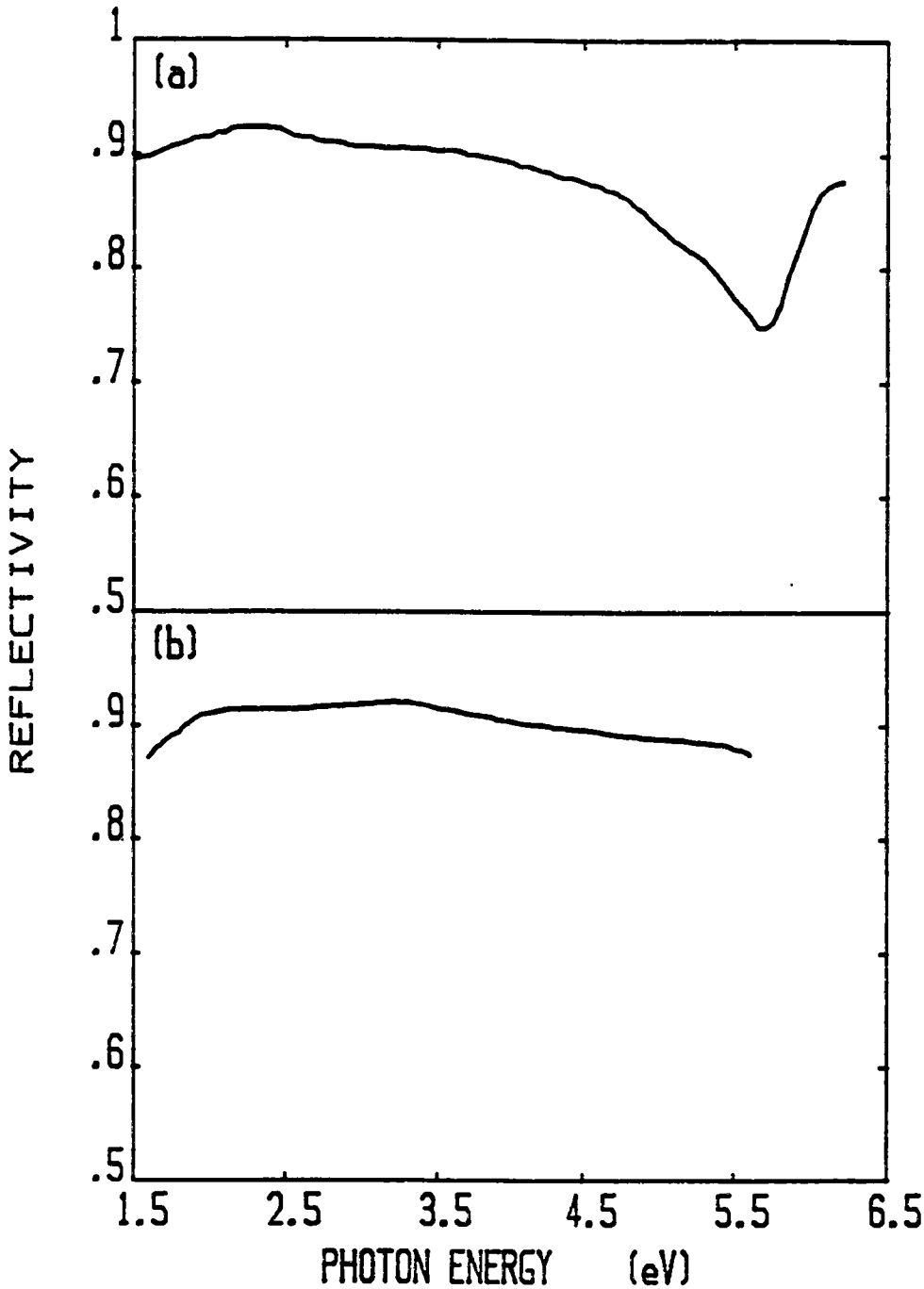

Fig. 2.4 Reference spectra of the Al mirror reflectivity

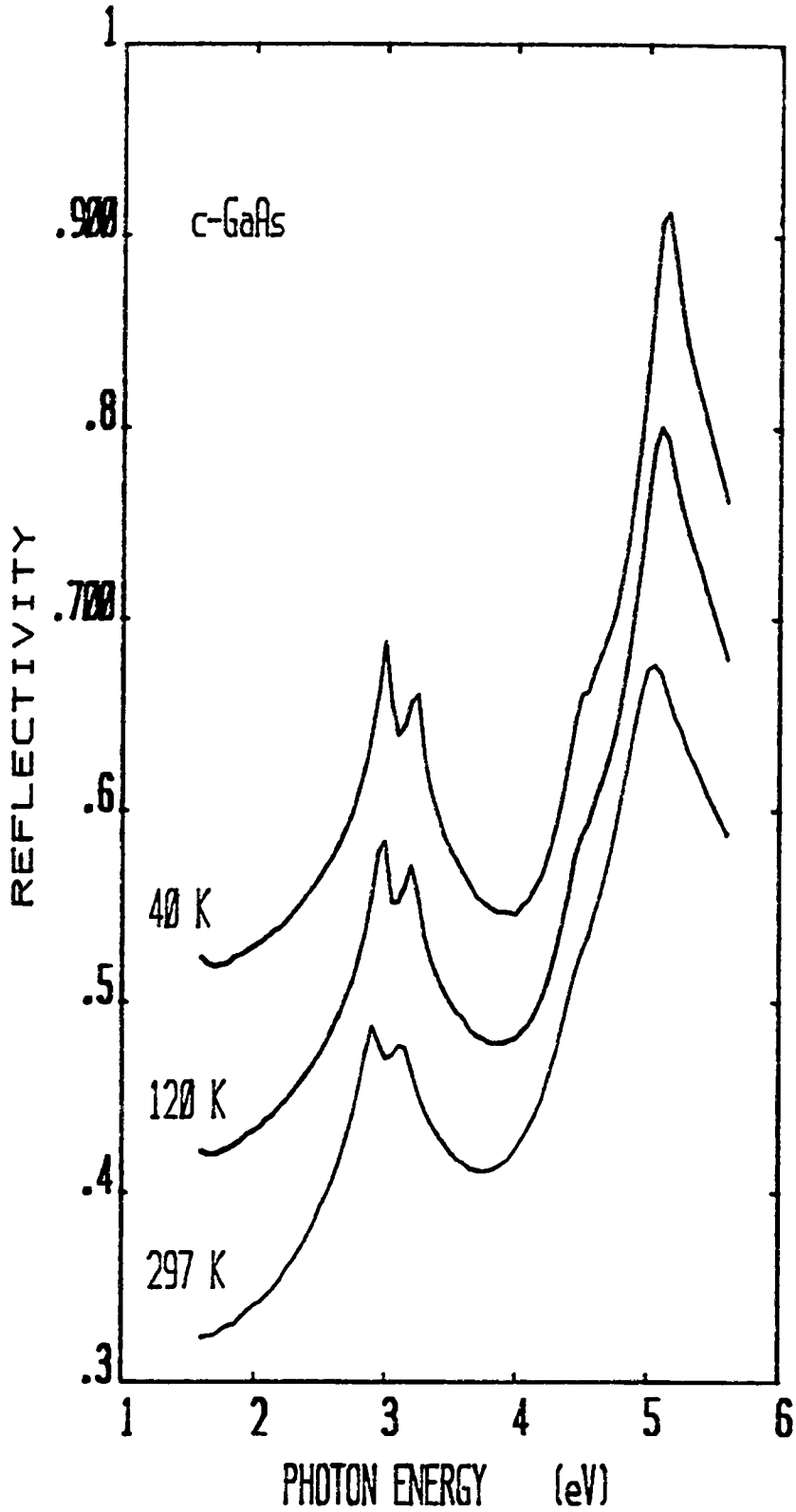

Fig. 2.5 Reflectivity spectra of c-GaAs

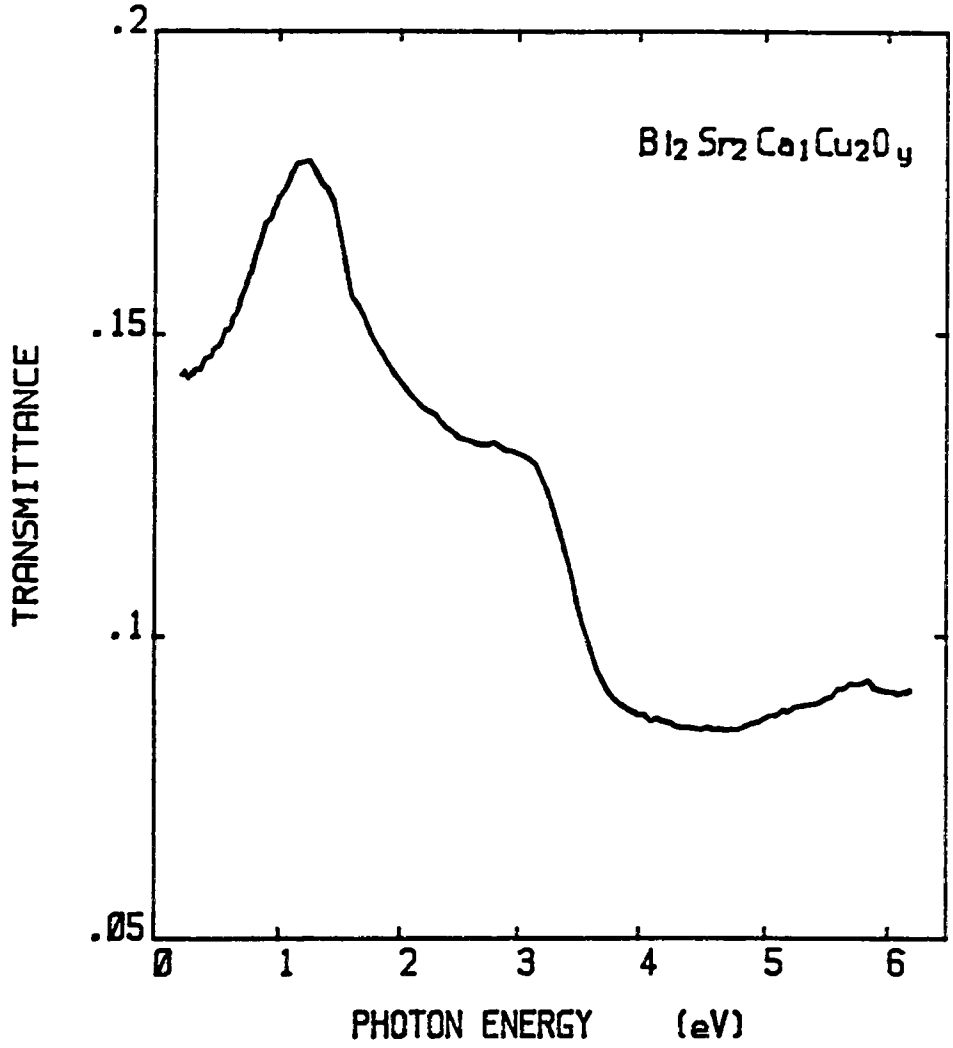

Fig. 2.6 Transmittance of a $Bi_2Sr_2Ca_1Cu_2O$ thin film

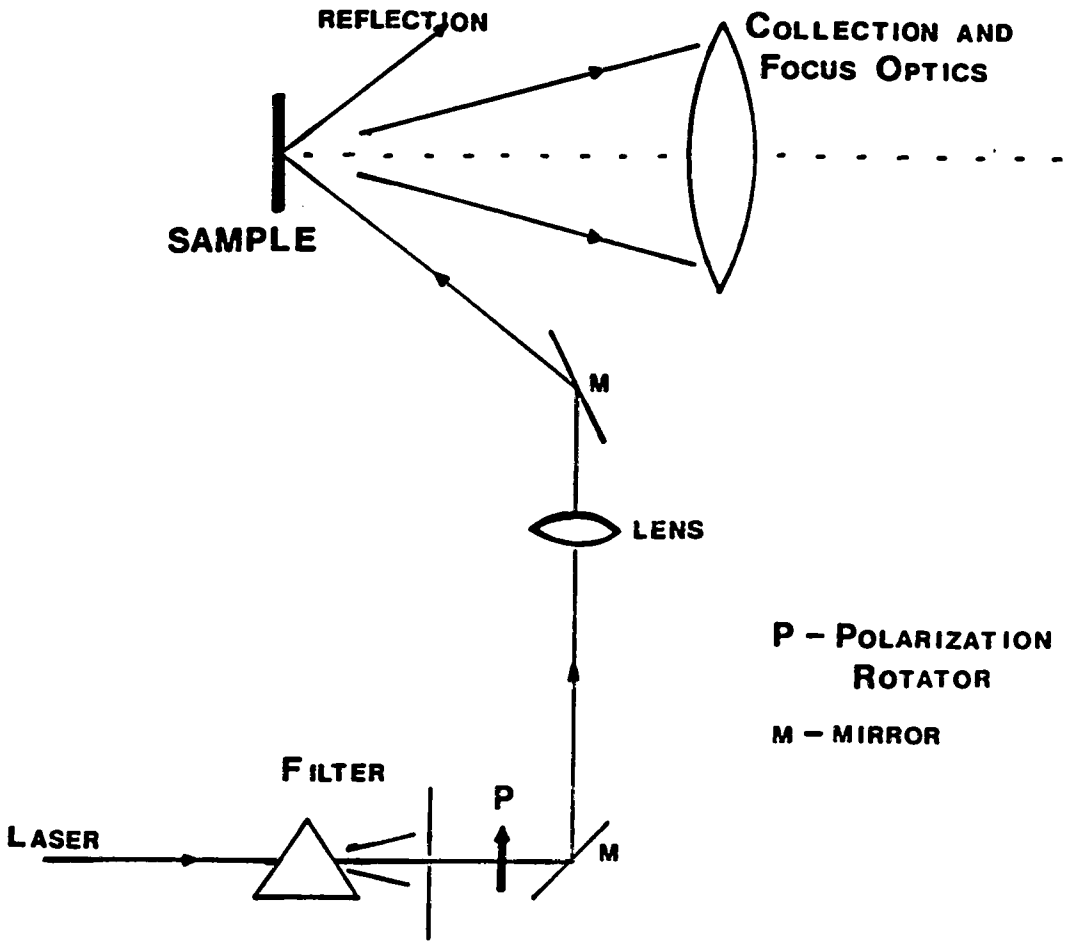

Fig. 2.7 Back-scattering geometry for Raman measurements

CHAPTER 3

FINITE-SIZE EFFECTS IN GaAs MICROCRYSTALS IN Be^+-IMPLANTED GaAs

3.1 Backgroud on Be^+-implanted GaAs

Beryllium is the most widely used acceptor species for GaAs ion implantation [Duncan and Westphal 1985]. It is the lightest p-type dopant for GaAs. In this chapter, the optical properties and the structural characteristics of Be^+-implanted GaAs are investigated by means of visible-ultraviolet reflectance measurements.

Near-surface damage in semiconductors, produced by light-ion species such as B^+ and Be^+, has been studied with various experimental techniques such as ellipsometry [Erman et al. 1984], Raman scattering [Gargouri et al. 1987, Holtz et al. 1988], and transmission electron microscopy [Jones et al. 1988]. Unlike heavy-ion implantation, light-ion implantation at room temperature with moderate energy and fluence (or dose) does not produce a completely amorphized layer [Prussin et al. 1985, Liou et al. 1986, Jones et al. 1988].

In a recent investigation of the near-surface damage layer in unannealed Be^+-implanted GaAs, Holtz at el.

[1988] used a combination of Raman scattering and chemical etch to obtain microstructural information for samples exposed to various fluences. Information derived included the microcrystalline volume fraction, characteristic microcrystal size, and their depth dependence. This chapter presents the results of a visible and ultraviolet optical investigation of the electronic interband spectra for these same Raman-characterized Be^+-implanted GaAs samples. One purpose of these experiments is to determine the effect of microcrystal size in the 100-Å range on the optical properties and electronic excitations of microcrystalline GaAs.

Microcrystalline Si has recently been extensively investigated [Kumar et al. 1986, Richter and Ley 1981, Liu et al. 1984, Veprek et al 1987, Chen et al], but little is known about microcrystalline GaAs (μ-GaAs). The microstructural information available for the Be^+-implanted material provides us with an opportunity to correlate the present optical results on μ-GaAs with microcrystal size, and to make some quantitative statements about finite-size effects in μ-GaAs.

It should be noted that polycrystalline semiconductors with crystallite sizes in the range below 500 Å (say, 50 to 500 Å, or 5 to 50 nm) are usually termed <u>microcrystalline</u> [Kumar et al. 1986, Richter and Ley 1981,

Liu et al. 1984], although nanocrystalline is also sometimes used [Veprek et al. 1987, Chen et al. 1989]. Throughout this paper, the term microcrystalline GaAs (symbolized here by μ-GaAs) is used to denote the crystalline component in the beryllium-implanted GaAs samples, which is known (from the Raman work [Holtz et al. 1988]) to be characterized by microcrystal sizes in this range.

This chapter describes the results of visible-ultraviolet reflectivity measurements which probe the nature of electronic excitations within the damage layer of Be^{+}→GaAs. The semiconductor samples, experimental methods, and observed reflectivity spectra are described in Sec. 3.2. In Sec. 3.3 the optical dielectric function of the damage layer of each implanted material is derived by means of Lorentz-oscillator analysis. The optical properties of μ-GaAs, the microcrystalline component, are extracted in Sec. 3.4 with the use of the effective medium approximation (EMA). The use of the EMA here is somewhat unconventional, as discussed in Sec. 3.5. Section 3.6 presents the main findings on finite-size electronic effects in μ-GaAs. The microcrystallinity-induced spectral changes are concentrated in the linewidths of the three sharp interband peaks; these linewidths increase linearly and rapidly with increasing inverse microcrystal size. A

simple theory, discussed in Secs. 3.7 and 3.8, semi-quantitatively accounts for the present observations. Small microcrystal size implies a short time for an excited carrier to reach, and to be scattered by, the microcrystal boundary, thus limiting the excited-state lifetime and broadening the excited-state energy. An alternative uncertainty-principle argument can be given in terms of confinement-induced $\underline{k}$-space broadening of electron states.

3.2. Ion-implantated Samples, Experiment Methods, and Reflectivity Results

The c-GaAs starting material was Czochralski-grown, chromium-doped, semi-insulating, single-crystal GaAs. (100)-oriented wafers were cut, polished, then etched in 8:1:1 H_2SO_4:30%H_2O_2:H_2O prior to implanting at room temperature. Implantation was carried out at the Texas Instruments Central Research Laboratory in Dallas, using 45-keV Be^+ ions incident at 9° from the normal to avoid channeling. Ion fluences ranged from 10^{13} to 5×10^{14} ions/cm^2. No anneal was done following implantation. The samples were of excellent optical quality; no implantation-induced surface roughness was discernible with laser-beam scattering.

Reflectivity measurements in the visible and

near-ultraviolet region (photon energy E in the range from 2 to 5.6 eV) were performed with the IR-near-UV prism-grating spectrometer described in Chapter 2. Reflectivity was determined via comparison with a calibrated aluminum mirror, using the reflectivity of c-GaAs derived from ellipsometry measurements [Aspnes and Studna 1983] as a reference standard. (See Section 2.1 of Chapter 2.) The thin oxide layer present on the air-exposed c-GaAs sample was "optically removed" with the method described in Sec. 2.1. The same correction was applied to the ion-implanted samples. For these, the correction is expected to be only approximate, as mentioned in that section. The results reported below in Sec. 3.4 may be slightly affected by this, but the effect on the lower energy E_1 and $E_1+\Delta_1$ peaks should be entirely negligible. Photon energy was known within 0.01 eV throughout the spectral region covered in the measurements. All the measurements reported here were carried out at room temperature.

Figure 3.1 displays the results for the reflectivity spectra R(E) of four beryllium-implanted GaAs samples. (Unless otherwise noted, spectra are presented as functions of photon energy $E = \hbar\omega$.) Panels (a), (b), (c), and (d) show the spectra observed after implantation (45-keV Be^+ ions) with fluences of $1x10^{13}$, $5x10^{13}$, $1x10^{14}$,

and $5x10^{14}$ ion/cm^2, respectively. In addition to the experimental data on the ion-implanted samples, indicated by the points, each panel also contains two curves which correspond to the spectra of crystalline GaAs (labelled c) and of amorphous GaAs (labelled a). These two curves are repeated in each panel in order to provide visual benchmarks for the evolution of the GaAs spectrum with increasing implantation dose. The amorphous spectrum shown corresponds to implantation-amorphized GaAs produced by high-fluence high-energy As^+ bombardment [Aspnes, private communication; also see Aspnes et al. 1982]. A systematic spectral change is clear in Fig. 3.1; the higher the ion fluence, the more severe is the deviation from the spectrum of the bulk crystal.

The three prominent peaks in the c-GaAs spectrum of Fig. 3.1 arise from direct ($\underline{k}$-conserving) interband transitions in the vicinity of critical points (parallel bands producing Van Hove singularities, as discussed in Chapter One) within the Brillouin zone. The peaks at 2.9, 3.1, and 4.9 eV correspond, respectively, to direct transitions illustrated as a, b, c in Fig. 1.2. The conventionally accepted notation for the interband energies of these three critical-point features are E_1, $E_1+\Delta_1$, an E_2, respectively [Lautenschlager et al. 1987]. As seen in Fig. 1.2, the splitting Δ_1 of the 3-eV doublet

arises from a splitting (it is caused by spin-orbit interaction) within the Valence band of c-GaAs.

3.3 The Dielectric Function of the Implanted Material

In order to derive the complex dielectric function and the other optical properties from each measured reflectivity spectrum, a Lorentz oscillator expression [Spitzer and Kleinman 1961, Verleur 1968, Erman et al. 1984] was used for the dielectric function. The oscillator expression has been given in Eq. 1.8 in Chapter 1, and is re-written here:

$$\varepsilon(\omega) = \varepsilon_\infty + \sum_{i=1}^{n} \frac{F_i^2}{(\omega_i^2 - \omega^2) - i\Gamma_i \omega} \cdot \qquad (3.1)$$

Reflectivity can be determined directly from the real (ε_1) and imaginary (ε_2) parts of ε: $\varepsilon = \varepsilon_1 + i\varepsilon_2$. In this way, a calculated reflectivity spectrum $R(\omega)$ can be generated from the set of 3n+1 parameters, F_i, ω_i, Γ_i, and ε_∞. The calculated reflectivity spectrum is then compared with the experimental one. A computer program was developed, based on nonlinear least squares fitting [IMSL User's Manual 1984], to obtain the parameter set that gives the best fit of the calculated to the experimental reflectivity spectrum.

An error criterion δ, corresponding to a normalized

average square deviation, was defined as

$$\delta = \frac{\sum_{i=1}^{N} | f_{fit}(\omega_i) - f_{exp}(\omega_i) |^2}{\sum | f_{exp}(\omega_i) |^2} \qquad (3.2)$$

where N is the number of data points, and f is the data function, which can be the reflectivity, the dielectric function, or other functions.

Seven oscillators were needed to fit adequately the reflectivity spectrum of each sample. Seven oscillators were also used in the ellipsometry studies of Erman et al. [1984]. Initially, the idea was to regard the oscillator parameters themselves as convenient intermediaries on route to ε_1 and ε_2, rather than as physically significant quantities in their own right. However, the fitting results showed that three of the oscillators clearly correspond closely to the E_1, $E_1+\Delta_1$, and E_2 direct interband transitions. The effect of implantation on the linewidth parameter Γ of these three oscillators is pronounced and systematic and has definite physical significance; this will be discussed in Secs. 3.7 and 3.8.

The fitting technique was checked by applying it to c-GaAs, for which the reflectivity, the dielectric function, and the other related optical properties are rather accurately known as a result of ellipsometry measurements.[Aspnes and Studna 1983] Oscillator fitting

was carried out on the ellipsometry-derived reflectivity function R(E). The error criterion δ (Eq. 3.2, with f = R) was less than 10^{-4}. The dielectric function $\varepsilon(\omega)$ corresponding (via Eq. 3.1) to the fitted set of oscillator parameters was also compared with the $\varepsilon(\omega)$ values measured ellipsometrically.[Aspnes and Studna 1983] The corresponding error δ (Eq. 3.2, with f = ε, f now is a complex quantity.) was about 10^{-3}. In addition, a different fit was also performed in which the ellipsometry-derived dielectric function, rather than the reflectivity, was the fitted quantity (Eq. 3.2, with f = ε). This yeilded a δ of about 10^{-4}. All of these tests indicate that the fitting procedure is quite satisfactory. It should be noted, however, that the error is not uniformly distributed over all data points; deviations tend to be larger in regions in which either ε_1 or ε_2 is small. In these regions, ellipsometry measurements also involve a large uncertainty.[Aspnes and Studna 1983]

The dielectric functions of the implanted samples and of c-GaAs were obtained in this way by means of oscillator fits of the experimentally measured reflectivity, using seven oscillators for each sample. In all of the fits, the value of the error criterion δ (f = R) was less than 10^{-4}. The real part, $\varepsilon_1(E)$, and the imaginary part, $\varepsilon_2(E)$, of

the dielectric functions of the implanted samples are plotted in Figs. 3.2 and 3.3, respectively, along with their crystal and amorphous counterparts. Again, the a-GaAs spectra are from the work of Aspnes on implantation-amorphized GaAs. The dielectric function is seen to be sensitive to the damage produced by ion implantation. The sharp spectral structures are smeared out as ion fluence increases. These spectral changes are due to two quite distinct effects: the increasing presence of the amorphous phase, and the finite-size effects on the optical properties of the crystalline phase. The first is self-explanatory. We shall concentrate our attention on the second effect.

3.4 Optical Properties of the Microcrystalline Component

The structure of ion-implanted semiconductors is believed to have the nature of a volume mixture of microcrystals and amorphous material.[Richter et al 1981] In particular, recent Raman-scattering studies on the same samples studied here strongly support a structural model of the implantation-induced damage layer as a fine-scale mixture of amorphous and microcrystalline GaAs.[Holtz et al. 1988] Also, these samples (45-keV Be^+ implants to fluences up to $5x10^{14}$ cm^{-2}) were shown, by chemical-etch depth-profile Raman studies [Holtz et al. 1988], to have a

uniform high-damage plateau extending from the surface to a depth of about 1500 Å, followed by a graded transition region. The reflectivity measurements carried out on these samples following chemical-etch removal of near-surface layers show that the UV spectrum exhibits a similar depth profile.

In the reflectivity experiments described in the present work, photon energies exceeded 2 eV (well above the room-temperature bandgap of 1.43 eV) and the optical penetration depth for this strongly-absorbed light was less than the plateau depth. This means that a region with macroscopically uniform structure is being probed. Thus the complication of the graded transition region is avoided. In the transition region, the structure varies with depth from that of the high-damage plateau to that of the undamaged crystalline substrate (for these samples, the transition region spans depths from about 1500 Å to 4000 Å [Holtz et al 1988].) Another significant feature of these samples is that the microcrystalline component dominates the damage layer.

The Bruggeman effective medium approximation (EMA) described in Chapter 1 has been used to characterize this the damage layer. When applied to the ion-implanted two-phase medium, EMA (Eq. 1.9 in Chapter 1) takes the form,

$$\frac{\varepsilon - \varepsilon_a}{2\varepsilon + \varepsilon_a} f_a + \frac{\varepsilon - \varepsilon_\mu}{2\varepsilon + \varepsilon_\mu} f_\mu = 0 \qquad (3.4)$$

where ε, ε_μ, and ε_a denote the dielectric functions of the implanted sample, the microcrystalline phase, and the amorphous phase, and f_a and f_μ (f_μ=1-f_a) are the volume fractions of the amorphous and microcrystalline phases, respectively. The dielectric function ε_a of a-GaAs is broad and featureless in this region, and thus it is reasonable to assume that the amorphous component in the implanted material has the same dielectric function. But it is not assumed that the dielectric function of the microcrystalline component, ε_μ, is the same as that of c-GaAs. The sharp spectral features of ε_c are due to interband $\underline{k}$-conserving transitions at critical points in $\underline{k}$-space, and would be expected to be sensitive to finite-size effects in small microcrystals. Therefore, in this thesis, the effective medium approximation has been used to derive ε_μ from the measured ε and the known ε_a.

The dielectric function of the microcrystalline phase is obtained by solving Eq. 3.4 for ε_μ:

$$\varepsilon_\mu = \frac{1 + 2B}{1 - B} \varepsilon \qquad (3.5)$$

where

$$B = \frac{\varepsilon - \varepsilon_a}{2\varepsilon + \varepsilon_a} \frac{f_a}{1-f_a} . \qquad (3.6)$$

In order to obtain f_a, the amorphous volume fraction, it is assumed that away from the sharp interband features of the bulk dielectric function, at 2.9 eV (E_1), 3.1 eV ($E_1+\Delta_1$), and 4.9 eV (E_2), the optical properties of microcrystallites are close to those of the bulk crystal ($\varepsilon_\mu = \varepsilon_c$). This assumption is supported by the good agreement of the f_a values obtained by this procedure (calculated below) with those obtained independently for these samples from the previously mentioned Raman studies [Holtz et al. 1988]. It is also self-consistent, as shown later in the α_μ spectra of Fig. 3.6, where α_μ is the microcrystalline-phase optical absorption coefficient. The amorphous volume fraction of each sample can thus be estimated by using the following simple relation, valid only in spectral regions away from the critical-point features of ε_c, connecting the absorption coefficients of the bulk crystal (α_c), the amorphous phase (α_a), and the implanted material (α):

$$\alpha = \alpha_a \, f_a + \alpha_c \, (1-f_a) \qquad (3.7)$$

The spectral region below 2.5 eV, well below the first strong interband feature at 2.9 eV, was chosen to calculate f_a. In Eq. 3.7, α and α_c are known from the present experiments (determined from the dielectric functions of Figs. 3.2 and 3.3), while α_a is known from

previous work.[Aspnes, private communication] Obviously, α_a and α_c need to be appreciably different from each other, and α must be intermediate between them, in order for Eq. 3.7 to be useful for estimating f_a. These conditions are indeed met in the stated special region, in which α_a is a factor of 4 to 5 larger than α_c, so that Eq. 3.7 does provide a reasonably effective method here for estimating f_a from the absorption coefficients.

The resulting amorphous fractions are listed in Table 3.1, along with the Raman-derived results [Holtz et al. 1988] obtained previously. The last column in the table is the characteristic microcrystallite size L deduced from the Raman measurements by analyzing the size-effect-induced shifting and broadening of the longitudinal-optical phonon line [Holtz et al. 1988]. The amorphous fraction is relatively low, which is consistent with the idea that only light damage is induced by light-ion implantation at room temperature. For the most heavily damaged sample, the crystalline component still accounts for 75-80 percent of the volume fraction. But the Raman-derived characteristic microcrystallite size L is very small; $L \approx 55$ Å for the 5×10^{14} cm^{-2} implant.

The dielectric functions of the microcrystalline phase of the implanted samples, calculated using Eqs. 3.5 and 3.6 and the f_a values in Table 3.1 (column 2), are

presented in Figs. 3.4 and 3.5. These spectra clearly show that the optical properties of μ-GaAs are substantially different than those of c-GaAs, especially in the vicinity of the sharp interband features. The E_1 and $E_1+\Delta_1$ doublet of ε_2 merges into a single peak as crystallite size becomes less than about 200 Å.

The optical absorption spectrum of the microcrystalline component of each sample, denoted as $\alpha_\mu(E)$, was determined in each case from the microcrystalline-phase dielectric function $\varepsilon_\mu(E)$ whose real and imaginary parts were shown in Figs. 3.4 and 3.5. The results for $\alpha_\mu(E)$ are shown in Fig. 3.6, where they are compared with the bulk-crystal spectrum $\alpha_c(E)$. It is clear that below 2.5 eV, α_μ is close to α_c, which is self-consistent with (and thereby supports) the assumption made above in the calculation of f_a. However, throughout much of the spectral range covered in Figs. 3.4-3.6, the optical properties of μ-GaAs are seen to be appreciably different from the optical properties of c-GaAs. This is a key finding of the present investigation.

3.5 Reversal of the EMA

It is important to emphasize that the present application of the effective medium approximation is unconventional. The conventional procedure is to use the

EMA to calculate the optical properties of a composite two-phase medium in terms of the composition and the known optical properties of the individual component phases in bulk form. In the case of a two-phase mixture of crystalline and amorphous GaAs, the procedure would be to use EMA (via Eq. 3.3) to determine the dielectric function of the mixture in terms of the diectric functions of c-GaAs and a-GaAs. The composition (f_c and $f_a = 1 - f_c$) could be used as a parameter to optimize the fit to the measured spectra of the mixture, i.e. the composition could be determined by optimizing the fit. This is not done here.

In the present analysis, the composition (f_a, f_c) was first estimated as described in the previous section, with results consistent with independent estimates obtained earlier in the extensive Raman study by Holtz et al (1988a) on these samples. The EMA was then used to extract the dielectric function of one of the constituent phases, the microcrystalline component, which is treated as the unknown quantity. The dielectric function of the two-phase mixture is known (determined by the present experiments on the implanted samples), the composition of the mixture is known (as already described), and the dielectric function of the amorphous component is taken to be the same as the featureless function characteristic of pure a-GaAs. The dielectric function ε_μ of the microcrystalline component

(μ-GaAs) is then determined by using Eqs. 3.5 and 3.6.

The present analysis is thus focused on the optical properties of μ-GaAs, the microcrystalline component within the damage layer of the implanted GaAs samples. The dielectric function of μ-GaAs is treated as a moving target, different for each differently-implanted sample (i.e. ε_μ changes with ion fluence). The physical reason for this is that ε_μ clearly depends on the characteristic microcrystallite size L within the microcrystalline phase. L is an internal variable which controls the properties of μ-GaAs. L is known from the Raman work, and it changes (Table 3.1) from sample to sample. The present results therefore provide information about the L-dependence of ε_μ. The observed L-dependence will be analyzed in Sec. 3.6 and interpreted in Secs. 3.7 and 3.8.

The fact that ε_μ changes from sample to sample, becoming progressively more and more different from ε_c (the bulk-crystal dielectric function) as L decreases, demonstrates that the conventional form of the EMA is inappropriate for ion-implanted GaAs at high fluences. This conclusion was also reached by Erman et al [1984], who found that the use of ε_c for the crystalline component could not successfully reproduce the optical properties of the implanted material. The present work sheds light on the failure of the conventional EMA procedure, and it also

shows how the EMA can be applied in a different way in order to extract the different-from-the-bulk-crystal optical properties of a fine-grain (small L) microcrystalline component.

3.6 The Effects of Microcrystal Size on the Optical Properties of μ-GaAs

Figures 3.4, 3.5, and 3.6, which display the results for the optical properties of μ-GaAs, the microcrystalline phase that is the main component within the near-surface damage layer of the implanted GaAs samples, exhibit a clear evolution with decreasing microcrystal size. To quantitatively characterize this evolution, a second oscillator analysis was now performed on the microcrystalline-phase dielectric function ε_μ, for each of the μ-GaAs phases studied. As mentioned earlier, the oscillator parameters themselves have thus far been viewed merely as convenient intermediaries on route to the dielectric function. This time, however, we know the dielectric function (the EMA-derived ε_μ whose real and imaginary parts have been presented in Figs. 3.4 and 3.5). We carry out an oscillator fit to ε_μ, using Eq. 3.1, specifically to determine the oscillator parameters and to examine the changes in these parameters as the characteristic size L changes. Since these parameters

quantitatively characterize the spectra in a consistent way, systematic microcrystallinity-induced changes should be significant.

Table 3.2 compares the oscillator parameters found for c-GaAs and for the μ-GaAs phase in the $5x10^{14}$ cm^{-2}, 45-keV, Be^+ implant. This corresponds to the comparison between the c-GaAs and μ-GaAs spectra shown in panel (d) of Figs. 3.4-3.6. For this μ-GaAs sample, the microcrystalline component of sample (d), the characteristic microcrystal size is about 55 Å (Table 3.1).

A quick review of the road to Table 3.2 is in order. Oscillator analysis of the measured reflectivity (Fig. 3.1) was used to determine the dielectric function (Figs. 3.2 and 3.3) of the implanted material. Effective-medium analysis (Eqs. 3.5 and 3.6) was then used to extract the dielectric function ε_μ of the μ-GaAs component, using the composition (f_μ, f_a) and dielectric function of the implanted material and the known dielectric function ε_a of a-GaAs. Finally, in order to track the changes that occur with decreasing L, oscillator parameters were fitted to the ε_μ spectra of Figs. 3.4 and 3.5.

Among the oscillators listed in Table 3.2, three have especially small (less than 0.4 eV) c-GaAs linewidth

values Γ_1(c). These three oscillators correspond closely to the three prominent sharp features in the crystalline spectrum. They are readily identified with the direct interband transitions, E_1, $E_1+\Delta_1$, and E_2, and their oscillator energies of 2.92, 3.12, and 4.85 eV are close to the accepted room-temperature transition energies [Lautenschlager et al. 1987]. We shall focus our attention on these three (labelled) rows in Table 3.2. Microcrystallinity scarcely affects these energies; $E_1(\mu)$ differs from E_1(c) by no more than 0.04 eV for these three oscillators, and these differences are not viewed as of experimental significance. Skipping over to the last two columns, we see definite c→μ changes (10-15%, both signs) in the fitted F_1 values. However, these F_1 changes, like the E_1 changes, are overshadowed by the striking changes manifest in the middle two columns of the table, and they are discussed in detail in the remainder of this chapter.

By far the most pronounced microcrystallinity-induced (c→μ) changes seen in Table 3.2 are those found for the Γ values contained in the three labelled rows. The linewidth parameter nearly triples for E_1, increases by 50% for $E_1+\Delta_1$, and doubles for E_2. These three Γ_1's experience the largest relative changes from the crystalline values among the 22 oscillator parameters listed. The finite-size effects, which produce the progressive departure from the

crystal spectrum of the μ-GaAs spectra of Figs. 3.4-3.6 (increasing in each instance, with decreasing microcrystallite size, in the sequence a→b→c→d), are concentrated in these three quantities. Thus the changes in these Γ's must be taken seriously, since they appear to epitomize the c→μ spectral evolution exhibited in Figs. 3.4-3.6.

Figure 3.7 displays a graphic representation of the microcrystallinity-induced variation in these linewidth parameters. The horizontal axis is 1/L, the reciprocal of the characteristic crystallite size. Evidence that L^{-1} provides a useful measure of microcrystallinity was found in the earlier Raman-scattering studies on these materials [Holtz et al. 1988]. The three small-L values plotted at the right and center of Fig. 3.7 correspond to the Raman-derived L's listed in Table 3.1 for the three high-implant samples. The points plotted on the left-hand axis correspond, of course, to the bulk crystal (c-GaAs, $L = \infty$). The L value for the light implant (first row of Table 3.1) was not independently obtained, but is an interpolated estimate based on the observed Γ and the linear $\Gamma(L^{-1})$ dependence for the case of the E_1 oscillator. Using the crude estimate so obtained for this L yields the two points plotted for $E_1+\Delta_1$ and E_2, which are seen to be reasonably consistent with the rest of the

data.

For each interband-transition oscillator, the linewidth Γ can be expressed as the sum of two terms:

$$\Gamma = \Gamma_0 + \Gamma_{size} \ . \qquad (3.8)$$

Here Γ is the linewidth measured for a microcrystalline sample (μ-GaAs), Γ_0 is the linewidth measured for the bulk crystal (c-GaAs), and Γ_{size} is the additional size-effect broadening contributed to the linewidth in GaAs microcrystals by the effect of finite size. From Fig. 3.7 it is clear that, within the experimental error, Γ_{size} is proportional to the reciprocal of the characteristic microcrystal size:

$$\Gamma_{size} = A/L \ , \qquad (3.9)$$

so that

$$\Gamma = \Gamma_0 + A/L \ . \qquad (3.10)$$

Here A is a constant corresponding to the slope of the appropriate line in Fig. 3.7. The A values are listed in Table 3.3.

Before discussing interpretations of and mechanisms for the second term on the right-hand side of Eq. 3.10, a brief comment is worth noting about the first term, the "intrinsic" (bulk crystal) term Γ_0. The sharp features in the dielectric function originate from the corresponding

sharp features in the joint density-of-states for direct (or "vertical" or $\underline{k}$-conserving, see Fig. 1.2) electronic transitions from the valence band to the conduction band. The joint density-of-states is a continuous function $\rho_{cv}(E)$ and the shape (and effective spectral width) of each critical- point feature arises from the band structure $E_{cv}(\underline{k})$ in the vicinity of the contributing critical point(s) in $\underline{k}$-space. In addition, there are mechanisms in the bulk crystal (carrier-phonon interaction, carrier-carrier interactions, etc.) which serve to limit the lifetimes of the optically induced electron-hole excited states and which introduce additional broadening into the observed linewidth. The combined linewidth arising from $\rho_{cv}(E)$ and the superimposed lifetime-limitation broadening is the "intrinsic" linewidth Γ_0 which characterizes the bulk-crystal interband feature in room-temperature c-GaAs. The main focus here is on the additional broadening Γ_{size} introduced by the microcrystalline graininess in μ-GaAs, as manifested in Fig. 3.7 and the second term on the right-hand side of Eqs. 3.8 and 3.10.

3.7 Finite-Size Effects in μ-GaAs: Lifetime Limitation Mechanism

The discussion contained in the preceding paragraph suggests that a lifetime-limitation mechanism may account for the finite-size effects observed in μ-GaAs. The proximity of the microcrystal boundary to the optically excited electron and hole provides a natural mechanism. This section present a simple semi-quantitative theory, invoking the uncertainty principle, for the spectral effect of the carrier-boundary interaction.

The basic idea is that a collision with the microcrystal boundary scatters an optically excited carrier into another state, limiting the excited-state lifetime. Let the excited carriers possess a characteristic velocity v. Then a rough estimate of the average time τ it takes for an excited electron (or hole) to "feel" the boundary in a microcrystal of size L is

$$\tau = (L/2)/v \qquad (3.11)$$

For sufficiently small L, τ will become smaller than the lifetime associated with the competing processes, and will dominate the excited-state lifetime. From the uncertainty principle, the consequent energy broadening is

$$\tau \, \Delta E = h \ , \qquad (3.12)$$

where h is Plank's constant. Combining Eqs. 3.11 and 3.12 yields

$$\Delta E = 2h\nu \frac{1}{L} . \qquad (3.13)$$

By identifying ΔE with Γ_{size}, the size-effect contribution to the spectral linewidth Γ observed in microcrystalline material, Eq. 3.8 becomes

$$\Gamma = \Gamma_0 + 4\pi\hbar\nu \frac{1}{L} . \qquad (3.14)$$

This equation has precisely the form of the experimentally observed relation, Eq. 3.10. Equating A with $4\pi\hbar\nu$ yields

$$\nu = \frac{A}{4\pi\hbar} . \qquad (3.15)$$

Table 3.3 lists the velocities implied by Eq. 3.15 and the experimental values for A. As discussed in the following section, these velocities are reasonably consistent (given the quantitative limitations of this envelope-scale calculation) with group velocities derived from the c-GaAs band structure. The main point here, however, is the success of this model in generating the linear relation connecting Γ and L^{-1} (Eq. 3.14), in agreement with the principal experimental results (Fig. 3.7, Eq. 3.10).

Also included in Table 3.3 are values of the

size-effect lifetime $\tau(L)$ for L = 100 Å, representative of the range of the samples (corresponding to the L^{-1} value which bisects Fig. 3.7). These short lifetimes, in the 10^{-14} s range, are estimated from Eq. 3.11 and the optically derived velocities (Eq. 3.15). In this regime of microcrystallinity, the finite-size effect is the dominant excited-state lifetime limitation.

3.8 Finite -size Effects in μ-GaAs: *k*-Vector Broadening Mechanism

This section presents a different viewpoint on the finite-size effects in μ-GaAs, one which focuses on the departure of the electron states from Bloch states. Each band $E(\underline{k})$ in a crystal is not quite continuous but is defined on a very fine grid in $\underline{k}$-space with grid spacing $2\pi/L$, where L is the crystal size. In a microcrystal, with L of the order of 10^2 Å, the grid is coarse and can no longer be ignored. The effect is to give each electron state a $\underline{k}$-space spread Δk given by

$$L\,\Delta k = 2\pi \ . \qquad (3.16)$$

Equation 3.16, with $\hbar\Delta k$ regarded as momentum spread, is simply the uncertainty-principle consequence upon Δk of the electron wavefunction's confinement to length L. Thus this argument also relies on the uncertainty principle,

and will be seen to be physically equivalent to the treatment of the last section.

Figure 3.8 illustrates the effect of the wavevector spread Δk on the interband transitions. (Photon wavevector is taken be to zero in Fig. 3.8). A direct ($\underline{k}_c = \underline{k}_v$) transition in c-GaAs is indicated in Fig. 3.8-(a), in the vicinity of a critical point at which the bands are parallel. All vertical transitions near the critical point contribute optical absorption processes at a well-defined energy. The effect of wavevector spread in μ-GaAs is indicated in Fig. 3.8-(b). From Fig. 3.8-(b) it can be seen that wavevector spread results in an energy spread via energy-band dispersion dE/dk:

$$\Delta E = 2\left|\frac{dE}{dk}\right|\Delta k \ . \qquad (3.17)$$

Identifying ΔE with Γ_{size}, the size-related broadening, and substituting Δk from Eq. 3.16 into Eq. 3.17 yields

$$\Gamma = \Gamma_0 + 4\pi\left|\frac{dE}{dk}\right|\frac{1}{L} \ . \qquad (3.18)$$

Again we have arrived at a linear relation between Γ and L^{-1}, in agreement with observation (Fig. 3.7, Eq. 3.10). The equivalence of this result, obtained starting from a different perspective, to Eq. 3.14 of the last section, can be seen by associating v of Eq. 3.14 to the group velocity $\hbar^{-1}dE/dk$ corresponding to a wave packet

constructed from states near k.

Equation 3.18 allows us to connect the present results to the band structure of GaAs. The $\underline{k}$-space gradient of $E(\underline{k})$, which determines the second term in Eq. 3.18, can be estimated from the bands in those regions of the Brillouin zone which dominate the contribution to each optical feature. The question of identifying the $\underline{k}$-space regions which give rise to the E_1, $E_1+\Delta_1$, and E_2 features has long been studied [Cohen and Chelikowsky 1982, Ehrenreich et al. 1962, Greenaway 1962, Lautenschlager et al 1987], and yet appears to be incompletely resolved. We make the following consensus-type assumptions, and rely on the energy band structure of Cohen and Chelikowsky for extracting numerical estimates. We assume that the E_1 and $E_1+\Delta_1$ transitions occur along the Λ directions, including the L points, and that the E_2 transitions occur near the X and K points and along the Σ directions. (See Fig 1.1b in Chapter 1 for the Brillouin zone and the symmetry notations, and Fig. 1.2 for representative transitions.) Under these assumptions, we can estimate a range of values for $|dE/dk|$ for each transition. The minimum value is zero in each case, corresponding to the horizontal bands at the symmetry points [Phillips 1966] L (for E_1 and $E_1+\Delta_1$) and X (for E_2). The maximum gradient for E_1 and $E_1+\Delta_1$ occurs

along Λ, about halfway between Γ and L, and for E_2 it occurs near K. These maximum values are included in Table 3.3 in the form $4\pi|dE/dk|$, in order to provide a comparison to the experimental A values (equating the L^{-1} coefficients in Eqs. 3.10 and 3.18). Considering the approximations contained in the model, the rough agreement is reasonable and supports the overall picture.

A detail worthy of comment is the experimental difference found between the behaviors of the size-effect broadenings of the E_1 and the $E_1+\Delta_1$ peaks. Since this doublet arises from the spin-orbit splitting of the valence band, it is generally presumed that both peaks arise from transitions in the same region of $\underline{k}$-space (hence the equal entries in the middle column of Table 3.3). However, the difference that we observe in the finite-size effects on E_1 and $E_1+\Delta_1$ suggests that the contributing $\underline{k}$-space regions are shifted relative to each other. It is noteworthy that a recent detailed study of the effect of temperature on the interband spectra of c-GaAs finds that the $E_1+\Delta_1$ linewidth increases more slowly with increasing temperature than does the E_1 linewidth [Lautenschlager et al. 1987], a result which is in the same direction as the present finding for the effect on linewidth of finite microcrystal size.

TABLE 3.1 Amorphous fraction and crystallite size in Be^+-GaAs

Sample	fluence	f_a (opt)[a]	f_a (Raman)[b]	L(Raman)[b]
(a)	$1x10^{13}$ cm^{-2}	0.03	---	(500 Å)[c]
(b)	$5x10^{13}$ cm^{-2}	0.07	0.07	160 Å
(c)	$1x10^{14}$ cm^{-2}	0.11	0.12	82 Å
(d)	$5x10^{14}$ cm^{-2}	0.20	0.25	55 Å

[a] Estimated from the optical studies reported here.
[b] Estimated from the Raman studies of Holtz et al. [1988].
[c] Crude estimate based on Fig. 3.7. The other entries in the last column are based on Holtz et al. [1988].

TABLE 3.2 Comparison of the oscillator parameters (Eq. 3.1) fitted to c-GaAs and to the microcrystalline phase (μ-GaAs) in the $5x10^{14}$ cm^{-2} implant.[a]

Interband transition	E_1 (c) (eV)	E_1 (μ) (eV)	Γ_1 (c) (eV)	Γ_1 (μ) (eV)	F_1 (c) (eV)	F_1 (μ) (eV)
E_1	2.92	2.92	0.19	0.53	2.22	2.56
$E_1+\Delta_1$	3.12	3.16	0.34	0.50	3.16	2.82
	3.39	3.45	0.68	0.67	3.88	3.21
	3.86	3.94	0.92	0.98	4.09	3.65
	4.56	4.59	0.75	0.95	7.22	7.69
E_2	4.85	4.87	0.39	0.78	4.82	5.53
	6.1	6.3	2.5	1.9	9.3	10.2
					ε_∞=1.55	ε_∞=2.38

[a] The parameter values listed in the table have been rounded off from the actual fitting parameters; the dropped digits are not significant and contribute only noise to a discussion of these values.

TABLE 3.3 Excited-state lifetimes τ as limited by finite-size effects in μ-GaAs, as well as carrier velocities v, estimated from the observed slopes (A) of the linear relations connecting spectral linewidth Γ and reciprocal microcrystallite size L^{-1}. The quantity $4\pi(dE/dk)_{max}$, estimated from the band structure of Cohen and Chelikowsky [1982], is included for comparison to A.

Interband transition	Exptl. Slope A ($d\Gamma/dL^{-1}$ in eV Å)	$4\pi(dE/dk)_{max}$ (eV Å)	v (cm/s)	τ (for L=100 Å) (s)
E_1	18	16	2×10^{7}	2×10^{-14}
$E_1+\Delta_1$	9	16	1×10^{7}	5×10^{-14}
E_2	21	34	2×10^{7}	2×10^{-14}

Figure Captions

Fig. 3.1 Reflectivity spectra, shown as points, of 45-keV Be^+-implanted GaAs with ion fluence: (a) $1x10^{13}$, (b) $5x10^{13}$, (c) $1x10^{14}$, (d) $5x10^{14}$ ions/cm^2. The two curves included for comparison, and repeated in each panel, are the reflectivity spectra of c-GaAs and a-GaAs.

Fig. 3.2 Real part of the dielectric function of 45-keV Be^+-implanted GaAs with ion fluence: (a) $1x10^{13}$, (b) $5x10^{13}$, (c) $1x10^{14}$, (d) $5x10^{14}$ ions/cm^2. The dielectric functions are obtained from the reflectivity spectra of Fig. 3.1 using Lorentz-oscillator analysis, as described in the text. The c-GaAs and a-GaAs counterparts are included for comparison.

Fig. 3.3 Imaginary part of the dielectric functions of the implanted samples, along with the c-GaAs and a-GaAs counterparts.

Fig. 3.4 Real part of the dielectric function of the microcrystalline phase (μ-GaAs) in 45-keV

Be^+-implanted GaAs with ion fluence: (a) $1x10^{13}$, (b) $5x10^{13}$, (c) $1x10^{14}$, and (d) $5x10^{14}$ ions/cm^2. The dielectric functions of μ-GaAs are deduced from the results of Figs. 3.2 and 3.3 using the effective medium approximation, as described in the text. The c-GaAs counterpart is included in each panel for comparison.

Fig. 3.5 Imaginary part of the dielectric function of the microcrystalline phase in each of the implanted samples, as described in the caption of Fig. 3.4.

Fig. 3.6 Absorption coefficient of the microcrystalline phase in each of the implanted samples, as described in the caption of Fig. 3.4. The absorption coefficients are directly calculated from the dielectric functions of Figs. 3.4 and 3.5.

Fig. 3.7 Spectral linewidth as a function of the reciprocal of the characteristic microcrystallite size for the three prominent interband features in the μ-GaAs spectra of Figs. 3.4-3.6. The straight lines are fits to the data.

Fig. 3.8 Direct interband electronic transitions, in the vicinity of a critical point, in a bulk crystal, (a), and in a microcrystallite, (b). The $\underline{k}$-vector broadening due to the finite crystallite size in (b) results in the broadening of the transition energy.

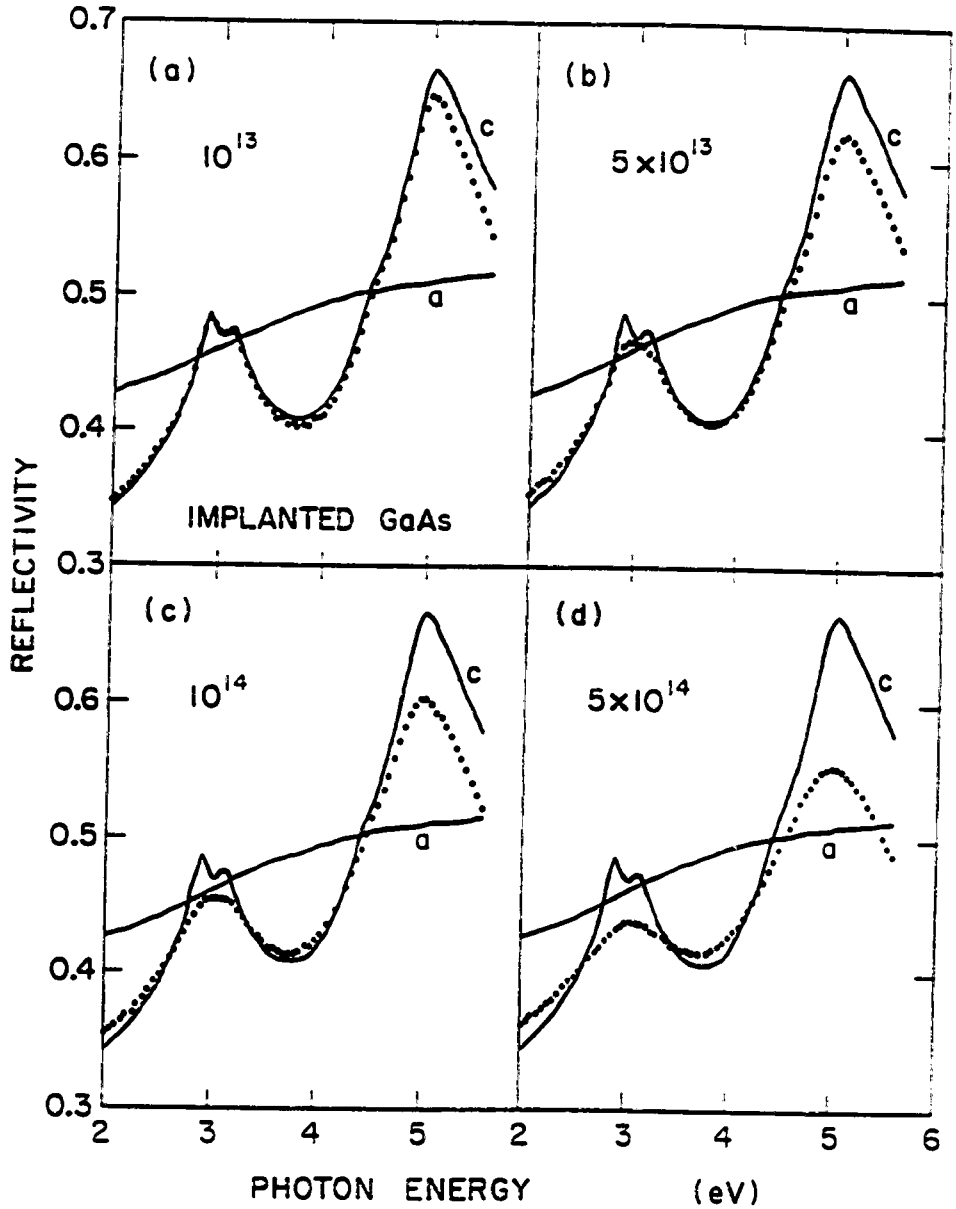

Fig. 3.1 Reflectivity spectra of the Be^+-implanted GaAs

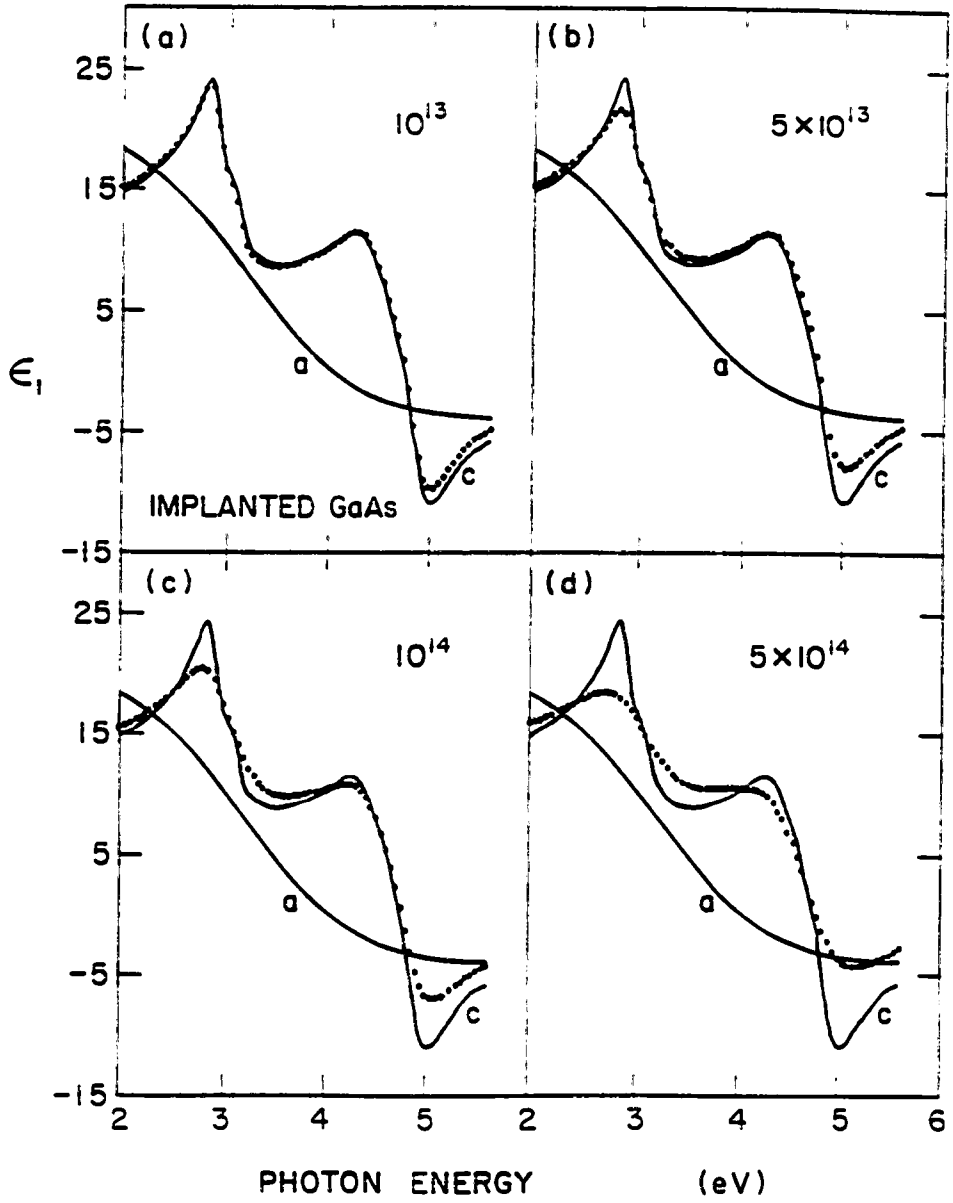

Fig. 3.2 ε_1 of the Be^+-implanted GaAs

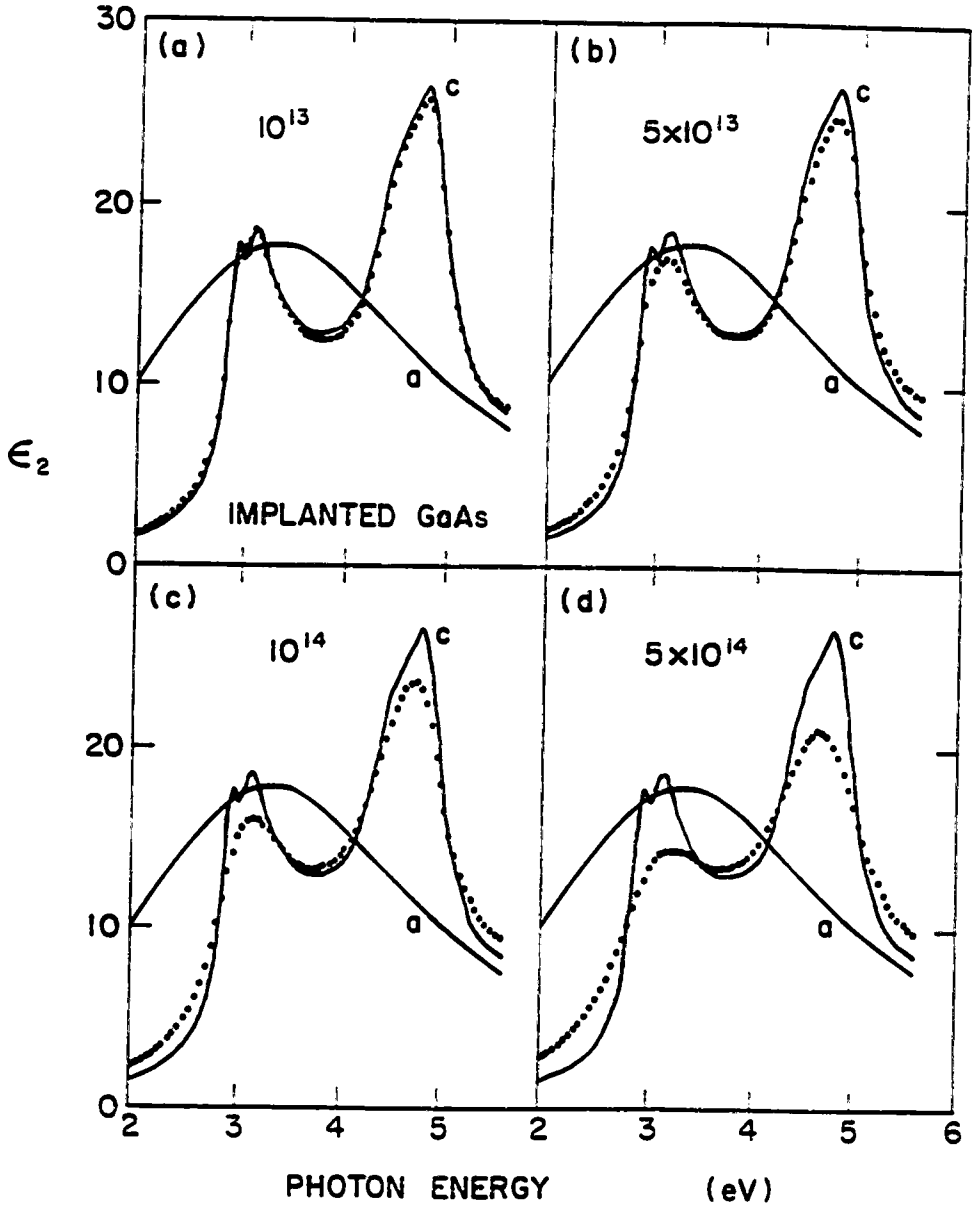

Fig. 3.3 ϵ_2 of the Be^+-implanted GaAs

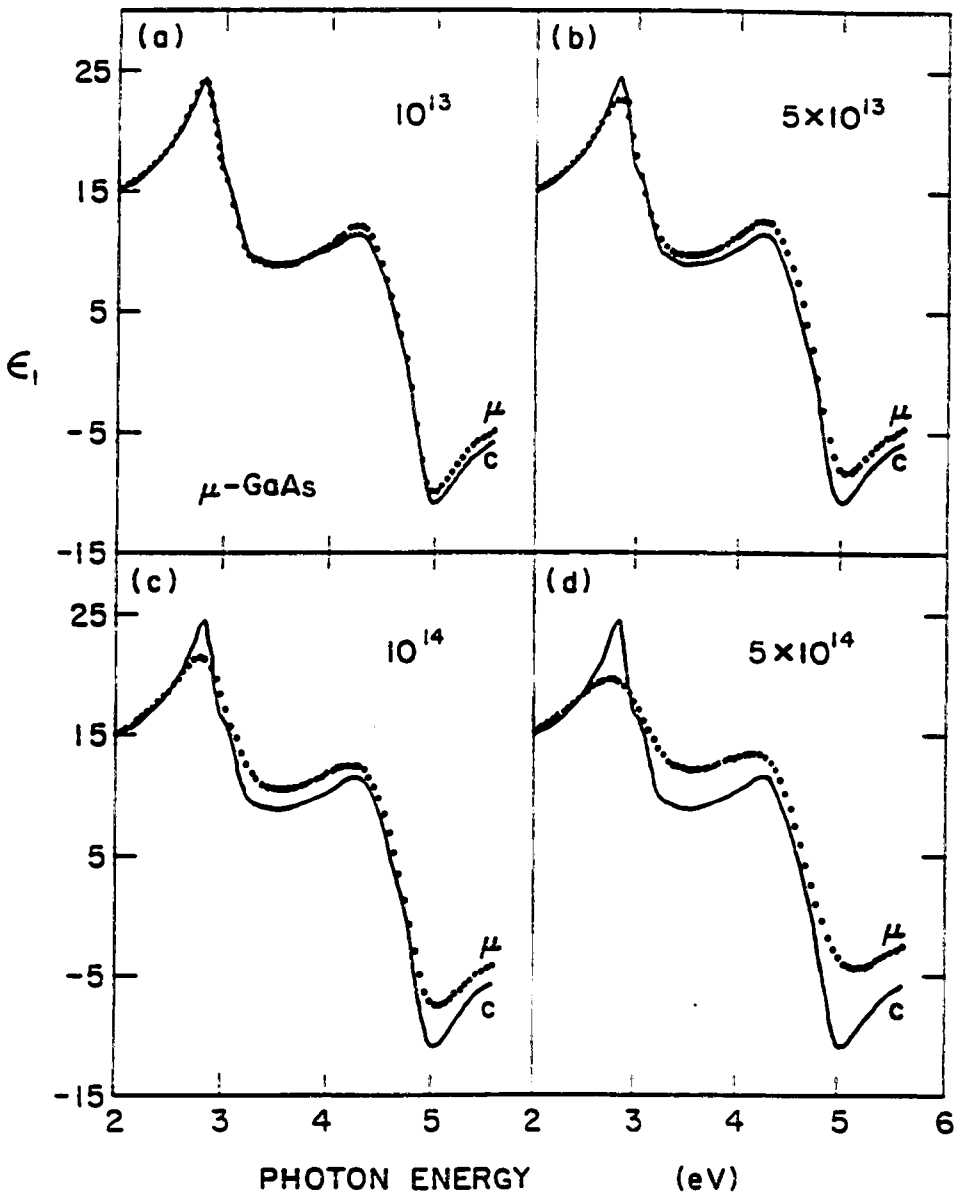

Fig. 3.4 ϵ_1 of the μ-GaAs in Be^+-GaAs

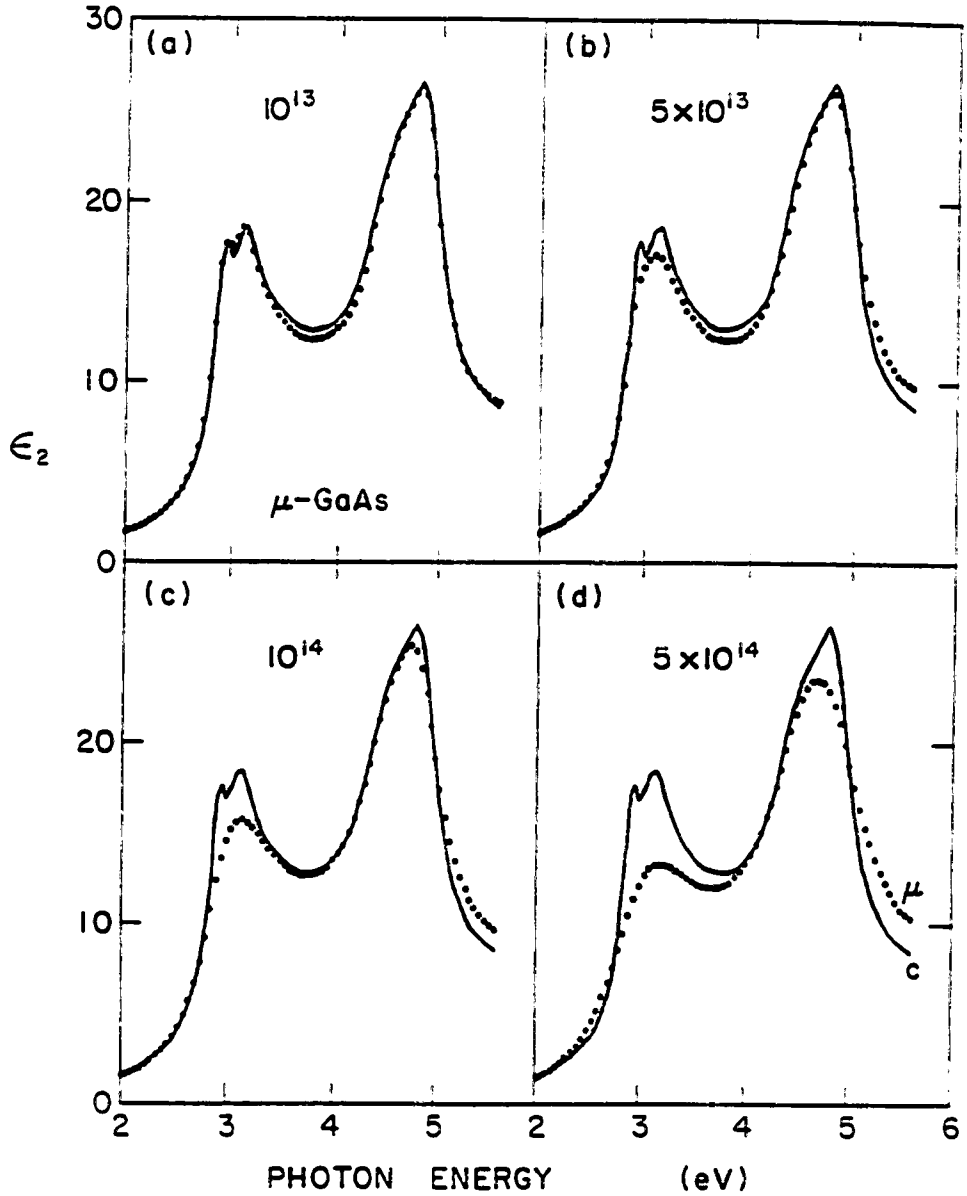

Fig. 3.5 ϵ_2 of the μ-GaAs in Be^+-GaAs

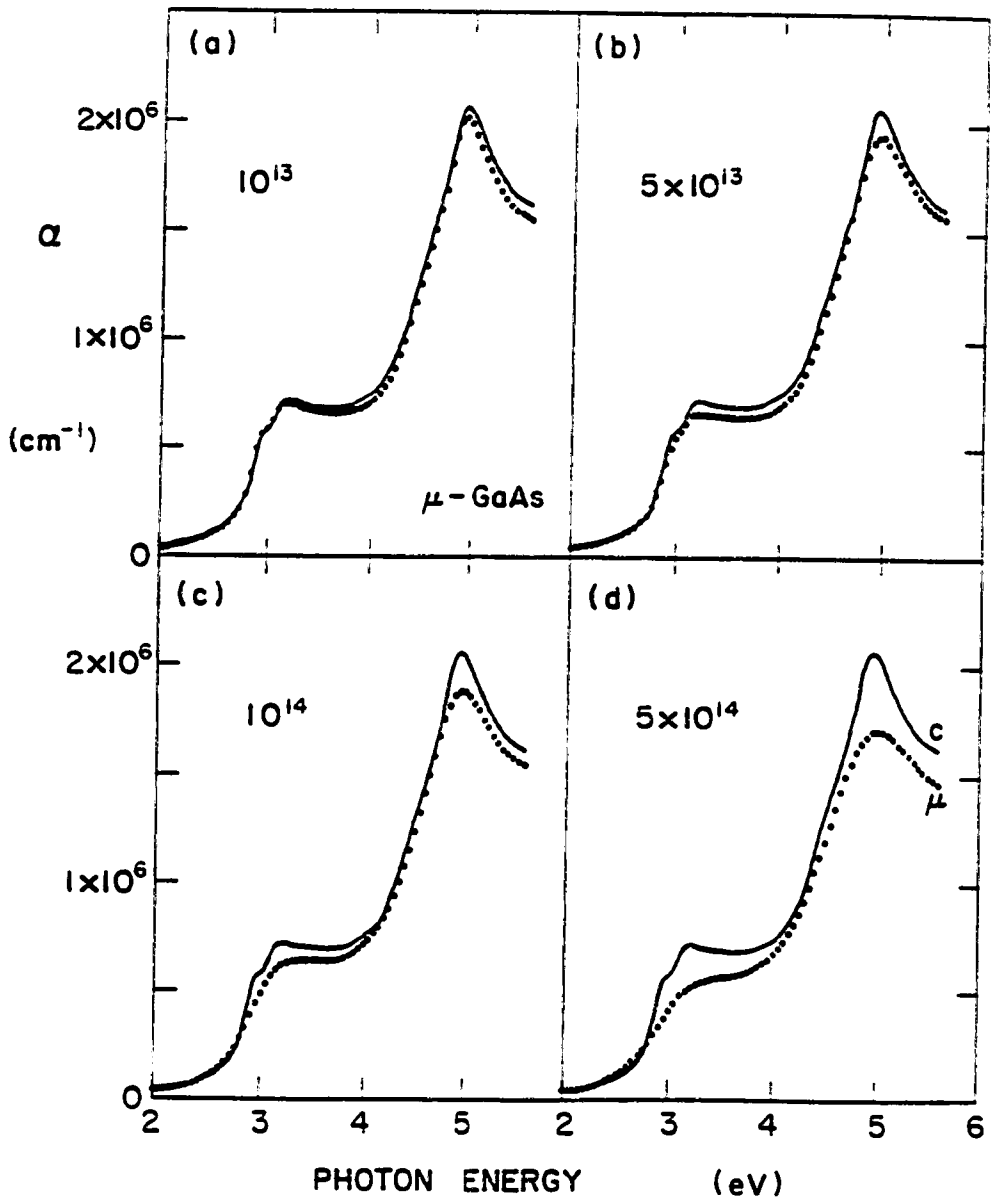

Fig. 3.6 Absorption coefficient of the μ-GaAs in Be^+-GaAs

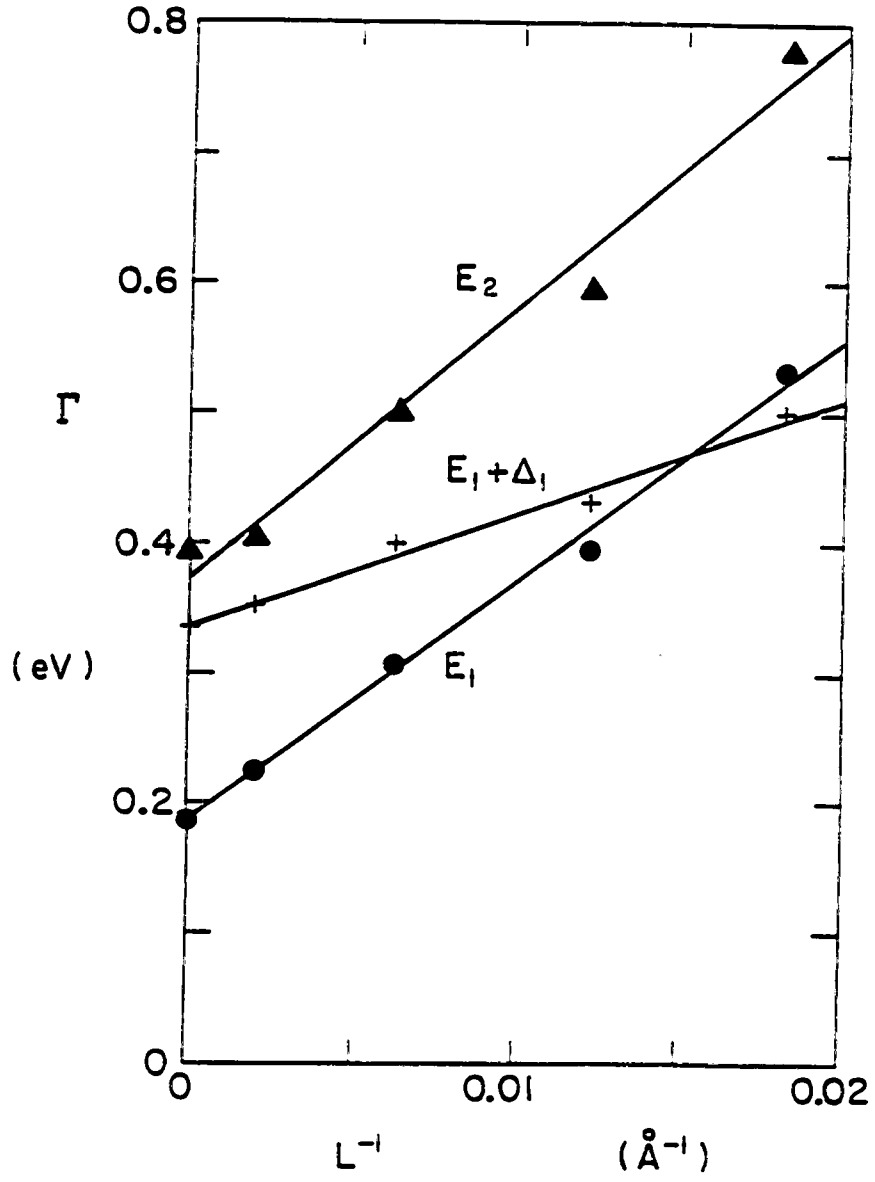

Fig. 3.7 Spectral linewidth vs. L^{-1}

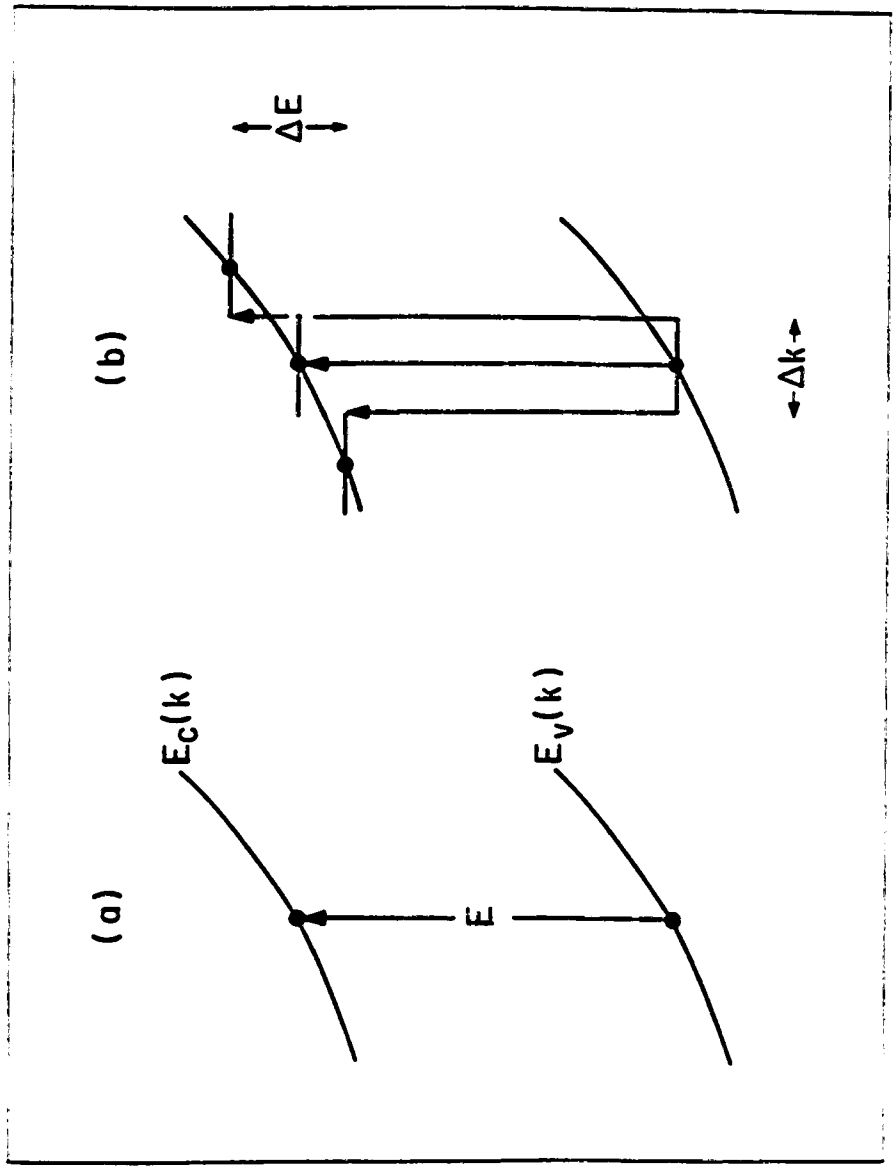

Fig. 3.8 Directe interband electronic transitions
(a) in c-GaAs and (b) in μ-GaAs

CHAPTER 4

CHARACTERIZATION OF ION-ETCHED GaAs SURFACES

4.1 Background on Ion-etched GaAs

Ion etching is a physical process in which substrate surface atoms are removed (sputtered) via momentum transfer from incident energetic particles. Substrate lattice structural damage is expected due to the collisions between the incident energetic particles and the surface atoms, and the subsequent cascades. This chapter describes a study of the damage distribution and its nature in Ar^+-ion bombarded GaAs.

Ion-etching-induced damage in semiconductors has been studied with various techniques such as electrical (I-V, C-V) characterization [Pang 1984, 1986; Cole 1988], secondary-ion mass spectrometry [Mu et al. 1985, Clegg 1987], spectroscopic ellipsometry [Mu et al. 1985], and Raman spectroscopy [Wagner and Hoffman 1987]. However, few detailed studies of the damage profile, or of the nature of the damage, have been reported. Some of the fundamental questions have not been clearly answered. These include whether an amorphous layer is formed near the surface, what the depth distribution of the damage is, and what the

nature of the damage is. In this chapter, the damage distribution in Ar^+-etched GaAs is studied by means of the Raman-scattering technique and visible-near-ultraviolet reflectivity measurements, together with wet chemical etching. A graded damage profile model is proposed, which well explains the damage distribution probed by the Raman and reflectivity measurements. Finally, the nature of the ion-etch induced damage is tentatively interpreted on the basis of the observations in the Raman and reflectivity experiments.

4.2 Argon-Etched Samples and Experimental Methods

The virgin gallium arsenide samples were silicon-doped, liquid-encapsulated-Czochralski (LEC) grown, (100)-oriented, single crystal wafers. The wafers were obtained from Morgan Semiconductor Division of Ethyl Corporation. The samples were n-type with carrier concentration in the range $(2 - 7) \times 10^{16}$ cm^{-3}. The surfaces were of good optical quality, and near-ultraviolet reflectivity exhibited the sharp spectral features characteristic of crystalline GaAs. Prior to ion-beam exposure, the wafers were cleaned in a 1:1 HCl solution to remove surface contaminants, and then rinsed in deionized water.

Ar^+-ion bombardment was carried out in a Perkin Elmer PHI 5300 XPS system housed in the Chemistry Department at

Virginia Tech [Epp and Dillard 1989]. The incident ion energy was varied between 0.5 keV and 4 keV; the ion fluence was fixed at 10^{17} ions/cm^2 for all ion-etched samples. The angle of incidence of the ion beam was about 45° from the surface normal, in a non-channeling direction not far from a [111] axis. The bombardment parameters are listed in Table 4.1. Bombardment was performed at room temperature. The beam was raster-scanned over an area of 10×10 mm^2. The base pressure in the chamber was about 2×10^{-8} torr, and it rose to 10^{-7} torr during ion-bombardment. Because of the low ion currents used in these experiments (see Table 4.1), the sample temperature rise during ion bombardment was negligible. After the ion bombardment, samples were exposed to the atmosphere for the spectroscopic measurements.

In order to depth-profile the surface damage, the ion-bombarded samples were chemically etched using a weak acidic solution of 1:1:100 H_2SO_4:30%H_2O_2:H_2O [McLevige 1978, Holtz et al. 1988]. The etch rate had been studied previously, yielding a rate of about 530 Å/minute for c-GaAs and slightly higher for ion-implantation-damaged GaAs [Holtz et al. 1988]. The etch rate is assumed to be 100 Å/10-sec in this study for both the near-surface damage layer and the unperturbed substrate beyond the damage layer. The minimum etch time was 10 seconds,

corresponding to the removal of a layer of 100 Å. Due to the approximate etch rate and the short etch time, a relatively large etch-depth uncertainty is expected; the error is estimated to be about 20% of the etched depth.

Room-temperature Raman scattering measurements were carried out using the double-monochromator spectrometer (SPEX 1403) which has been described in Chapter 2. The near-backscattering geometry was used. The incident beam was polarized perpendicularly to the incident plane, while the scattered light was not polarization-analyzed. According to the selection rules of the GaAs zincblende structure discussed in Chapter 1, the transverse-optical (TO) Raman modes are suppressed in this scattering geometry. The longitudinal-optical (LO) mode thus dominates the first-order Raman spectrum. Normalized Raman-intensity measurements were made using a replacement technique [Holtz et al. 1988] with either c-GaAs or CaF_2 as reference standard. The area under the LO peak was taken as its integrated peak intensity in this analysis, unless otherwise noted.

Optical reflectivity spectra in the visible and near-ultraviolet region (vis-near-UV, photon energy E ranging from 1.6 to 5.6 eV) were taken at room temperature. The dielectric function and other optical functions were derived from the observed reflectivity

spectrum using the Lorentz-oscillator analysis and the fitting technique described in Chapters 1 and 2.

4.3 Raman Scattering of Argon-Etched GaAs

The Stokes Raman spectra of the series of Ar^+-bombarded GaAs samples are shown in Fig. 4.1. Raman intensities are normalized to the same reference standard, so that changes in peak heights are significant. The spectra were taken with the 4579-Å (2.71-eV) line of the argon-ion laser. The laser beam probing depth at this photon energy, $1/(2\alpha)$, where α is the absorption coefficient, is about 250 Å for c-GaAs [Aspnes and Studna 1983], about 100 Å for a-GaAs [Aspnes 1988], and in between for the damaged samples. The optical penetration depth at 2.71 eV was also deduced from our own reflectivity measurements (and subsequent oscillator analysis) on c-GaAs and a-GaAs samples, with results in good agreement with the above values.

The sharp first-order Raman peak at 292 cm^{-1} corresponds to the LO phonon of c-GaAs, and the structures seen between 500 cm^{-1} and 580 cm^{-1} correspond to second-order (two-phonon) Raman processes in c-GaAs. Figure 4.1 clearly exhibits the spectral evolution with respect to the incident ion energy. The decrease of the first-order LO peak intensity, as well as of the second

order features, indicates the degradation of the near-surface crystalline quality in the bombarded samples.

A comparison of the first-order LO peak (1LO) with the second-order features shows that the second-order Raman bands are as sensitive as the 1LO line is to the crystalline quality; the ratio of the 1LO peak area to the area of the second-order features (the area above the smooth background which extends to high frequencies) remains the same for all of the five samples in Fig. 4.1. With 2.71-eV laser excitation, we do not see a stronger dependence of the second-order LO-phonon (2LO) band (near 580 cm^{-1}) than the 1LO line on the near-surface crystalline quality.

Wagner and Hoffman [1987] studied low-energy ion-bombarded GaAs with resonance-Raman scattering. Probing with a 3.0-eV laser line, they found that 2LO band to be more sensitive to damage than the 1LO line, in contrast to the behavior observed here in Fig. 4.1. Strong resonance-Raman effects were seen in their spectra, in which the 2LO band completely dominated the two-phonon region. Strong resonance Raman scattering is known to occur in GaAs when the probing photon energy is close to the E_1 electronic interband-transition energy of 2.9 eV [Trommer and Cardona 1978, Grimsditch et al. 1979]. Although the photon energy (2.71 eV) of the laser line

used in the present investigation is close enough to E_1 to produce discernible resonance enhancement of the 1LO line [Grimsditch et al. 1979, Berg and Yu 1987, Holtz et al. 1988], the 2LO band dose not dominate the two-phonon region in Fig. 4.1 to nearly the extent that it dominates the spectra of Wagner and Hoffman. This likely accounts for the discrepancy between their results and those of Fig. 4.1 with respect to the relative sensitivity of the 2LO band. The enhanced damage-sensitivity of the 2LO band evidently depends on being very close to resonance.

The region near the LO peak of Fig. 4.1 is expanded and shown in Fig. 4.2, again in intensity units normalized to a reference standard. A systematic intensity decrease is clearly seen with increasing Ar^+-ion energy. For the sample bombarded with ions of highest ion energy, 3.89 keV, the LO Raman intensity is only about 1/3 of that of c-GaAs. Also evident in Fig. 4.2 is that, despite the significant decrease in the LO peak intensity, the peak lineshape remains essentially unchanged from that of c-GaAs. This is a significant difference between ion-etched GaAs and ion-implanted GaAs. In the latter, a pronounced LO peak position shift and an asymmetric lineshape broadening occur in addition to the intensity decrease [Richter et al. 1981, Holtz et al. 1988] This difference is important and will be discussed further in

Sec. 4.4.

4.4 Interband Reflectivity of Argon-Etched GaAs

Figure 4.3 displays the vis-near-UV reflectivity spectra R(E) of the ion-etched series, where E denotes the photon energy. Also shown, as curves repeated in each panel to provide the visual banchmarks, are the spectra of c-GaAs and a-GaAs. The c-GaAs spectrum is derived from the ellipsometry work of Aspnes and Studna [1983], while the a-GaAs spectrum is derived from ellipsometry studies of implantation-amorphized GaAs [Aspnes et al. 1982, Aspnes 1988]. Indicated in each panel is the Ar^+-ion kinetic energy used in the ion bombardment. The reflectivity spectrum in this photon-energy region reflects direct ($\underline{k}$-vector conserved) interband electronic transitions. As discussed in Chapters 1 and 3, the three well-defined peaks of the spectrum of c-GaAs are conventionally denoted as E_1 (at 2.9 eV), $E_1+\Delta_1$ (at 3.1 eV, the spin-orbit-split partner of E_1), and E_2 (at 5.0 eV). The $E_1/E_1+\Delta_1$ doublet is attributed to direct interband transitions along the Λ directions and near the L symmetry points of the Brillouin zone; the E_2 peak is associated with transitions at the plateau along the Σ directions and near the X points [Chelikowsky and Cohen 1976]. Direct transitions representative of E_1, $E_1+\Delta_1$, and E_2 were illustrated in

Fig. 1.2 by the vertical lines labelled a, b, and c, respectively.

Appreciable effects of ion bombardment on the interband spectrum can be seen even for the sample with lowest ion energy, 0.5 keV. As the ion energy increases, the E_2 peak height decreases substantially, while the $E_1/E_1+\Delta_1$ doublet peak height changes little. All of the peaks broaden, and the spectrum evolves from the crystal spectrum towards the amorphous one, as ion energy increases.

Figure 4.3 exhibits another important feature. Along with the broadenings of the E_1, $E_1+\Delta_1$, and E_2 peaks, the positions of all of the peaks shift to lower photon energies. For panel (d) of Fig. 4.3, corresponding to the ion-bombardment energy of 3.89 keV, the peak positions have red-shifted by about 0.2 eV with respect to the crystal peaks. Such a bombardment-induced red shift of the interband reflectivity peaks is not observed in Be^+-implanted GaAs after bombardment by high-energy (45-keV) Be^+ ions (see Fig. 3.1 in Chapter 3). In that case the dominant effect is peak broadening; peak positions are unaffected. Such a red shift is also not observed in high-energy implantation of GaAs with heavier ions such as Si^+ and SiF_3^+. Figure 4.4 exhibits the reflectivity spectra of a sample of Si^+-implanted GaAs which had been

subjected to an ion dose of 2×10^{13} cm^{-2} and an implantation energy of 120 keV. For this spectrum, as for the Be^{+}-GaAs spectra shown in Fig. 3.1, the peaks are essentially unshifted.

These red shifts, present in ion-etched GaAs while absent in ion-implanted GaAs, indicate that the nature of the damage in the ion-etched system is different from that of the ion-implanted system discussed in Chapter 3. The interpretation of the peak shifts will be discussed in Sec. 4.5.

Lorentz-oscillator analysis of the reflectivity spectra in Fig. 4.3 was carried out to deduce the dielectric functions, and then other optical properties, of the ion-etched samples. Figures 4.5 and 4.6 show the real and imaginary parts of the dielectric functions of these samples. The oscillator parameters for sample d, with ion-energy of 3.89 keV, are given in Table 4.2, together with the parameters for the starting crystal. The oscillator positions, $E_1=\hbar\omega_1$, of the E_1, $E_1+\Delta_1$, and E_2 peaks for sample d clearly exhibit the red shift observed in the reflectivity spectrum. It should be noted that the near-surface structure of each bombarded sample is not uniform but is depth-dependent, as will be seen in the next section. The dielectric functions shown in Figs. 4.5 and 4.6 should thus be understood as pseudodielectric

functions [Aspnes 1982], and so should the properties derived therefrom.

4.5 Depth Profile of the Damage in Ion-Etched GaAs

Momentum transfer from the incident ions to the target crystal during ion bombardment causes structural damage in the target. The low ion energy used in ion etching confines the damage to within a few hundred angstroms of the surface, even taking into account damage diffusion [Pang 1984, 1986]. This section contains a detailed study of the damage profile in the bombarded samples by the use of Raman-scattering and reflectivity measurements done in combination with wet chemical etching.

The ion-etched samples were chemically etched (as described in Sec. 4.2) to depths up to 600 Å, at which depth the unperturbed crystal substrate was recovered. By gradually removing material (to a known depth) from the surface, a set of samples were obtained for each bombardment energy, yielding four sets of samples (corresponding to the four bombardment energies). LO Raman peak-intensity measurements were then carried out on these chemically etched samples. Measurements were made with the 5145-Å argon-laser line (2.41 eV), corresponding to an optical penetration depth of 540 Å for c-GaAs, 120 Å for

a-GaAs, and in between for the disordered medium. The LO intensity was normallized, by means of a kinematic-mount replacement technique [Holtz 1987], using the c-GaAs as a reference standard. The data points (symbols) in Fig. 4.7 show the LO intensity versus chemical-etch depth for the four Ar^+-bombardment samples. Both ion-energy dependence and depth dependence of the LO intensity are clearly demonstrated in this figure. The higher the ion energy, the smaller the LO intensity; and as the surface is removed in 100-Å steps, the LO intensity approaches the value characteristic of c-GaAs until that value is recovered. For the highest bombardment energy, the undisturbed crystal is reached at an etch depth of about 500 Å.

We write the relative Raman intensity from a medium with a depth dependent structure as

$$I = \frac{(1-R)^2}{(1-R_c)^2} \frac{2\alpha_c n_c^2}{|e_i \cdot \vec{R}_c \cdot e_s|^2} \int_0^\infty \frac{1}{[n(z)]^2} g(z) |e_i \cdot \vec{R} \cdot e_s|^2 dz \quad . \quad (4.1)$$

Here R, n, and α are the optical reflectance, refractive index, and absorption coefficient of the medium, and, with sunscript c, of the crystal, respectively. In Eq. 4.1 the optical properties of the incident and the (slightly-downshifted) scattered light are taken to be the same. The light-attenuation factor g(z) will be discussed in p. 116.

The factor $|e_i \cdot \vec{R} \cdot e_s|^2$ in Eq. 4.1 describes the Raman

efficiency of the scattering medium with the polarization of the incident light as e_i and that of the scattered light as e_s. For c-GaAs with the polarization described in Sec 4.1, this factor is simply d^2, where d is the nonvanishing matrix element of the Raman tensor of the Γ_{15} LO phonon (see Table 1.1 in Chapter 1). For the disordered medium, the Raman efficiency depends upon the nature of the disorder.

The spectra in Figs. 4.1 and 4.2 have shown that the LO Raman peak in the ion-etched samples has little change in shape; the full width at half maximum (FWHM) remains essentially the same for all four samples. The intensity drop dominates the bombardment-induced spectral change. This indicates that the near-surface damage layer probed by the Raman measurements is not essentially different from c-GaAs. The lattice modes of c-GaAs are preserved in this "nearly-crystalline" phase. The drop in the LO intensity is likely due to the atoms that are removed from crystalline sites to defects, or that are sputtered out of the sample -- leaving vacancies behind. In a region with a high density of defects, the medium may become "locally amorphous". As a very crude model, we describe the high density of defects by an amorphous phase which is dispersed throughout the continuous nearly-crystalline damage layer. The volume fraction of the amorphous phase, denoted as f, is a depth-dependent parameter. With such a

drastic assumption, the disordered near-surface medium of the ion-etched sample can then be treated as a two-phase mixture: a crystalline phase which preserves the lattice-vibrational properties of the unperturbed bulk crystal, and an "amorphous phase" which we introduce to describe the collective effects of the defects and the amorphous regions.

The slight rise of the left shoulder of the LO peak in Fig. 4.2 is the result of scattering from the amorphous phase. The amorphous spectrum provides only a smooth background in the vicinity of the LO peak, and it dose not contribute to the peak area of the LO mode, which is taken as its intensity. With the assumed structural model, the Raman efficiency of the disordered layer can then be expressed as

$$|e_i \cdot \vec{R} \cdot e_s| = (1-f)\, d^2 \quad , \tag{4.2}$$

where f is the volume fraction of the amorphous phase. Since the 2.41-eV laser line used for the Raman measurements of Fig. 4.7, is well away from the E_1 interband transition energy at 2.9 eV, resonance-Raman effects do not enter here [Trommer and Cardona 1978, Holtz et al. 1988]. On the other hand, the optical penetration depth at 2.41 eV is relatively short, which allows the Raman signal to be a sensitive probe of the near-surface

structure.

The light-attenuation factor g(z) in Eq. 4.1 is mainly due to the optical absorption of the incident and the scattered light, because the light loss due to Raman-scattering processes is orders of magnitude weaker [Cardona 1982]. We then have

$$g(z) = \exp[-2\int_0^z \alpha(z')dz'] \quad . \tag{4.3}$$

In this spectral region, the optical absorption α in the integral of Eq. 4.3 can be approximately by [Holtz et al. 1988],

$$\alpha = (1-f)\ \alpha_c + f\ \alpha_a \quad , \tag{4.4}$$

where α_c and α_a are the absorption coefficients of crystal and amorphous GaAs. Again, since the 2.41-eV line is well below the first strong critical-point feature at 2.9 eV (which is affected by the disorder, as seen in Fig. 4.3), it is not unreasonable to use the bulk-crystal value for α_c in Eq. 4.4.

The combination of Eqs. 4.1 through 4.4 yields the dependence of the Raman intensity I(f(z)) on the final depth-dependent damage profile f(z) which characterizes the damage layer. If damage is measured by the number of lattice atoms knocked away from their lattice sites by

collisions suffered during bombardment, then a near-Gaussian damage distribution is expected [Lindhard et al. 1963, also see Secs. 3, 4, and 8 in Bromley 1985]. Although such a distribution has not been observed in low-energy ion-etched GaAs, a near-Gaussian incident-ion distribution has been reported for low-energy low-fluence As^+-bombarded Si [Clegg 1987], and Ar^+-bombarded Cu [English and Jenkins 1985]. We now assume that individual Ar^+ ions produce a Gaussian damage distribution in the near-surface region of the GaAs sample studied here. In addition, an attempt is made to take into account the receding sample surface (etching) caused by the sputtering of surface atoms during the ion bombardment, since a high fluence was used in these experiments. With these considerations, we write the damage profile of the ion etched samples as

$$f(z) = \text{const} \cdot \int_0^T \exp\left[-\frac{(x-rt-R_p)^2}{2\sigma_p^2}\right] dt \ , \qquad (4.5)$$

where r is the sputtering rate, T is the total sputtering time, and $rT = d_{sput}$ is the total depth of the material sputtered (or ion-etched) away. R_p and σ_p are two parameters characterizing the assumed Gaussian and are conventionally denoted as the range and standard deviation, respectively. The depth variables x and z are

measured from the two surface frontiers before and after the bombardment, and are related by

$$x = z + d_{sput} \quad . \tag{4.6}$$

At time t, the actual surface is at (x-rt) and the most damage occurs at distance R_p from that surface, as expressed in the argument of the Gaussian of Eq. 4.5. The total sputtered depth d_{sput} is given by $d_{sput} = rT = SF \cdot a^3/8$, where S is the sputtering yield, F is the ion fluence (1×10^{17} cm^{-2} for these samples), and a is the lattice constant of GaAs. For ion energy of a few keV, S varies slowly as a function of ion energy [Kawable et al. 1978, Poate 1985], and is about 1 atom/ion for normal incidence in Ar^+-sputtered GaAs [Kawable et al. 1978]. For 45° incidence, the yield is expected to be higher by a factor of about $(\cos 45°)^{-1.5}$ [Johnson et al. 1987]. d_{sput} is thus calculated to be about 400 Å. Measurements on the 3.89-keV bombarded sample yielded a value for d_{sput} of 500 Å [Epp 1988], in good agreement with the above estimate. For simplicity, a fixed d_{sput} of 500 Å is assumed for all four samples (i.e., S was assumed energy-independent). The fitting to the Raman intensity data showed that a variation of 20% in d_{sput} resulted in little change in the fits and the damage profiles. This is mainly because the high ion fluence used in this study has

nearly saturated the surface damage. The tendency toward the surface-damage saturation was observed in our Raman and reflectivity measurements on a series of Ar^+-etched samples with the fluence up to 10^{18} cm^{-2}.

To reduce further the number of free parameters in this model, the projected range R_p was estimated from the literature. Extrapolation of the projected range data of Wilson and Brewer [1979] on argon-bombarded GaAs yielded these estimates of R_p: about 35 Å, 40 Å, 45 Å, and 55 Å, for samples a, b, c, and d, respectively. Again, the fits were found to be insensitive to 20% variations in R_p.

The solid curves in Fig. 4.7 are the fits to the measured Raman intensity data (points in Fig. 4.7) obtained by using Eqs. 4.1-4.5. Two parameters were adjusted in each fit: the scaling constant corresponding to the maximal damage fraction, and the Gaussian standard deviation σ_p. Their values are given in Table 4.3. The fits shown in Fig. 4.7 are quite reasonable. The corresponding damage profiles f(z) for the four samples are shown in Fig. 4.8. The curves demonstrate a smooth, graded, damage profile throughout the damage layer.

Figure 4.8 also includes a linearly graded damage profile for the four samples. These linear profiles are fits of Eq. 4.1 to the Raman intensity data of Fig. 4.7 using a simple linear damage profile. These fits are found

to be as good as those obtained with the graded profiles derived from the sputtering-Gaussian model of Eq. 4.5. Thus the experiments reported here cannot distinguish between the two sets of curves in Fig. 4.8. (The primary experimental limitation is the difficulty in obtaining a fine grid of chemical-etch depths.) Nevertheless, the solid smooth curves shown in Fig. 4.8 provide the more physically reasonable depth-profile results.

The vis-near-UV reflectivity measurements on the chemically etched samples, shown in Fig. 4.9 for sample d, qualitatively support graded damage profile of the type shown in Fig. 4.8. As the chemical etch proceeds, the reflectivity gradually returns to the crystal spectrum.

4.6 Interpretation of the Damage

It was pointed out earlier that substantial differences exist between low-energy ion-etched GaAs and high-energy ion-implanted GaAs. Plotted in Fig. 4.10 and 4.11 are spectroscopic comparisons of Ar^+-etched GaAs and the Be^+-implanted GaAs which address this point.

Figure 4.10 shows Raman spectra in the LO-mode region for sample d of the ion-etched series and for a sample of ion-implanted GaAs which had been bombarded with 45-keV Be^+ ions to a fluence of 10^{14} cm^{-2} (see also Holtz et al. [1988]). Each panel includes a comparison to the c-GaAs

spectrum of the starting material prior to bombardment (Si-doped GaAs for Ar^+:GaAs and Cr-doped semi-insulating GaAs for Be^+-GaAs; the two c-GaAs spectra are experimentally indistinguishable). The spectra were taken with the 5145-Å (2.41-eV) argon-laser line, so that resonance effects are minimal. Although the LO peak heights are different in the Ar^+:GaAs and Be^+-GaAs spectra, the integrated intensities (areas under the peaks) are nearly the same, so that a detailed comparison is appropriate.

Raman-scattering studies of Holtz et al. [1988] as well as the results of Chapter 3 have shown that the near-surface structure of the Be^+-GaAs sample consists of a fine-scale mixture of amorphous GaAs and GaAs microcrystals. The peak-position downshift and the asymmetric broadening, clearly seen in the lower panel of Fig. 4.10, manifest the finite-size effects on the vibrational excitations in the microcrystals present in Be^+-GaAs. In contrast to this, the peak position in Ar^+:GaAs (upper panel of Fig. 4.10) is scarcely shifted from the crystal peak position, and the lineshape is also very close to that of c-GaAs. More precisely, the peak shift in Ar^+:GaAs is less than 0.5 cm^{-1}, compared with 2.0 cm^{-1} in Be^+-GaAs; and no peak broadening (increase in FWHM) is seen in Ar^+:GaAs, while it is 3.0 cm^{-1} in

Be^+-GaAs. The absence of both a shift and a broadening in Ar^+:GaAs spectrum indicates that a microcrystal model cannot be applied to the crystalline phase in the ion-etched GaAs. The fact that the only bombardment-induced effect in the spectrum of Ar^+:GaAs is the decrease in peak height suggests that the crystalline phase in the disordered near-surface layer preserves the vibrational properties of the bulk crystal.

Figure 4.11 compares the interband reflectivity spectra of Ar^+:GaAs and Be^+-GaAs, again including the c-GaAs spectrum as a reference. Substantial differences can be seen between the spectra of ion-etched and ion-implanted GaAs. For Be^+-GaAs, the height of the $E_1/E_1+\Delta_1$ doublet decreases about as much as that of the E_2 peak. This implies that a uniform disordered layer is probed throughout this photon energy region, although the optical penetration depth $1/2\alpha$ is more than twice as deep for the $E_1/E_1+\Delta_1$ doublet (70 Å) as for the E_2 peak (30 Å) in Be^+-GaAs (see Fig. 3.6 in Chapter 3). This argument thus suggests that the damage layer in Be^+-GaAs is uniform to depths in excess of 70 Å, which is in fact the case (uniform high damage extends to about 1500 Å in this implanted material, as shown by Holtz et al. [1988]). For Ar^+:GaAs a similar, or slightly larger, penetration-depth ratio is expected between the $E_1/E_1+\Delta_1$ and the E_2

peaks. But in this case we see a greater decrease in peak height for E_2 than the $E_1/E_1+\Delta_1$, suggesting that more structural damage is present closer to the surface (i.e., a higher mean level of damage in the first 30 Å than in the first 70 Å). This is consistent with the damage profiles of Fig. 4.8.

A more dramatic feature of the Ar^+:GaAs reflectivity spectrum of Fig. 4.11 is the clear red-shift seen for both the $E_1/E_1+\Delta_1$ and the E_2 peaks (also seen clearly in the ε_2 spectra of Fig. 4.6). In Be^+-GaAs, on the other hand, such red-shifts are absent, and the only spectral change is the peak broadening accounted for (Chapter 3) by the lifetime decrease of the electronic excitations in the microcrystals which make up the crystalline phase within the implanted damage layer.

Low-energy ions incident in a non-channeling direction into a crystal produce defects in relatively localized areas. Although the ion fluence is very high in this study, 1×10^{17} cm^{-2}, the density of these disordered areas may not be so high as to form a continuous amorphous layer in the final near-surface damage layer. This may be due to the effect of the continuous sputtering during bombardment (which resulted in removal from the surface of a layer about 500 Å thick!). This is indicated by the damage profiles of Fig. 4.8. The absence of isolated or

separated microcrystals, as is evidenced in the Raman spectra of Figs. 4.1, 4.2, and 4.10, further suggests that there may be few interconnections among these localized disordered regions. In this picture, the crystalline phase would thus still preserve, to a large degree, the long-range order of the bulk crystal.

Energy shifts in interband reflectivity peaks have been observed in semiconductors under high pressure. Pressure blue-shifts the E_1, $E_1+\Delta_1$, and E_2 peaks in the tetrahedrally bonded semiconductor family to which GaAs belongs [Zallen and Paul 1967, Martinez 1980]. If we assume that the red-shift observed in the reflectivity spectrum of Ar^+:GaAs (Figs. 4.3, 4.6, and 4.11) is due to an equivalent negative pressure in the crystal phase arising from the high density of defects, then we may roughly estimate that equivalent pressure from the observed red-shifts and the known pressure coefficients. For Sample (d), the most damaged sample with 3.89-eV etchant, the average pressure in the surface layer turns out to be about -30 kbar. Such a high negative pressure is implausible, because it would also result in a substantial shift (10-20 cm^{-1}) of the LO Raman peak position, which is not observed (Figs. 4.2 and 4.10). So the simple idea of an equivalent negative pressure evidently does not work.

The spectral changes exhibited in Figs. 4.3, 4.6, and

4.11, both the peak broadenings and the peak shifts, can resemble effects associated with increasing temperature. The three spectra plotted in Fig. 2.5 of Chapter 2 clearly illustrate the influence of temperature on the interband spectrum: the peak broaden and red-shift with increasing temperature. Such red-shifts have been investigated both experimentally and theoretically for decades [Cohen and Chadi 1980]. The temperature dependence is believed to arise from two separate contributions: the volume change and the electron-phonon scattering.

The similarities noted in the previous paragragh suggest that the ion-etch damage may be viewed in terms of an equivalent temperature. In such an equilavency, the temperature-induced volume change, one of the two temperature contributions, is irrelevent, because its effect is the same as that of the pressure effect discussed above. The electron-defect scattering in the damaged medium may play a role similar to that of the electron-phonon scattering in the temperature effects. To estimate an equivalent temperature for the damaged medium, we use the temperature coefficient of the interband energy in c-GaAs near room temperature: -0.55 meV/K for E_1 and -0.50 meV/K the E_2 [Cohen and Chadi 1980]. For the most damaged sample, sample (d), the observed peak shifts for E_1 and E_2 are -0.15 eV and -0.20 eV, respectively,

corresponding to equivalent temperatures of 600 °K and 700 °K. Keep in mind that because of the different optical penetration depth at E_1 and E_2, E_1-energy photons probe to a depth of about 70 Å while E_2-energy photons probe a shallower (and more disordered) depth of about 30 Å. Thus the difference in equivalent temperature is in the right direction.

The slight shift in the LO Raman peak shown in Fig. 4.10 is not inconsistent with the equivalent temperature argument. The temperature coefficient of the LO peak is -1.3×10^{-2} cm^{-1}/K [Sapriel et al. 1986], which is shared by the volume-change mechanism and the electron-phonon interaction mechanism nearly equally [Cohen and Chadi 1980]. Only the electron-phonon interaction mechanism contributes to the equivalent temperature, so that a downshift of 0.5 cm^{-1} corresponds to an equivalent temperature of about 380 °K. The Raman spectrum in Fig. 4.11 was obtained with the 2.41-eV laser line, which has a large penetration depth of about 400 Å in the damaged medium. Thus the equivalent temperature averaged over the probed medium is expected to be substantially lower than the values obtained from the E_1 and E_2 interband peaks. A crude estimate of 400-500 °K is obtained from Fig. 4.8 and the E_1, E_2 estimates. The Raman estimate is slightly lower, but in the acceptable region.

Taken overall, the fact that the idea of an equivalent temperature (i.e., "frozen-in phonons") mimics most of the spectral effects seen in ion-etched GaAs appears to provide a useful clue to the nature of the structure in the damage layer in this material.

Table 4.1 Sample descriptions and ion-etch parameters

sample	fluence (ions/cm^2)	energy (keV)	current (μ-amp)	bombardment time
(a)	$1x10^{17}$	0.5	0.28	15 hrs 52 min
(b)	$1x10^{17}$	1.0	1.4	3 hrs 10 min
(c)	$1x10^{17}$	2.0	16	16 min 40 sec
(d)	$1x10^{17}$	3.89	36	7 min 24 sec

Table 4.2 Oscillator parameters of 3.89-keV Ar^+-etched GaAs and its starting crystal.[a]

Interband transition	E_i (eV)		Γ_i (eV)		F_i (eV)	
	c-GaAs	Ar^+:GaAs	c-GaAs	Ar^+:GaAs	c-GaAs	Ar^+:GaAS
E_1	2.92	2.64	0.19	0.86	2.23	4.44
$E_1+\Delta_1$	3.12	2.94	0.34	0.79	3.30	3.62
	3.41	3.40	0.65	0.87	3.65	3.86
	3.89	3.90	1.05	1.05	4.80	4.53
	4.55	4.30	0.74	1.36	7.45	7.08
E_2	4.84	4.66	0.36	0.93	4.40	2.92
	5.87	6.01	1.70	2.90	7.65	8.53
					ε_∞=1.5	ε_∞=1.5

[a] The parameter values listed in the table have been rounded off from the actual fitting parameters.

Table 4.3 Parameters of the graded damage profiles near the Ar^+:GaAs surfaces.

sample	d_{sput} (Å) [a]	R_p (Å) [a]	f_{max}	σ_p (Å)
(a)	500	35	0.04	30
(b)	500	40	0.11	128
(c)	500	45	0.19	269
(d)	500	50	0.42	286

[a] fixed

Figure Captions

Fig. 4.1 Raman scattering spectra of the Ar^+-etched GaAs sample. The top panel shows the spectrum of c-GaAs as a reference. The etching ion energy is given with each spectrum.

Fig. 4.2 Expanded view of the LO peaks of the Ar^+-bombarded GaAs spectra of Fig. 4.1.

Fig. 4.3 Reflectivity spectra, shown as points, of ion etched-GaAs. Repeated in each panel are the spectra of c-GaAs and a-GaAs for comparison.

Fig. 4.4 Reflectivity spectrum of Si^+-implanted GaAs with 120 keV, 2×10^{13} cm^{-2} implant. Also shown is the crystal spectrum.

Fig. 4.5 Real part of the dielectric function of Ar^+-etched GaAs, obtained by oscillator analysis from the reflectivity spectra of Fig. 4.3. The c-GaAs and a-GaAs spectra are shown for comparison.

Fig. 4.6 Imaginary part of the dielectric function of the ion-etched samples, along with the c-GaAs and a-GaAs counterparts.

Fig. 4.7 The LO Raman intensity of the Ar^+-bombarded and chemically etched samples. The points indicated by the symbols are the experimental data. The lines indicate the fits discussed in the text. For each chemically etched sample, the "fitting curve" is the line segments connecting points where the fit was done (at 100-Å intervals).

Fig. 4.8 Damage profile of the Ar^+-bombarded GaAs. The curves are derived from the fits of Fig. 4.8 using the Gaussian-sputtering model. The straight lines are from the fits to the data points of Fig. 4.8 using a simple linear profile with two parameters: f_{max} and d (damage depth).

Fig. 4.9 Reflectivity spectra of the Ar^+-bombarded and chemically etched GaAs samples. The chemical-etch depth is indicated with each spectrum.

Fig. 4.10 Raman comparison of ion-etched GaAs and

ion-implanted GaAs. The upper panel shows the LO Raman peak of the 3.89-keV Ar^+-etched sample (sample d in this study). The lower panel shows the LO peak of Be^+-implanted (45-keV Be^+ ions, 10^{14} ions/cm^2; see also Holtz et al. [1988]). Both penals include the c-GaAs spectrum of the virgin crystal prior to bombardment.

Fig. 4.11 Comparison of the reflectivity spectrum of ion-etched GaAs to that of ion-implanted GaAs. Dotted curves correspond to the spectrum of the 3.89-keV Ar^+ etched sample (upper penal) and the 45-keV Be^+ implanted sample (lower penal). The Both penals include the c-GaAs spectrum of the virgin crystal prior to bombardment.

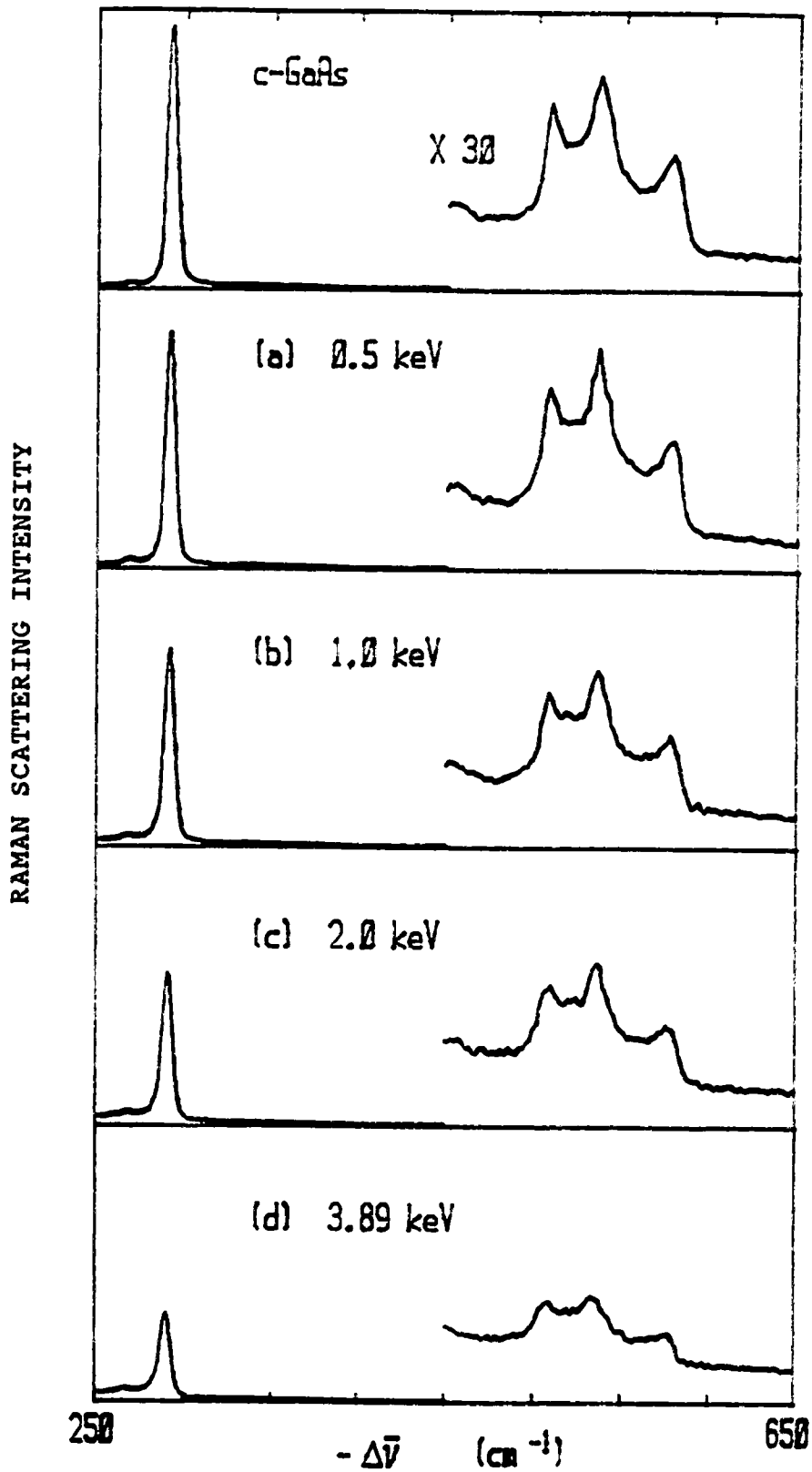

Fig. 4.1 Raman spectra of the Ar^+-bombarded GaAs

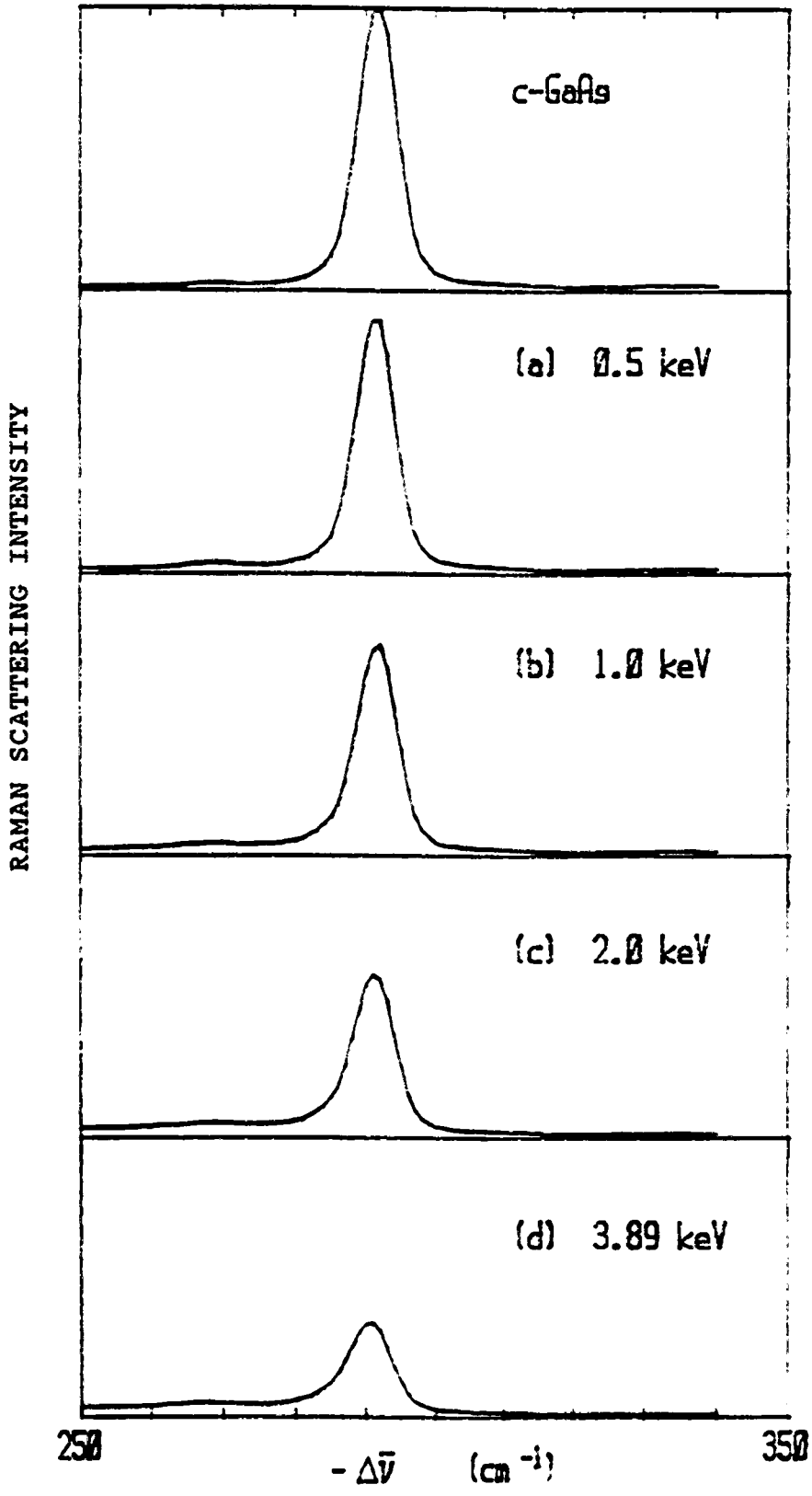

Fig. 4.2 The LO peaks of the Ar^+-bombarded GaAs

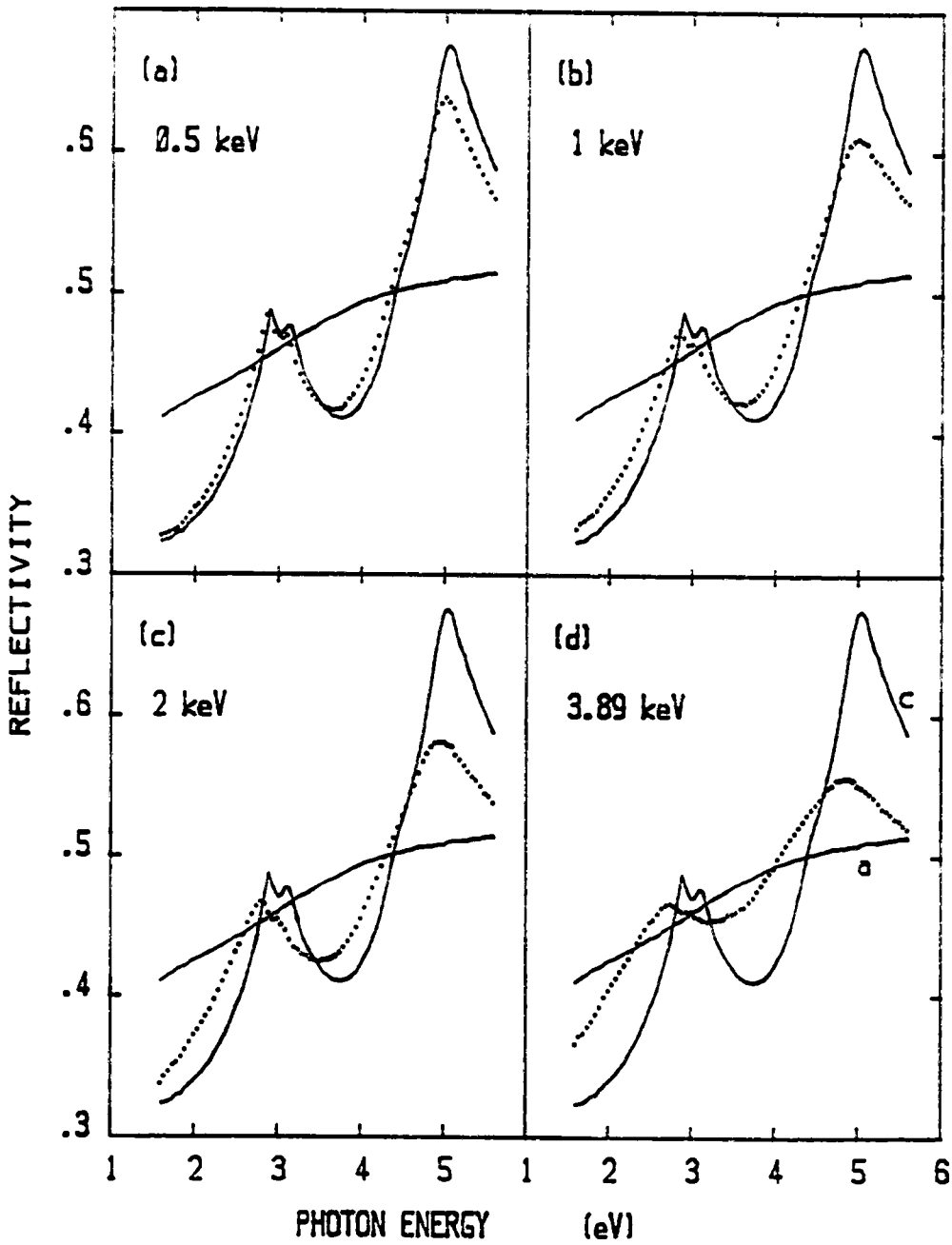

Fig. 4.3 Reflectivity spectra of the Ar^+-bombarded GaAs

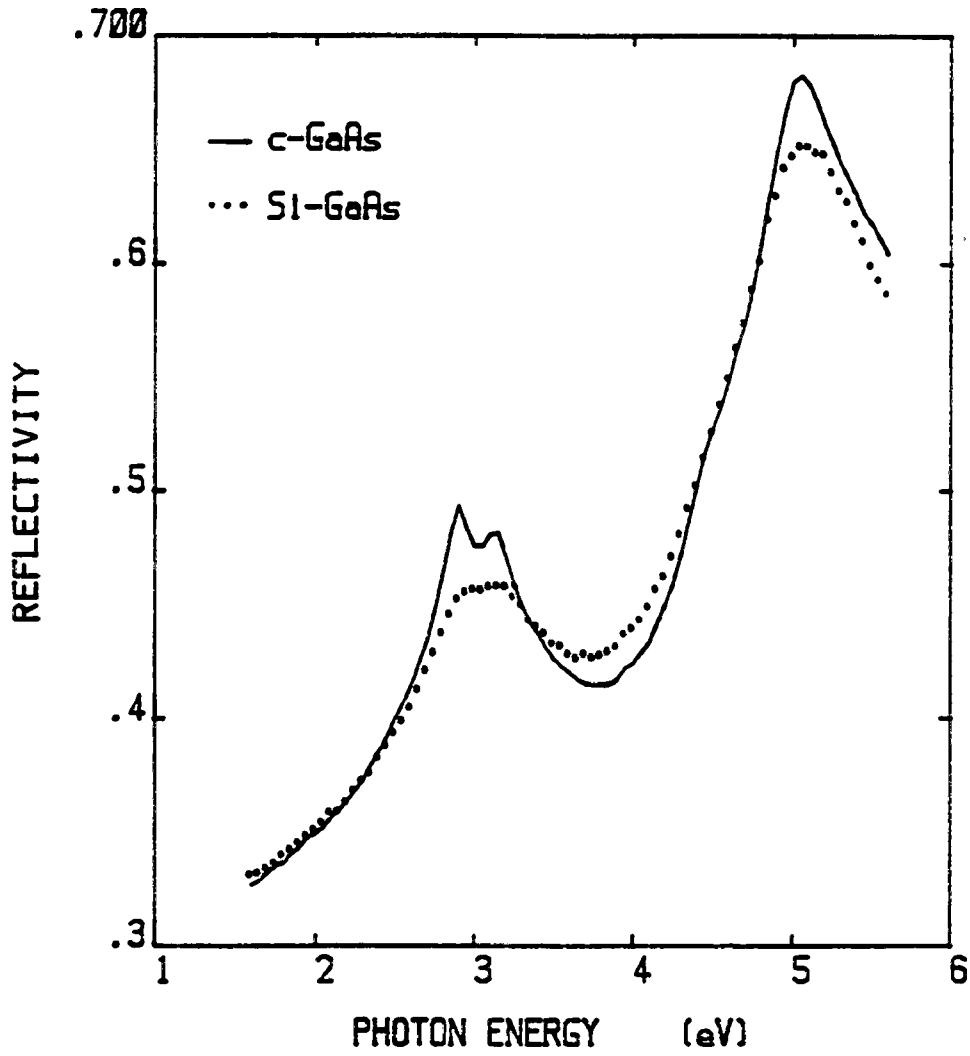

Fig. 4.4 Reflectivity spectrum of the Si^+-implanted GaAs

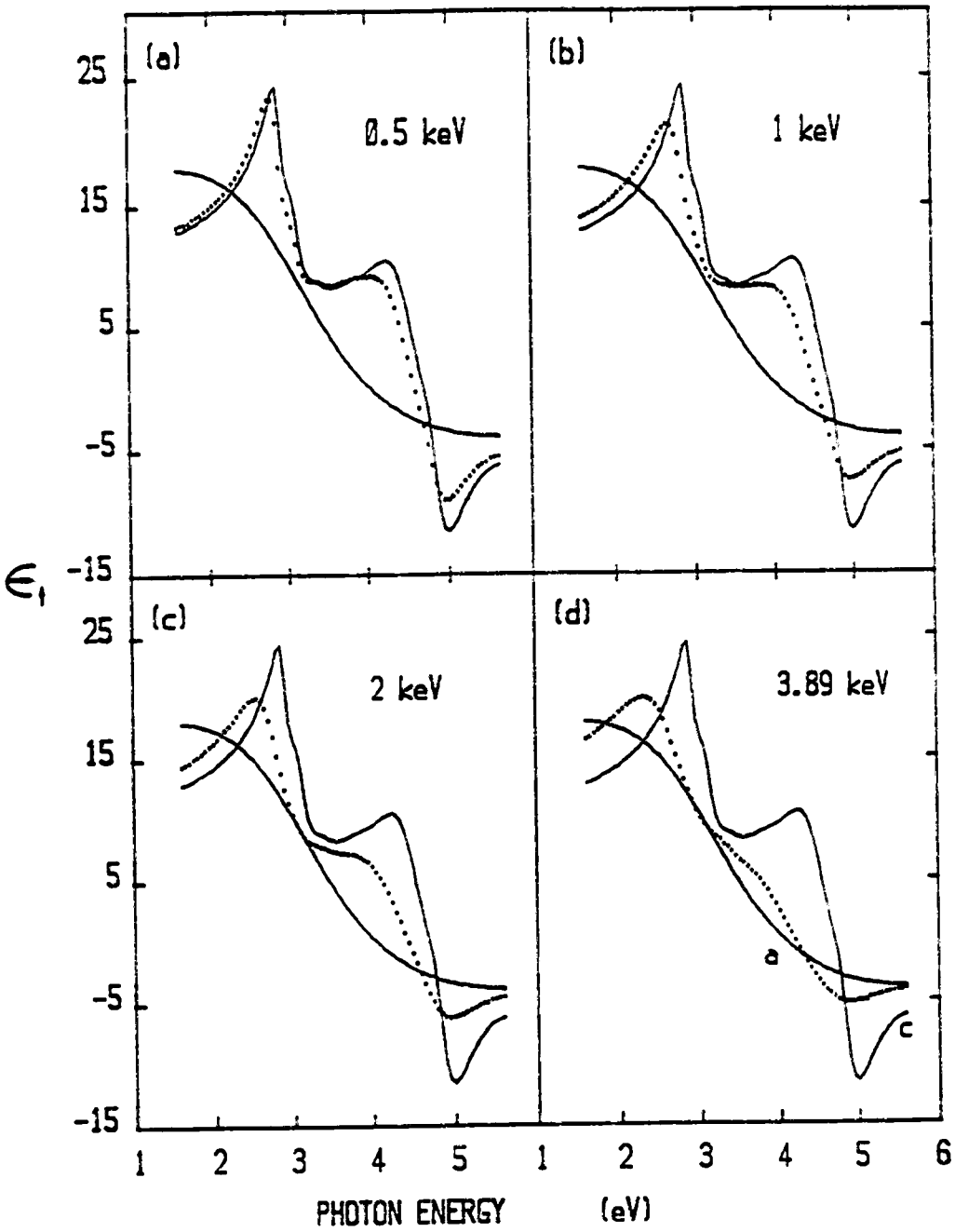

Fig. 4.5 ε_1 of the Ar^+-bombarded GaAs

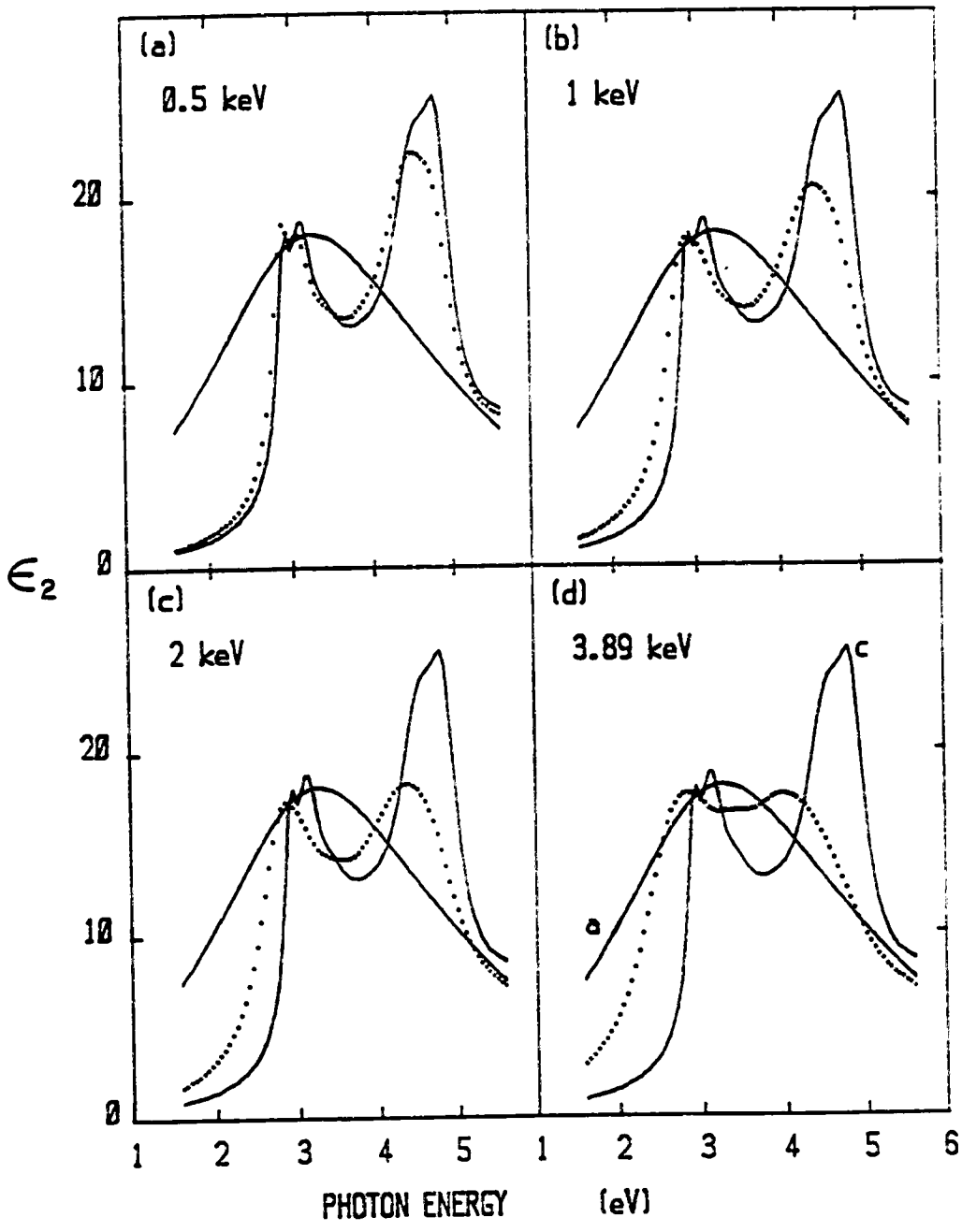

Fig. 4.6 ε_2 of the Ar^+-bombarded GaAs

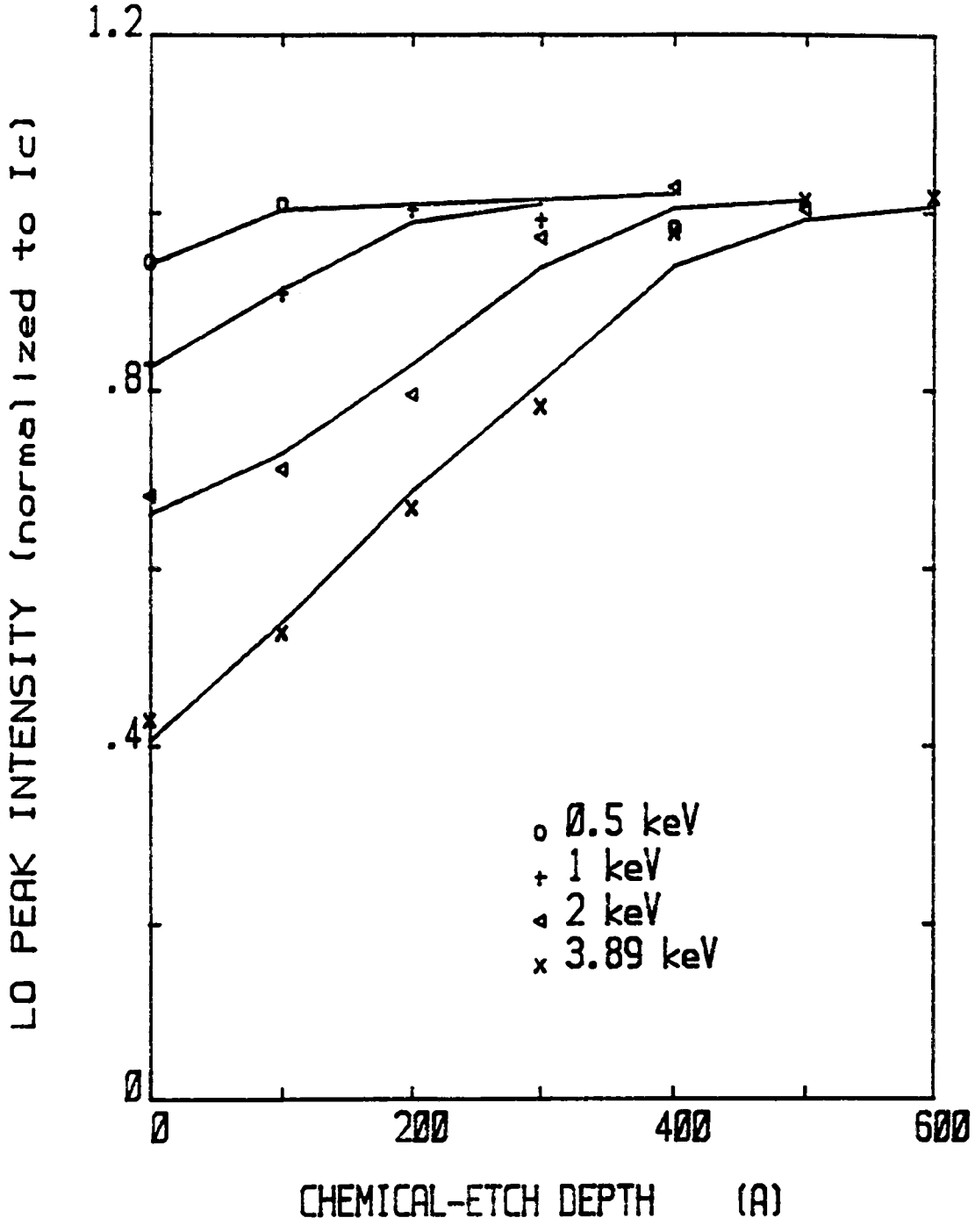

Fig. 4.7 The LO Raman intensity of the Ar^+-bombarded and chemical-etched GaAs

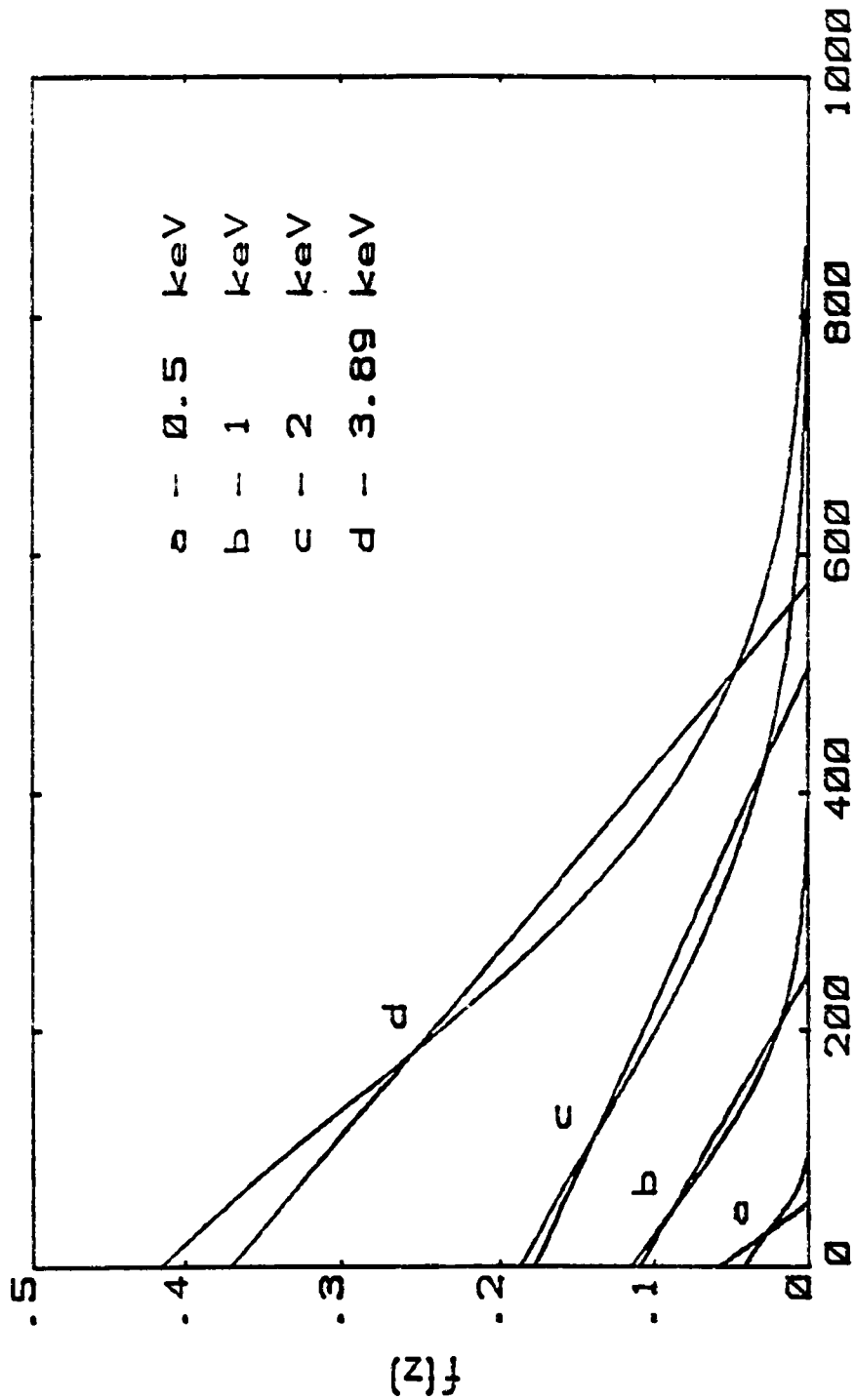

Fig. 4.8 Damage profiles of the Ar⁺-bombarded GaAs

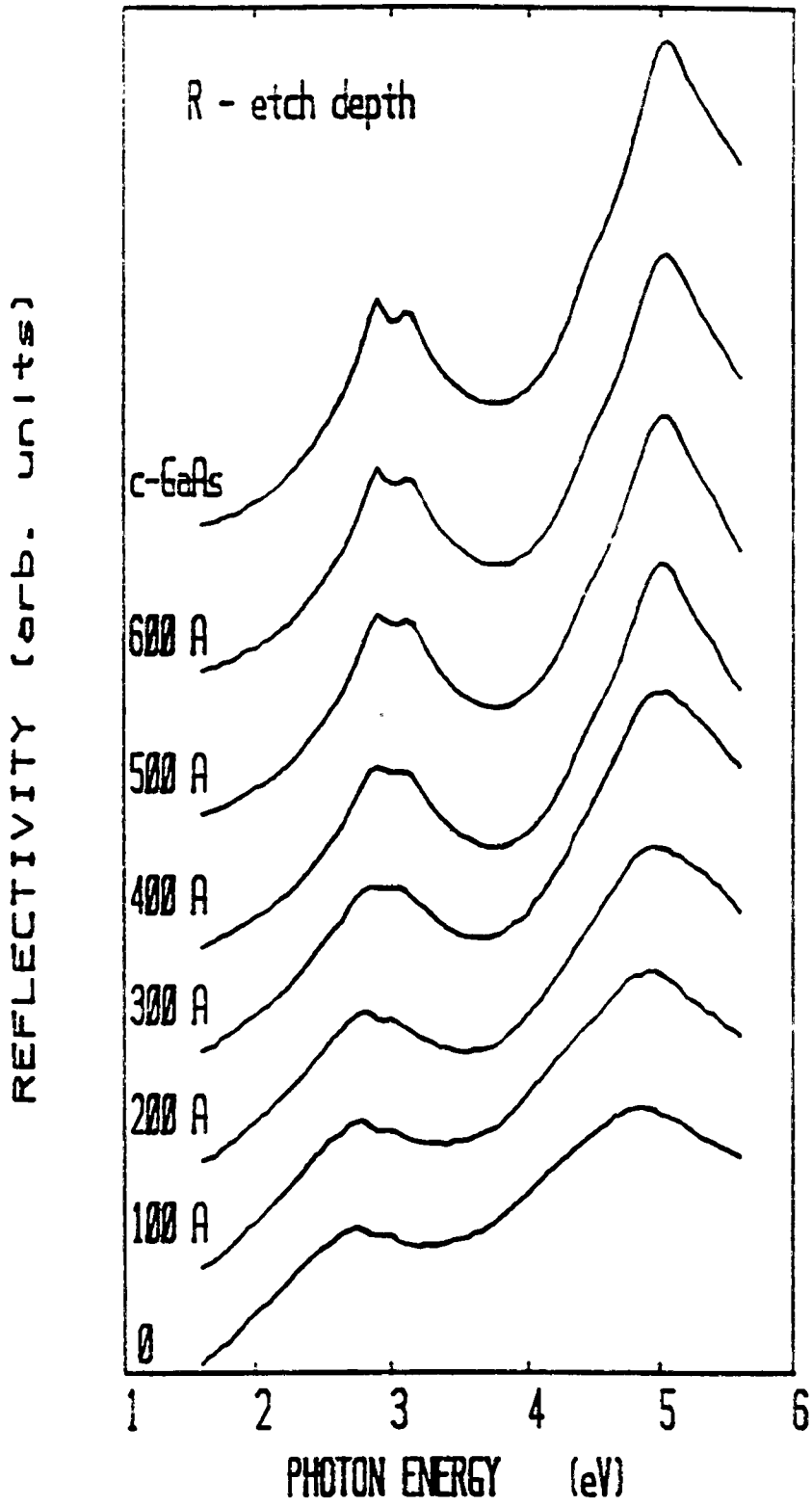

Fig. 4.9 Reflectivity spectra of the Ar^+-bombarded and chemical-etched GaAs

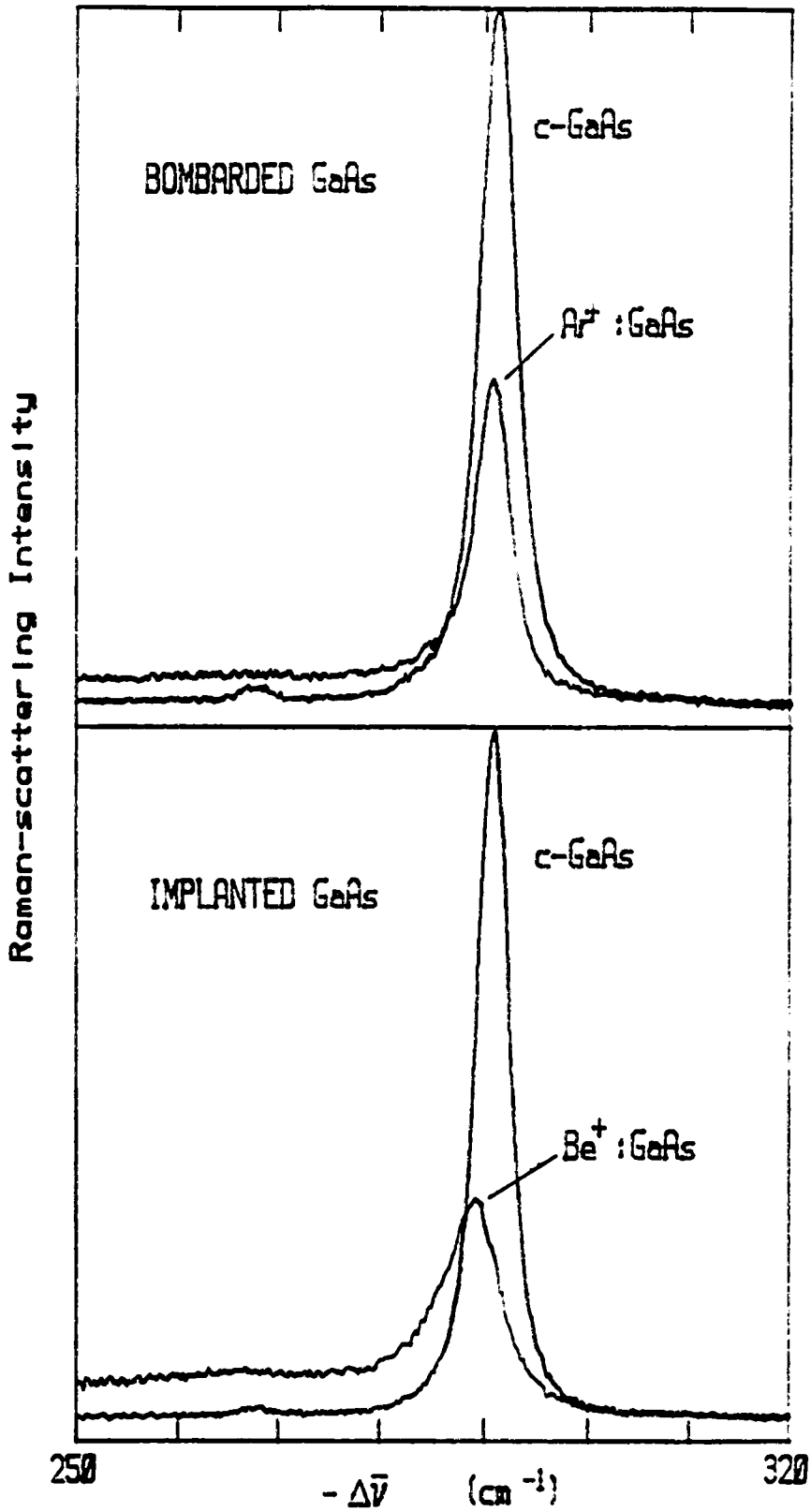

Fig. 4.10 The LO Raman peaks of (a) the Ar^+-bombarded GaAs and (b) the Be^+-implanted GaAs

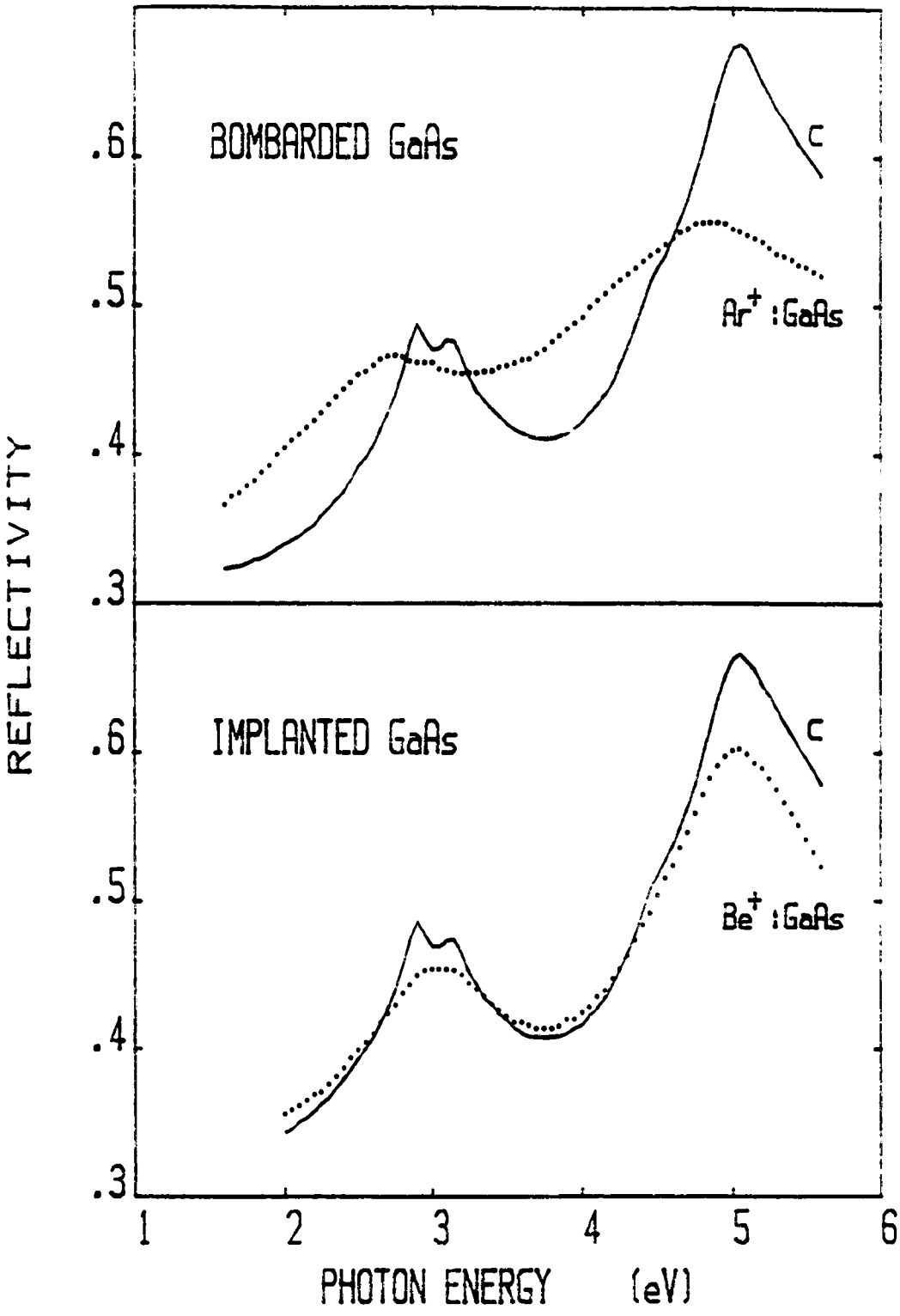

Fig. 4.11 The reflectivity spectra of (a) the Ar^+-bombarded and (b) the Be^+-implanted GaAs

CHAPTER 5

SUMMARY

A considerable amount of time was devoted to the optical spectrometer upgrade. By reducing the parasitic light residing in the original design, the spectrometer can now operate in the region up to 6 eV in photon energy. The computer automation that has been completed during the course of the present work not only increases the operation efficiency, it also greatly improves the precision of the spectrometer. The spectrometer control software and the optical data analysis software developed in this study will also be useful for future investigations.

The disorder in beryllium-ion implanted GaAs and argon-ion etched GaAs was studied by means of optical reflectivity and Raman-scattering experiments.

Finite-size effects on electronic excitations have been experimentally identified in the interband spectra of microcrystalline GaAs in Chapter 3. Visible-ultraviolet reflectivity measurements were carried out on a series of unannealed Be^+-implanted GaAs samples in which the implantation-induced damage layer is known (from previous Raman work) to consist of a fine-grain mixture of

amorphous and microcrystalline GaAs. Oscillator analysis was used to derive the optical dielectric function of the implanted layer from the observed reflectivity spectrum. Then, by inverting the effective medium approximation in an unconventional usage, the optical functions of the microcrystalline component, μ-GaAs, have been extracted from the optical properties of the two-phase damage layer. The optical properties of μ-GaAs are seen (Figs. 3.4-3.6) to differ appreciably from those of the bulk crystal (c-GaAs), with the difference increasing as the characteristic microcrystallite size (L) decreases.

The appropriate quantitative characterization of the evolution of the optical properties of μ-GaAs with decreasing L is given in terms of the spectral linewidths of the features associated with the E_1, $E_1+\Delta_1$, and E_2 direct interband transitions. As discussed in Sec. 3.5, the spectral changes induced by small L are found to be concentrated in these three linewidths. These linewidths increase linearly and rapidly (Fig. 3.7) with L^{-1}, the inverse microcrystal size. When L = 100 Å, the size-effect increase in linewidth is about 0.2 eV for the E_1 and E_2 peaks, comparable to the intrinsic bulk-crystal room-temperature linewidth.

A simple theory based on the uncertainty principle is found to account semi-quantitatively for the observations

on finite-size effects in μ-GaAs, notably the linear dependence of linewidth on L^{-1} as well as the magnitude of this dependence. Small microcrystal size implies a short time for excited carries to reach, and to be scattered by, the microcrystal boundary. This limits the excited-state lifetime and thus broadens the excited-state energy. The results indicate (Table 3.3) a severe lifetime limitation, of order 3×10^{-14} s, for microcrystallinity in the 100-Å range. The velocities indicated by the experimentally derived lifetimes are consistent with band-structure group velocities in GaAs. An alternative argument, also based on the uncertainty principle, can be expressed in terms of $\underline{k}$-space broadening of electron states: a $\underline{k}$-space spread of order $2\pi/L$ is implied by microcrystal size L. This viewpoint yields, via $E(\underline{k})$ energy-band dispersion, an equivalent linear relation between linewidth and L^{-1}, in agreement with experiment.

In the study of low-energy high-fluence Ar^+-ion etched GaAs, on the other hand, both Raman scattering and optical reflectivity experiments, together with wet chemical etching, have been carried out.

The LO Raman peak in the Ar^+-bombarded GaAs preserves the same lineshape as in the pristine bulk crystal, so that finite-size effects associated with microcrystallinity are absent. The peak intensity,

however, decreases substantially as ion energy increases. This observation leads to a provisional model for the structure of the damaged near-surface region in terms of a two-phase mixture: a crystalline phase which preserves the lattice vibrational properties of the unperturbed bulk crystal, and an amorphous phase intended to describe the collective effect of the high defect density and the localized regions of high disorder.

The damage profile in the near-surface region has been well characterized by a graded profile model. This model is built upon two physical processes simultaneously taking place during ion bombardment: Gaussian-like damage distribution produced by individual ions, and continuous sputtering removal of near-surface atoms during the bombardment. The fits to the measured LO intensity of the ion-bombarded and chemically etched samples result in a graded damage profile. The peak damage is at the surface, and it gradually decreases, not too differently from a simple linear profile. No complete amorphous layer is found for ion energy as high as 4 keV. The damage depth extends from less than 100 Å for the 0.5-keV etchant to about 600 Å for the 3.89-keV etchant. The reflectivity spectrum of the chemically etched specimen qualitatively supports this graded damage model.

In the reflectivity experiments on the Ar^+-etched

samples, we have observed peak position shifts in the interband transition features. A red shift (toward lower photon energy) of as much as 0.2 eV for the E_2 peak and 0.1 eV for the $E_1/E_1+\Delta_1$ doublet is seen in the reflectivity spectrum of the most damaged sample. The red shifts appear to be interpretable in terms of an equivalent temperature of about 600-700 °K, suggesting that a "frozen-phonon" picture of the disorder may be appropriate for the damage layer in ion-etched material.

REFERENCES

Aspnes, D.E., 1982, Thin Solid Films 89, 249.

Aspnes, D.E., 1984, Characterization of Materials and Interfaces by Visible-near UV Optical Spectroscopy, MRS Symposium X (Boston), J. Mater, ed.

Aspnes, D.E., 1988, private communication.

Aspnes, D.E., and A.A. Studna, 1983, Phys. Rev. B 27, 985.

Aspnes, D.E., S.M. Kelso, C.G. Olson, and D.W. Lynch, 1982, Phys. Rev. Lett 48, 1863.

Berg, R.S. and P.Y. Yu, 1987, Phys. Rev. B 35, 2205.

Birman, J.L., 1974, Theory of Crystal Space Groups and Infra-Red and Raman Lattice Processes, in Encyclopedia of Physics, L. Genzel, ed. (Springer-Verlag).

Blakemore, J.S., 1982, J. Appl. Phys. 53, R123.

Brodsky, M.H., 1975, in Light Scattering in Solids, M. Cardona, ed. (Springer-Verlag).

Bromley, D.A., 1985, ed., Treatise on Heavy-Ion Science Vol. 6, (Plenum).

Bruggeman, A.G., 1935, Ann. Phys. (Leipzig) 24, 636.

Buchner, S and E. Burstein, 1974, Phys. Rev. Lett. 33, 908.

Burns, G, 1985, Solid State Physics, (Academic Press).

Cardona, M., 1961, J. Appl. Phys. 32, 2151.

Cardona, M., 1982, in Light Scattering in Solids II, M. Cardona and G. Guntherodt, ed. (Springer-Verlag).

Chelikowsky, J.R. and M.L. Cohen, 1976, Phys. Rev. B 14, 556.

Chen, L, J. Tauc, and Z. Vardeny, to be published.

Clegg, J.B., 1987, Surface and Interface Analysis, 10, 332.

Cohen, M.H., 1958, Phil. Mag. 3, 762.

Cohen, M.L., and J.R. Chelikowsky, 1982, "Pseudopotentials for semiconductors", in Handbook on Semiconductors 1, W. Paul, ed. (North-Holland).

Cohen, M.L., and J.R. Chelikowsky, 1988, Electronic Structure and Optical Properties of Semiconductors, (Springer-Verlag).

Cummings, K.D., 1982, Ph.D. Dissertation, Ohio State University.

Dorner, B. and D. Strauch, 1987, private communication.

Duncan, W.M. and G. Westphal, in VLSI Electronics: Microstructure Science, Einspruch and Wisseman, eds., (Academic Press, New York).

Ehrenreich, H., H.R. Philipp, and J.C. Phillips, 1962, Phys. Rev. Lett. 8, 59.

Elliott, J.P. and P.G. Dawber, 1979, Symmetry in Physics Volume 1, (MacMillan).

English, C.A. and M.L. Jenkins, in Treatise on Heavy-Ion Science Vol. 6, D.A. Dromley, ed., (Plenum).

Epp, J.M., 1988, private communication.

Epp, J.M. and J.G. Dillard, 1989, Chem. Mat. 1.

Erman, M., J.B. Theeten, P. Chambon, S.M. Kelso, and D.E. Aspnes, 1984, J. Appl. Phys. 56, 2664.

Gargouri, M., B. Prevot, and C. Schwab, 1987, J. Appl. Phys. 62, 3902.

Greenaway, D.L., 1962, Phys. Rev. Lett. 9, 97.

Grimsditch, M.H., D. Olego, and M. Cardona, 1979, in Light Scattering in solids, J.L. Birman, H.Z. Cummins, and K.K. Rebane, ed., (Plenum).

Hayes, W and R. Loudon, 1978, scattering of Light by crystals, (John Wiley and Sons).

Hoffman, D.M., 1982, Ph.D. Dissertation, Ohio State University.

Holtz, M, 1987, Ph.D. Dissertation, Virginia Tech.

Holtz, M, R. Zallen, O. Brafman and S. Matteson, 1988, Phys. Rev. B 37, 4609.

IMSL User's Manual, 1984, Math/pc-Library.

Iqbal, Z., and S. Veprek, 1982, J. Phys. C 15, 377.

Jones, K.S., D.K. Sadana, S. Prussin J. Washburn, E.R. Weber, and W.J. Hamilton, 1988, J. Appl. Phys. 63, 1414.

Johnson, R.E., B. Sundqvist, P. Hakansson, A. Hedin, M. Salehpour and G. Save, 1987, Surface Science, 179, 187.

Kawable, M., N. Masuda, and S. Namba, 1978, Appl. Optics, 17, 2556.

Kumar, S, B. Drevillon, and C. Godet, 1986, J. Appl. Phys. 60, 1542 (1986).

Lautenschlager, P., M. Garriga, S. Logothetidis, and M. Cardona, 1987, Phys. Rev. B 35, 9174.

Lindhard, J., M.E. Scharff, and H.E. Schiott, 1963, Kl. Dan. Vid. Selsk. Mat. Fys. Medd. 13, No.14.

Liou, L.L, W.G. Spitzer, J.E. Fredrickson, and S. Kwun, 1986, J. Appl. Phys. 59, 1927.

Liu, H.N., D. Pfost, and J. Tauc, 1984, Solid State Commun. 50, 987.

Loudon, R, 1964, Adv. Phys. 13, 423.

Lax, M., 1974, Symmetry Principles in Solid State and Molecular Physics, (John Wiley & sons).

Martin, R.M. and L.M. Falicov, 1975, in Light Scattering in Solids I, M. Cardona, ed. (Springer-Verlag).

Martinez, G., 1980, in Handbook on Semiconductors 2, M. Balkanski, ed., (North-Holland).

McLevige, W, 1978, Ph.D. Dissertation, University of Illinois.

Menendez, J. and M. Cardona, 1985, Phys. Rev. B 31, 3696.

Mu, X.C., S.J.Fonash, B.Y.Yang, K.Vedam, A.Rohatgi and J. Rieger, 1985, J. Appl. Phys., 58, 4262.

Nye, J.F., 1957, Physical Properties of Crystals, (Clarendon, Oxford).

Nye, J.F., 1987, Physical Properties of Crystals 2nd. ed., (Clarendon, Oxford).

Pang, W.S., 1984, Solid State Technology, 27, 249.

Pang, W.S., 1986, J. Electrochem. Soc. 133, 784.

Parmenter, R.H., 1955, Phys. Rev. 100, 573.

Petroff, Y, 1980, in Handbook on Semiconductors 2, M. Balkanski, ed., (North-Holland).

Phillips, J.C., 1966, in Solid State Physics, ed. F. Seitz and D. Turnbull, Vol.18, 55.

Pinczuk, A. and E. Burstein, 1975, in Light Scatering in Solids, M. Cardona, ed., (Springer-Verlag).

Poate, J.M., 1985 in Treaties on Heavy-Ion Science Vol.6, p.133, D.A. Bromley, ed. (Plenum).

Prussin, S., D.I. Margolese, and R. Tauber, 1985, J. Appl. Phys. 57, 180.

Richter, H, and L. Ley, 1981, J. Appl. Phys. 52, 7281.

Richter, H., Z.P. Wang, and L. Ley, 1981, Solid State Commun. 39, 625.

Sadana, D.K., 1985, Nucl. Inst. Meth. Phys. Res. B 7/8, 375.

Sapriel, J., J. Chvignon, F. Alexandre, and R. Azoulay, 1986, Phys. Rev. B 34, 7118.

Sell, D.D., H.C. Casey, and K.W. wetch, 1974, J. Appl. Phys. 45, 2650.

Spitzer, W.G, and D.A. Kleinman, 1961, Phys. Rev. 121, 1324.

Shiles, E., T. Sasaki, M. Inokuti, and D.Y. Smith, 1980, Phys. Rev. B 22, 1612.

Shur, M., 1986, GaAs Devices and Circuits, (Plenum).

Sze, S.M., 1981, Physics of Semiconductor Devices, 2nd Ed., (John Wiley and Sons).

Trommer, R. and M. Cardona, 1978, Phys. Rev. B 17, 1865.

Van Hove, L., 1953, Phys. Rev. 89, 1189.

Veprek, S., F.A. Sarott, and Z. Iqbal, 1987, Phys. Rev. B 36, 3344 (1987).

Verleur, H.W., 1968, J. Opt. Soc. Am. 58, 1356.

Wagner, J. and Ch. Hoffman, 1987, Appl. Phys. Lett. 50, 682.

Wilson, R.G. and R.R. Brewer, 1979, Ion Beam: With application to Ion Implantation, (Robert E. Krieger).

Wooten, F., 1972, Optical Properties of Solids, (Academic Press).

Zallen, R. and W. Paul, 1967, Phys. Rev. 155, 703.

Zallen, R., 1982, in Handbook on Semiconductors Vol.1, W. Paul, ed. (North- Holland).

Zallen, R., 1983, The Physics of Amorphous Solids, (John Wiley & sons).

APPENDIX

OPTICAL SPECTROMETER CONTROL SOFTWARE

```
1 REM ************************************************************************
2 REM * THIS PROGRAM IS THE CONTROL  SOFTWEAR  THAT OPERATES  THE PRISM-  *
3 REM * GRATING SPECTROMETER.THE SPECTROMETER IS A MODIFIED PERKIN-ELMER *
4 REM * MODEL 16 SPECTROMETER WITH MODEL 160  MONOCHROMATER AS THE FIRST *
5 REM * STAGE. THE OPERATING RANGE IN  PHOTON  ENERGY IS FROM 0.08 eV TO *
6 REM * 6.2 eV. THIS  SOFTWEAR IS  PROGRAMMED FOR MEASUREMENTS OF SOURCE *
7 REM * INTENSITY, TRANSMITTANCE, AND REFLECTIVITY,AS WELL AS FOR MIRROR *
8 REM * CALIBRATION.                                                      *
9 REM ************************************************************************
10 CLS 0: SCREEN 0
11 PRINT "    ************************************************************"
12 PRINT "    *                        S O S                             *"
13 PRINT "    *                      ==========                          *"
14 PRINT "    *              SPECTROMETER OPERATION SOFTWEAR             *"
15 PRINT "    *                                                          *"
16 PRINT "    *                    BY G. JEFF FENG                       *"
17 PRINT "    *                      OCTOBER 1986                        *"
18 PRINT "    *                                                          *"
19 PRINT "    ************************************************************"
20 PRINT:PRINT:PRINT
30  PRINT "     TO RUN THIS PROGRAM THE FOLLOWINGS MUST BE DONE:          "
40  PRINT
50  PRINT "          * LOCK-IN AMPLIFIER ON WITH:                        "
60  PRINT "          *       TIME CONST.=300ms FOR PMTDETECTOR           "
70  PRINT "          *       TIME CONST.=1s    FOR PYROELECTRONIC DETECTOR"
80  PRINT "          * MOTORS ON WITH                                    "
90  PRINT "          * BOTH PRISM DRUM AND GRATING DRUM AT 2000          "
100 PRINT:PRINT
110 INPUT "                   PRESS 'RETURN' WHEN READY .....          ";AS
120 REM ************************ MAIN PROGRAM ****************************
130 REM **** ARRAY DIMENSION ****
140 REM DATA ARRAY DIMENSION 301 CAN BE EXPANDED
150 DEFINT N,I-J
160 DIM SS(23),X(301),Y(301),MR(301),MI(301),SI(301),DRFT(301),BI(301)
170 DIM YY(301),SQV(301),YOL(20,3),XOL(20,3),MII(20,3),SII(20,3)
180 REM **** GRAPHIC AND TEXT AREA ****
190 SCREEN 3: REM 610x400 GRAPHIC MODE
200 VIEW (101,21)-(500,270),,1: REM GRAPHIC WINDOW
210 VIEW PRINT 20 TO 24: REM BOTTOM FIVE LINES AS TEXT MODE
220 REM **** DEFAULTS ****
230 NSCAN=1 : NAPDUM=20: NMF=2 : J3=0 :  REM CONTROL SCAN
240 NDP=5 : MTK%=0 : ETK%=0 : GTK%=0 : NOL=0
250 GRAT%=0 : SOUR%=0 : DETE%=0 : REM GRATING,SOURCE AND DETECTOR
260 BELL$=CHR$(7)+CHR$(7)
300 REM **** DEFINE SOME FUNCTIONS ****
```

```
310 DEF FNYS(J)=(VOLT+DUMY*(J1-1))/J1: REM AUTOMATIC AVERAGE OVER SCANS
320 DEF FNYR(J)=((VOLT-BI(J))*MR(J)/(MI(J)-BI(J))+DUMY*(J1-1))/J1
330 DEF FNYT(J)=(VOLT/SI(J)+DUMY*(J1-1))/J1
340 DEF FNYM(J)=(SQR(VOLT/SI(J))+DUMY*(J1-1))/J1
350 DEF FNPDRUV(E)=1864.32+16.75*E+.454*E^2+.99*E^3 : REM PRISM DRUM (UV)
360 DEF FNPDRIR(E)=1214.02+2524.37*E-3875.42*E^2+2933.79*E^3-1078.89*E^4
    +154.21*E^5 : REM PRISM DRUM (V-IR)
370 DEF FNGDR(E)=AA*E^2+BB*E+CC : REM DRUM READING AS A FUNCTON OF ENERGY
372 DEF FNPMPIR(E)=-12800!*(2000!-FNPDRIR(E))/100!:REM PRISM MOTOR POSITON
380 DEF FNPMPUV(E)=-12800!*(2000!-FNPDRUV(E))/100!:REM PRISM MOTOR POSITON
390 DEF FNPMPIR(E)=-12800!*(2000!-FNPDRIR(E))/100!:REM PRISM MOTOR POSITON
400 DEF FNGMP(E)=12800!*(2000!-FNGDR(E))/100! : REM GRATING MOTOR POSITON
410 REM **** OPEN SERIAL PORTS ****
420 OPEN "COM2:9600,N,8,1" AS #8
430 OPEN "COM3:4800,E,7,1" AS #7
440 REM **** GRATING AND FILTER LIMITS ****
450 AA=.35936  :BB=518.388 :CC=-1110.739
460 ED(1)=1.5 : ED(2)=0!
470 EG(1)=2.3: EG(2)=1.15: EG(3)=.51: EG(4)=.19: EG(5)=.08
480 ES(1)=3.2 : ES(2)=.5  : ES(3)=0!
490 NG=5 : NS=3 : ND=2 : REM NUMBER OF GRATINGS, SOURECS AND DETECTORS
500 REM **** MAIN MANU ****
520 GOSUB 6400 : LOCATE 20,1
522 PRINT TAB(10) "     ***************** MAIN MENU *****************     "
530 PRINT TAB(10) "M----MODE       ;  E----MOTOR ENGAGE; G----SET GRAPHIC"
540 PRINT TAB(10) "S----SCAN       ;  P----PLOT        ; F----FILE       "
550 PRINT TAB(10) "Z----MOTOR ZERO ;  Q----QUIT        ;                 "
560 INPUT MQ$
600 IF MQ$="M" THEN GOSUB 800
610 IF MQ$="G" THEN GOSUB 5000
620 IF MQ$="E" THEN GOSUB 1700
640 IF MQ$="S" THEN GOSUB 2500
650 IF MQ$="P" THEN GOSUB 4500
660 IF MQ$="F" THEN GOSUB 7500
670 IF MQ$="Z" THEN GOSUB 8000
680 IF MQ$="Q" GOTO 8100
690 GOTO 520
800 REM **** SUBROUTINE  MODE SELECTION ****
810 GOSUB 6400 : LOCATE 20,1
820 PRINT TAB(10) "             **** MODE SELECTION ****                  "
830 PRINT TAB(10) "R----SAMPLE REFLECTANCE; T----SAMPLE TRANSMITTANCE   ;"
840 PRINT TAB(10) "M----MIRROR REFLECTANCE; S----SOURCE/MIRROR INTENSITY;"
845 PRINT TAB(10) "Q----QUIT              ;                              "
850 INPUT MODE$
855 IF MODE$="Q" THEN RETURN
860 IF MODE$="S" GOTO 1200
870 IF MODE$="T" OR MODE$="M" GOTO 1050
880 IF MODE$="R" GOTO 900
890 GOTO 810
900 REM **** SUPPLY MR AND MI ****
```

```
910 GOSUB 6400 : LOCATE 20,1
920 PRINT "    SUPPLY MIRROR REFLECTANCE(MR) FILE:"
930 INPUT "    ENTER FILENAME  ";FMR$
932 PRINT "    SUPPLY MIRROR INTENSITY(MI) FILE:"
934 INPUT "    ENTER FILENAME  ";FMI$
936 PRINT "    SUPPLY BACKGROUD (BI) FILE:"
938 INPUT "    ENTER FILENAME  ";FBI$
940 OPEN "I",#2,FBI$
942 INPUT#2,COMM$ : INPUT#2,COMM$
944 I=0
945 WHILE NOT EOF(2)
946   I=I+1
947 INPUT#2,X(I),BI(I)
948 WEND
949 CLOSE(2)
950 OPEN "I",#2,FMR$
952 INPUT#2,COMMR$
954 I=0
955 WHILE NOT EOF(2)
956   I=I+1
957 INPUT#2,X(I),MR(I)
959 WEND
960 CLOSE(2)
962 NDP=I
970 OPEN "I",#2,FMI$
972 INPUT#2,COMM$
974 INPUT#2,NDP,NOL
976 FOR I=1 TO NDP: INPUT#2,X(I),MI(I)
980 NEXT I
990 CLOSE(2)
992 E1=X(1) :  E2=X(NDP)
1000 MTK%=1
1010 GOTO 500
1040 REM **** SUPPLY SI FILE ****
1050 GOSUB 6400 : LOCATE 20,1
1060 PRINT "    SUPPLY SOUCE INTENSITY FILE:"
1070 INPUT "    ENTER FILENAME  ";FSI$
1080 OPEN "I",#2,FSI$
1090 INPUT#2,COMMS$
1100 INPUT#2,NDP,NOL
1110 FOR I=1 TO NDP: INPUT#2,X(I),SI(I)
1115 IF MODE$="R" THEN MI(I)=SI(I)
1117 NEXT I
1120 FOR I=1 TO NOL
1130  FOR II=1 TO 3:INPUT#2,XOL(I,II),SII(I,II) : NEXT II
1135 IF MODE$="R" THEN MII(I)=SII(I)
1140 NEXT I
1150 CLOSE(2)
1160 E1=X(1) : E2=X(NDP)
1170 MTK%=1
```

```
1180 RETURN
1200 REM **** SET SCAN PARAMETERS ****
1210 GOSUB 6400 : LOCATE 20,1
1220 PRINT "    SCAN REGION SHOULD BE WITHIN 6.2 EV TO 0.08 EV."
1230 PRINT
1240 INPUT "    ENTER: E-MIN, E-MAX ";E2,E1
1250 INPUT "    ENTER: # OF DATA POINTS ( <300 )";NDP
1260 FOR I=1 TO NDP
1270 X(I)=E1-(I-1)*(E1-E2)/(NDP-1)
1280 NEXT I
1290 MTK%=1 : RETURN
1300 REM **** SELECT SOURCE  ****
1310 GOSUB 6400 : LOCATE 20,1
1320 DUMS%=SOUR%
1330 IF EE<=6.2  AND EE>=3.2 THEN SOUR%=1
1340 IF EE<=3.3  AND EE>=.5  THEN SOUR%=2
1350 IF EE<=.5               THEN SOUR%=3
1360 IF DUMS%=SOUR% THEN RETURN
1362 IF SOUR%=1 THEN PRINT "    ENGAGE D2-LAMP"
1364 IF SOUR%=2 THEN PRINT "    ENGAGE  W-LAMP"
1366 IF SOUR%=3 THEN PRINT "    ENGAGE GLOBAR "
1370 PRINT BELL$
1380 INPUT "    THEN, PRESS 'RETURN' ";Q$
1390 RETURN
1400 REM **** SELECT DETECTOR ****
1410 GOSUB 6400 : LOCATE 20,1
1420 DUMD%=DETE%
1430 IF EE<=6.2 AND EE>=1.5 THEN DETE%=1
1440 IF EE<=1.6             THEN DETE%=2
1450 IF DUMD%=DETE% THEN RETURN
1452 IF DETE%=1 THEN PRINT "    ENGAGE VUV-DETECTOR"
1454 IF DETE%=2 THEN PRINT "    ENGAGE  IR-DETECTOR"
1460 PRINT BELL$
1470 INPUT "    THEN, PRESS 'RETURN' ";Q$
1480 RETURN
1500 REM **** SELECT GRATING  ****
1510 DUMG%=GRAT%
1520 IF EE<=6.2   AND EE>=2.3  THEN GRAT%=1  :AA=.35936:BB=518.388
1530 IF EE<=3.2   AND EE>=1.15 THEN GRAT%=2  :AA=1.43744:BB=1036.776
1540 IF EE<=1.35  AND EE>=.51  THEN GRAT%=3  :AA=7.27704:BB=2332.746
1550 IF EE<=.545  AND EE>=.19  THEN GRAT%=4  :AA=51.7478:BB=6220.656
1560 IF EE<=.229  AND EE>=.08  THEN GRAT%=5  :AA=292.194:BB=14781.76
1570 IF EE>6.2 OR EE<.08  THEN PRINT BELL$
1580 IF EE>6.2 OR EE<.08  THEN PRINT "    INCORRECT ENERGY REGION!":STOP
1590 IF DUMG%=GRAT% THEN RETURN
1600 GOSUB 6400 : LOCATE 20,1
1610 PRINT "    ENGAGE #";GRAT%;" GRATING"
1620 PRINT BELL$
1630 INPUT "    THEN, PRESS 'RETURN' ";Q$
1640 IF FNGDR(EE)<=2300! AND FNGDR(EE)>=30! THEN RETURN
```

```
1650 PRINT BELL$
1660 PRINT "    ENERGY REGION DOSE NOT MATCH THE GRATING!"
1670 STOP
1700 REM **** MOVE MOTOR TO E-MAX POSITION   ****
1710 IF MTK%=0 THEN GOSUB 800
1720 GOSUB 6400 : LOCATE 20,1
1730 PRINT "    SCAN REGION: FROM ";E1;" EV TO ";E2;" EV"
1740 PRINT "    DATA POINTS: ";NDP
1750 FOR I=1 TO 500 : A=2!*3^3 : NEXT I
1760 EE=E1
1770 GOSUB 1500:GOSUB 1300:GOSUB 1400:REM SELECT GRATING,SOURCE,DETECTOR
1780 PRINT "    PRISM   POSITION SHOULD BE 2000 WHEN MOTOR POWER ON"
1790 PRINT "    GRATING POSITION SHOULD BE 2000 WHEN MOTOR POWER ON"
1800 INPUT "    CORRECT? Y/N ";Q$
1810 IF Q$<>"Y" THEN PRINT "    CHECK DRUM POSOTIONS !!"+BELL$: STOP
1910 PMP$=STR$(INT(FNPMPUV(X(1))))
1912 IF X(1)<=2! THEN PMP$=STR$(INT(FNPMPIR(X(1))))
1915 IF VAL(PMP$)>=0! THEN PMP$=RIGHT$(PMP$,(LEN(PMP$)-1))
1920 GMP$=STR$(INT(FNGMP(X(1))))
1925 IF FNGMP(X(1))>=0! THEN GMP$=RIGHT$(GMP$,(LEN(GMP$)-1))
1930 PRINT "       MOTOR WINDING ... "
1940 GMM$="8MPA 8A0.2 8V0.1 8D"+GMP$+" 8G"
1950 PMM$="7MPA 7A0.2 7V0.1 7D"+PMP$+" 7G"
1960 GOSUB 4300 : REM MOVE PRISM TO EMAX
1970 GOSUB 4000 : REM MOVE GRATING TO EMAX
1980 IF X(1)>2! THEN PRINT "    PRISM  POSITION SHOULD BE ";FNPDRUV(X(1))
1982 IF X(1)<=2! THEN PRINT "    PRISM  POSITION SHOULD BE ";FNPDRIR(X(1))
1990 PRINT "    GRATING POSITION SHOULD BE ";FNGDR(X(1))
2000 INPUT "    CORRECT?  Y/N ";Q$
2010 IF Q$="N" THEN STOP
2020 FOR I=1 TO 200 : X=2*3!^3 : NEXT I
2030 ETK%=1 : RETURN
2200 REM ************************************************************
2210 REM *              **** SUBROUTINE TAKE DATA ****                *
2220 REM *THIS SUBROUTINE READS LOCK-IN OUTPUT,CHECK CURRENT SENSITIVITY*
2230 REM *AND AUTO SET THE SENSITIVITY IF NOT MATCHING THE OUTPUT.      *
2240 REM *THE OUTPUT IS STORED IN 'VOLT'.                               *
2241 REM ************************************************************
2242 IF EE>4.8 THEN NAP=NAPDUM*2
2243 IF EE>5.4 THEN NAP=NAPDUM*3
2244 IF EE>5.6 THEN NAP=NAPDUM*4
2245 IF EE>5.8 THEN NAP=NAPDUM*8
2246 IF EE<=4.8 THEN NAP=NAPDUM
2248 LOWTK%=0
2250 SUM=0!:VOLT=0!:R=0!
2255 FOR I=1 TO 50 : DUMMY=2*3!^2 : NEXT I   : REM DELAY
2260 PRINT#7,"S":INPUT#7,A$,NS$:NS=VAL(NS$)
2270 DUMMY=NS-(INT(NS/3)*3)+1
2280 IF DUMMY=1 THEN DUMMY=5
2290 IF DUMMY=3 THEN DUMMY=1
```

```
2300 SNS=(10^-INT(NS/3))*DUMMY
2305 FOR I=1 TO 1000: DUMMY=2*3!^2 : NEXT I    : REM DELAY
2310 FOR JL=1 TO NAP :REM NAP=# OF AVERAGE POINTS
2315 FOR I=1 TO 20: DUMMY=2*3!^2 : NEXT I    : REM DELAY
2320 PRINT#7,"Q1":INPUT#7,A$,R$
2330 R=VAL(R$)
2340 SUM=SUM+R
2350 NEXT JL
2360 VOLT=(SUM/NAP/2000!)*SNS
2370 REM **** SET SENSITIVITY ****
2375 NTOCKEN=0
2380 IF NS=-1 THEN NS=0
2381 IF NS<0 THEN PRINT BELL$: INPUT "SIGNAL HIGH !! ": STOP
2383 IF NS>=11  THEN NS=11 : GOTO 2450
2388 FOR IL=NS TO NS+2
2390 D=IL-(INT(IL/3)*3)+1
2400 IF D=1 THEN D=5
2410 IF D=3 THEN D=1
2420 SS(IL)=(10^-INT(IL/3))*D*.6
2430 NEXT IL
2432 IF NS=0 THEN SS(NS)=4.8
2440 IF VOLT<=SS(NS+2)*.9 THEN NS=NS+2:NTOCKEN=1: GOTO 2380
2450 IF VOLT>SS(NS) THEN NS=NS-2:NTOCKEN=1: GOTO 2380
2460 IF NTOCKEN=0 THEN RETURN
2470 PRINT#7,"S"+STR$(NS):INPUT#7,A$ : REM SET SENSITIVITY=NS
2480 FOR ID=1 TO 1000: X=2*3!^2 : NEXT ID
2490 GOTO 2250
2500 REM **** SCAN ****
2510 REM LOCK-IN OUTPUT IS CONVERTED TO THE SPECTRAL DATA
2520 REM MOTORS AND LOCK-IN ARE LINKED
2530 IF MTK%=0 THEN GOSUB 800
2540 IF ETK%=0 THEN GOSUB 1700
2550 IF GTK%=0 THEN GOSUB 5000
2560 GOSUB 6400 : LOCATE 20,1
2570 PRINT "    YOU ARE READY TO SCAN IN THE REGION:"
2580 PRINT "    SCAN: FROM ";E1;" TO ";E2;" EV"
2590 PRINT "    WITH: ";NDP;" DATA POINTS"
2600 FOR I=1 TO 500:DUMMY=2*3!^2.3:NEXT I  : REM DELAY
2610 GOSUB 6400 : LOCATE 20,1
2615 PRINT TAB(10) "                **** SCAN MENU ****                    "
2620 PRINT TAB(10) "0----START SCANNING     ; 1----# OF SCANS(DEF 1) ;"
2630 PRINT TAB(10) "2----AVERAGE POINTS(20) ; 3----# OF M-FLAP(DEF 2);"
2640 PRINT TAB(10) "4----ADD SCANS          ; 5----STOP SCANNING     ;"
2650 INPUT QS
2660 PRINT
2670 IF QS<0 OR QS>5 GOTO 2610
2680 IF QS=5 THEN RETURN
2690 IF QS=1 THEN INPUT "   ENTER: # OF SCANS ";NSCAN
2700 IF QS=2 THEN INPUT "    ENTER: # OF AVERAGED POINTS ";NAPDUM
2710 IF QS=3 THEN INPUT "    ENTER: # OF MIRROR FLAPPING ";NMF
```

```
2720 IF QS=4 THEN INPUT "    ENTER: # OF SCANS TO ADD ";NSCAN
2730 IF QS=0 THEN GOTO 2800
2740 GOTO 2610
2800 FOR J2=1 TO NSCAN
2810 FOR I=1 TO NDP :YY(I)=0! :NEXT I
2820 EE=E1: GOSUB 1500:GOSUB 1300:GOSUB 1400:REM GRATING,SOURCE & DETECTOR
2830 GOSUB 6400
2840 J1=J2+J3 : REM J1=# OF TOTLE SCANS SINCE THE PROGRAM STARTS RUNNING
2850 PRINT "    #";J1;" SCAN;                SCANNING ....."
2860 ROL=1 : NOL=0 : REM RATIO OF OVERLAPPING
2870 FOR J=1 TO NDP
2880 DUMY=Y(J)
2900 GOSUB 2240: REM VOLT=OUTPUT
2910 IF MODE$="R" THEN Y(J)=FNYR(J)*ROL:
     DUME=(VOLT-BI(J))*MR(J)/(MI(J)-BI(J))
2920 IF MODE$="M" THEN Y(J)=FNYM(J)*ROL: DUME=SQR(VOLT/SI(J))
2930 IF MODE$="S" THEN Y(J)=FNYS(J)    : DUME=VOLT
2940 IF MODE$="T" THEN Y(J)=FNYT(J)*ROL: DUME=VOLT/SI(J)
2950 SQV(J)=SQV(J)+DUME^2
2960 DRFT(J)=SQR(ABS(SQV(J)-J1*Y(J)^2)) : REM SQUARE ROOT ERROR
2970 YY(J)=Y(J) : GOSUB 6100
2980 EE=X(J+1)
2990 IF J=NDP THEN PRINT#7,"S 0" : INPUT#7,A$ : REM SENS.=5V
3000 IF J=NDP THEN EE=X(1): GOSUB 1400:GOSUB 1500:GOSUB 1300:GOTO 3030
3005 IF EE<ED(DETE%) THEN GOSUB 1400 : REM CHANGE DETECTOR
3010 IF EE<EG(GRAT%) THEN GOSUB 1500 : REM CHANGE GRATING
3020 IF EE<ES(SOUR%) THEN GOSUB 1300 : REM CHANGE SOURCE
3025 IF (DUMG%<>GRAT% OR DUMS%<>SOUR% OR DUMD%<>DETE%) THEN GOSUB 3500
3030 DUMG%=GRAT% : DUMS%=SOUR% :DUMD%=DETE%
3040 REM ****  MOTOR MOVES ****
3050 PMP=INT(FNPMPUV(EE))
3052 IF X(1)<=2! AND EE<=2! THEN PMP=INT(FNPMPIR(EE))
3060 GMP=INT(FNGMP(EE))
3070 PMP$=STR$(PMP) : REM IF A>0 INT(A)= A   IF A<0 INT(A)=-A
3080 GMP$=STR$(GMP) : REM NOTICE THE PRECEDING BLANK ABOVE
3090 IF VAL(PMP$)>=0! THEN PMP$=RIGHT$(PMP$,(LEN(PMP$)-1))
3100 IF FNGMP(EE)>=0! THEN GMP$=RIGHT$(GMP$,(LEN(GMP$)-1))
3110 PMM$="7MPA 7A0.1 7V0.1 7D"+PMP$+" 7G"
3120 GMM$="8MPA 8A0.1 8V0.1 8D"+GMP$+" 8G"
3130 REM IF J=NDP THEN PMM$="7MPA 7A0.1 7V0.2 7D"+PMP$+" 7G"
3140 REM IF J=NDP THEN GMM$="8MPA 8A0.1 8V0.2 8D"+GMP$+" 8G"
3150 GOSUB 4300 : REM MOVE GRATING
3160 GOSUB 4000 : REM MOVE PRISM
3170 REM **** MOTOR STOPS ****
3180 NEXT J
3190 FLDUM$="SPEC"+STR$(-J1): REM SAVE THE SCANS IN SPCE-*
3200 OPEN "O",#5,FLDUM$
3210 PRINT#5," # OF SCANS=";J1
3220 FOR I=1 TO NDP
3230 PRINT#5,USING"+#####.######  ";X(I),Y(I)
```

```
3240 NEXT I
3250 CLOSE(5)
3260 NEXT J2
3270 J3=J1 : REM FOR MULTI-SCAN AVERAGE
3280 GOTO 2610 : REM RETURN TO SCAN MENU
3500 REM **** OVERLAPPING ****
3510 IF J<3 THEN RETURN
3515 IF J=NDP THEN RETURN
3520 NOL=NOL+1
3530 FOR IOL=1 TO 3
3540 XOL(NOL,IOL)=X(J-3+IOL) : EE=X(J-3+IOL)
3550 REM **** PROCEDING MOTOR ****
3560 PMP=INT(FNPMP(EE))
3570 GMP=INT(FNGMP(EE))
3580 PMP$=STR$(PMP) : REM
3590 GMP$=STR$(GMP) : REM
3600 IF FNPMP(EE)>=0! THEN PMP$=RIGHT$(PMP$,(LEN(PMP$)-1))
3610 IF FNGMP(EE)>=0! THEN GMP$=RIGHT$(GMP$,(LEN(GMP$)-1))
3620 PMM$="7MPA 7A0.1 7V0.1 7D"+PMP$+" 7G"
3670 GMM$="8MPA 8A0.1 8V0.1 8D"+GMP$+" 8G"
3700 GOSUB 4300 : REM MOVE GRATING
3710 GOSUB 4000 : REM MOVE PRISM
3720 REM **** END PRECEDING MOTOR ****
3730 GOSUB 2240 : REM VOLT=OUTPUT
3740 IF MODE$="S" THEN YOL(NOL,IOL)=(VOLT+YOL(NOL,IOL)*(J1-1))/J1
3750 IF MODE$="T" THEN
      YOL(NOL,IOL)=(VOLT/SII(NOL,IOL)+YOL(NOL,IOL)*(J1-1))/J1
3760 IF MODE$="M" THEN
      YOL(NOL,IOL)=(SQR(VOLT/SI(J-3+IOL))+YOL(NOL,IOL)*(J1-1))/J1
3765 IF MODE$="R" THEN
      YOL(NOL,IOL)=(VOLT*MR(J-3+IOL)/MII(NOL,IOL)+YOL(NOL,IOL)*(J1-1))/J1
3770 ROL(IOL)=Y(J-3+IOL)/YOL(NOL,IOL)
3780 NEXT IOL
3790 ROL=(ROL(1)+ROL(2)+ROL(3))/3
3800 IF MODE$="S" GOTO 3850
3810 FOR IOL=1 TO 3 : REM NECESSSRY FOR MULTI-SCAN
3820 YOL(NOL,IOL)=YOL(NOL,IOL)*ROL
3830 NEXT IOL
3840 PRINT " OVERLAPPING FACTOR=";ROL
3850 EE=X(J+1)
3860 PRINT:PRINT "    SCANNING ... "
3870 RETURN
4000 REM ****GRATING MOTION ****
4010 REM GRATING WILL MOVE BY "GMM$"
4020 REM EXIT THIS LOOP WHEN MOTOR STOPS
4060 PRINT#8,"8R" : INPUT#8,A$,E$     : REM STATUS REQUEST
4070 IF E$="*R" GOTO 4100             : REM "*R"=READY
4080 IF E$="*B" THEN GOSUB 4200: GOTO 4060 : REM "*B"=BUSY
4090 GOTO 4150
4100 PRINT#8,GMM$ : INPUT#8,A$
```

```
4110 GOSUB 4200
4120 PRINT#8,"8R" : INPUT#8,A$,E$
4130 IF E$="*B" THEN GOSUB 4200 : GOTO 4120
4140 IF E$="*R" THEN RETURN
4150 PRINT "GRATING MOTION ERROR MESSAGE = ";E$
4160 PRINT BELL$
4170 INPUT " DO YOU WANT TO STOP?  Y/N "; Q$
4180 IF Q$="Y" THEN STOP
4190 RETURN
4200 REM **** DELAY LOOP ****
4210 FOR ID=1 TO 50
4220 DUMMY=2*3!^2
4230 NEXT ID
4240 RETURN
4300 REM **** PRISM MOTION ****
4310 REM PRISM WILL MOVE BY "PMM$"
4320 REM EXIT THIS LOOP WHEN MOTOR STOPS
4360 PRINT#8,"7R" : INPUT#8,A$,E$     : REM STATUS REQUEST
4370 IF E$="*R" GOTO 4400             : REM "*R"=READY
4380 IF E$="*B" THEN GOSUB 4200:GOTO 4360 :REM "*B"=BUSY 4200=DELAY
4390 GOTO 4450
4400 PRINT#8,PMM$ : INPUT#8,A$
4410 GOSUB 4200
4420 PRINT#8,"7R" : INPUT#8,A$,E$
4430 IF E$="*B" THEN GOSUB 4200: GOTO 4420
4440 IF E$="*R" THEN RETURN
4450 PRINT "PRISM MOTION ERROR MESSAGE = ";E$
4460 PRINT BELL$
4470 INPUT " DO YOU WANT TO STOP?  Y/N "; Q$
4480 IF Q$="Y" THEN STOP
4490 RETURN
4500 REM ******************************************************
4510 REM **** SUBROUTINE PLOT ****
4520 REM FORTRAN SUBROUTINE , GGRAPH, IS CALLED FOR PLOTTING
4530 GOSUB 6400 : LOCATE 20,1
4540 PRINT TAB(15) "PLOT WHAT?"
4550 PRINT TAB(15) "  S----SPECTRUM"
4560 PRINT TAB(15) "  E----STANDARD RELATIVE ERROR
4570 PRINT TAB(15) "  Q----QUIT PLOTTING
4580 INPUT PLT$
4590 IF PLT$="Q" THEN RETURN
4600 IF PLT$<>"E" AND PLT$<>"S" GOTO 4530
4610 YYMAX=0! : YYMIN=10000!
4620 FOR I=1 TO NDP
4630 IF PLT$="S" THEN YY(I)=Y(I)
4640 IF PLT$="E" AND J1=1 THEN RETURN
4650 IF PLT$="E" THEN YY(I)=100!* DRFT(I)/(Y(I)*SQR(J1*(J1-1)))
4660 IF YY(I)>YYMAX THEN YYMAX=YY(I)
4670 IF YY(I)<YYMIN THEN YYMIN=YY(I)
4680 NEXT I
```

```
4690 GOSUB 5000
4700 PRINT
4710 GOTO 4530
4960 REM ********************* PLOT ROUTINE ***********************
4970 REM THIS PLOT ROUTINE CAN BE USED  WITH ANY                   *
4980 REM BASIC PROGRAM WHICH HAS DATA IN X-YY ARRYS                *
4990 REM ***********************************************************
5000 VIEW (101,21)-(500,270),,1
5010 VIEW PRINT 20 TO 24
5020 REM **** PLOT MENU ****
5030 GOSUB 6400 : LOCATE 20,1
5040 PRINT TAB(12) "P----PLOT          ;" TAB(40) " X----AXES          ;"
5050 PRINT TAB(12) "L----LABEL AXES    ;" TAB(40) " T----TITLE         ;"
5060 PRINT TAB(12) "F----CURVE FONT    ;" TAB(40) " C----CLEAR SCREEN ;"
5070 PRINT TAB(12) "H----HARDCOPY      ;" TAB(40) " R----RETURN        ;"
5080 INPUT Z$
5090 IF Z$="P" THEN GOSUB 6110
5100 IF Z$="X" THEN GOSUB 5200
5110 IF Z$="L" THEN GOSUB 5760
5120 IF Z$="T" THEN GOSUB 5500
5130 IF Z$="F" THEN GOSUB 6080
5140 IF Z$="C" THEN VIEW (101,21)-(500,270):CLS:GOSUB 5210
5150 IF Z$="H" THEN GOSUB 6270
5160 IF Z$="R" THEN RETURN
5170 GOTO 5030
5200 REM **** X-AXIS ****
5202 PRINT:PRINT "       DATA RANGE: X-MIN=";E2;"    X-MAX=";E1
5204       PRINT "                   Y-MIN=";YYMIN;"    Y-MAX=";YYMAX
5206 INPUT "      ENTER: X-MIN AND X-MAX OF AXIS";XMIN,XMAX
5208 INPUT "      ENTER: Y-MIN AND Y-MAX OF AXIS";YMIN, YMAX
5210 FOR IP=1 TO 10
5220 DIVX=IP*40
5230 LINE(DIVX,250)-(DIVX,246)
5235 LINE(DIVX,0)-(DIVX,4)
5240 FOR JP=1 TO 9
5250 SUBX=JP*4
5260 LINE (DIVX-40+SUBX,250)-(DIVX-40+SUBX,248)
5270 NEXT JP
5300 NEXT IP
5310 FOR IP=0 TO 10
5320 DIVX=IP*40+100
5325 VIEW PRINT 18 TO 24
5327 LOCATE 18,CINT(DIVX/8-.8): PRINT "    "
5330 LOCATE 18,CINT(DIVX/8-.8): PRINT (XMAX-XMIN)*IP/10+XMIN
5340 NEXT IP
5350 REM **** Y-AXIS ****
5360 FOR IP=1 TO 10
5370 DIVY=IP*25
5380 LINE(0,DIVY)-(4,DIVY)
5385 LINE(396,DIVY)-(400,DIVY)
```

```
5390 FOR JP=1 TO 4
5400 SUBY=JP*5
5410 LINE(0,DIVY-SUBY)-(2,DIVY-SUBY)
5420 NEXT JP
5430 NEXT IP
5440 VIEW PRINT 1 TO 24
5445 FOR IP=0 TO 10 STEP 2
5450 DIVY=270-IP*25
5455 DUMMY=(YMAX-YMIN)*IP/10+YMIN:DD$=LEFT$(STR$(DUMMY),6)
5457 LOCATE CINT(DIVY*3.05/50+.8),7 : PRINT "      "
5460 LOCATE CINT(DIVY*3.05/50+.8),7 : PRINT DD$
5470 NEXT IP
5480 VIEW (101,21)-(500,270)
5490 VIEW PRINT 20 TO 24
5495 GTK%=1 : RETURN
5500 REM **** TITLE ****
5510 PRINT
5520 INPUT " ENTER: TITLE ";TITLE$
5550 VIEW PRINT 1 TO 2
5560 LOCATE 1,18 : PRINT "                                                  "
5570 LOCATE 1,CINT(38-LEN(TITLE$)/2) : PRINT TITLE$
5580 VIEW (101,21)-(500,270)
5590 VIEW PRINT 20 TO 24
5600 RETURN
5720 REM **** X-AXIS LABEL ****
5750 PRINT
5760 INPUT "ENTER: X-AXIS LABEL ( <20 CHAR ) ";XLABEL$
5765 INPUT "ENTER: Y-AXIS LABEL ( <14 CHAR ) ";YLABEL$
5770 VIEW PRINT 19 TO 24
5780 LENX=LEN(XLABEL$)
5830 LOCATE 19,18 : PRINT "                                                  "
5840 LOCATE 19,CINT(38-LENX/2) : PRINT XLABEL$
5890 REM **** Y-AXIS LABEL ****
5920 LENY=LEN(YLABEL$)
5930 VIEW PRINT 1 TO 24
5960 FOR IPP=1 TO 14:LOCATE 2+IPP,4 : PRINT " " :NEXT IPP
5970 FOR IP=1 TO LENY
5980 Y$=MID$(YLABEL$,IP,1)
6000 LOCATE CINT(9-LENY/2+IP),4 : PRINT Y$
6010 NEXT IP
6020 VIEW (101,21)-(500,270) : VIEW PRINT 20 TO 24
6030 RETURN
6060 REM **** LINE OR DOTS ****
6070 PRINT
6080 PRINT "ENTER: 0----DOTS      ; 1----LINE "
6090 INPUT LP: RETURN
6099 REM **** PLOT ****
6100 IF J=1 THEN VIEW (101,21)-(500,270) :CLS:GOSUB 5210
6110 IF GTK%=0 THEN GOSUB 5200
6120 VIEW (101,21)-(500,270)
```

```
6130 WINDOW(XMIN,YMIN)-(XMAX,YMAX)
6140 IF LP=0 GOTO 6200
6150 FOR IP=1 TO NDP-1
6160 LINE(X(IP),YY(IP))-(X(IP+1),YY(IP+1))
6170 NEXT IP
6180 WINDOW
6190 RETURN
6200 FOR IP=1 TO NDP
6210 PSET(X(IP),YY(IP))
6220 NEXT IP
6230 WINDOW
6240 RETURN
6260 REM **** HARDCOPY ****
6270 INPUT " TYPE <SHIFT>+<CNTL>+<PRINT> FOLLOWING 'RETURN' ";Z$
6280 GOSUB 6400
6290 INPUT " ",A$
6300 RETURN
6400 REM **** CLEAR TEXT AREA ****
6410 VIEW
6420 VIEW (1,305)-(609,398)
6430 CLS
6440 VIEW (101,21)-(500,270)
6450 RETURN
7490 REM **** FILE DATA ****
7500 REM ************************************************
7510 REM DATA ARE TRANSFERED FROM ARRAYS X(I),Y(I) INTO DFN$*
7520 REM THE FIRST LINE IN THE FILE IS THE FILE DISCRIPTION *
7530 REM DATA ARE STORED IN TWO COLUMN, X(I) AND Y(I), AND  *
7540 REM IN DOUBLE PRECISION (+#####.###### )FORMAT        *
7550 REM ************************************************
7560 GOSUB 6400 : LOCATE 20,1
7570 INPUT "ENTER DATA FILE NAME ";DFN$
7580 INPUT "ENTER SAMPLE NAME    ";SMP$
7590 INPUT "ENTER REFLECTANCE OR TRANSMITTANCE ";RT$
7600 INPUT "ENTER DATE OF MEASUREMENT ";DT$
7610 OPEN "O",#2,DFN$
7620 PRINT#2,"SAMPLE: "+SMP$+"   "+RT$+"    MEASRUED ON "+DT$
7630 IF MODE$="S" THEN PRINT#2,NDP,NOL
7640 FOR I=1 TO NDP
7650 PRINT#2,USING"+#####.######  ";X(I),Y(I)
7660 NEXT I
7670 IF MODE$<>"S" THEN CLOSE(2) : RETURN
7680 FOR I=1 TO NOL
7690 FOR II=1 TO 3
7700 PRINT#2,USING"+#####.######  ";XOL(I,II),YOL(I,II)
7710 NEXT II
7720 NEXT I
7730 CLOSE(2) : RETURN
8000 REM ********* MOTORS GO HOME *************
8010 GOSUB 6400 : LOCATE 20,1
```

```
8020 PMM$="7MPA 7A0.2 7V0.1 7D0 7G "
8030 GMM$="8MPA 8A0.2 8V0.1 8D0 8G "
8040 GOSUB 4000
8050 GOSUB 4300
8060 PRINT " PRISM POSITION SHOULD BE 2000"
8070 PRINT " GRATING POSITION SHOULD BE 2000"
8080 INPUT " THEN PRESS 'RETURN' ";Q$
8090 RETURN
8100 REM **** END ****
8110 GOSUB 8000
8120 CLOSE(7)
8130 CLOSE(8)
8140 SCREEN 0,0
8150 END
8500 REM **** END ****
8510 GOSUB 8000
8520 CLOSE(7)
8530 CLOSE(8)
8540 SCREEN 0,0
8550 END
```

The vita has been removed from the scanned document